Modeling tissue-specific *Drosophila* metabolism identifies high sugar diet-induced metabolic dysregulation in muscle at reaction and pathway levels

Authors

Sun Jin Moon[1*], Yanhui Hu[1], Monika Dzieciatkowska[2], Ah-Ram Kim[1], John M. Asara[3,4], Angelo D'Alessandro[2], Norbert Perrimon[1,5*]

Affiliations

[1]Department of Genetics, Blavatnik Institute, Harvard Medical School, Boston, MA 02115

[2]Department of Biochemistry and Molecular Genetics, University of Colorado Anschutz, Aurora, CO 80045

[3]Division of Signal Transduction, Beth Israel Deaconess Medical Center, Boston, MA 02115

[4]Department of Medicine, Harvard Medical School, Boston, MA 02115

[5]Howard Hughes Medical Institute, Harvard Medical School, Boston, MA 02115

[*]Correspondence: Sun Jin Moon and Norbert Perrimon

Emails: sunjin_moon@hms.harvard.edu and perrimon@genetics.med.harvard.edu

Abstract

Individual tissues perform highly specialized metabolic functions to maintain whole-body metabolic homeostasis. Although *Drosophila* serves as a powerful model for studying human metabolic diseases, modeling tissue-specific metabolism has been limited in this organism. To address this gap, we reconstruct 32 tissue-specific genome-scale metabolic models (GEMs) by integrating a curated *Drosophila* metabolic network with pseudo-bulk single-nuclei transcriptomics data, revealing distinct metabolic network structures and subsystem coverage across tissues. We validate enriched pathways identified through tissue-specific GEMs, particularly in muscle and fat body, using metabolomics and pathway analysis. Moreover, to demonstrate the utility in disease modeling, we apply muscle-GEM to investigate high sugar diet (HSD)-induced metabolic dysregulation. Constraint-based semi-quantitative flux and sensitivity analyses identify altered NAD(H)-dependent reactions and distributed control of glycolytic flux, including GAPDH. This prediction is further validated through *in vivo* ^{13}C-glucose isotope tracing study. Notably, decreased glycolytic flux, including GAPDH, is linked to increased redox modifications. Finally, our pathway-level flux analyses identify dysregulation in fructose metabolism. Together, this work establishes a quantitative framework for tissue-specific metabolic modeling in *Drosophila*, demonstrating its utility for identifying dysregulated reactions and pathways in muscle in response to HSD.

Introduction

Multicellular organisms consist of tissues that perform highly specialized metabolic functions[1]. As such, analyzing tissue-level metabolism is critical to delineate the complex metabolic interplay among tissues and understand organismal physiology[2]. However, direct measurements of tissue-specific enzyme levels or fluxes are often unavailable. Instead, mRNA levels have served as a proxy to reconstruct context-relevant or tissue-specific genome-scale metabolic models (GEMs)[3–5], enabling quantitative metabolic network analyses. In fact, numerous computational algorithms such as mCADRE[6], tINIT[7,8], CORDA[5], and MERGE[4], have been developed and applied for reconstruction of tissue-specific GEMs across complex organisms from *C. elegans*[4] to *Homo sapiens*[6]. Yet, tissue-specific metabolic models in *Drosophila melanogaster* are unavailable, limiting quantitative assessments of metabolic processes at tissue level in this organism[9,10].

The high conservation of metabolic genes and functionally analogous organs between humans and fruit flies, together with the short generation time, lifespan, and availability of numerous genetic and analytical tools for *Drosophila*, has made flies an excellent organism in which to model human metabolic diseases[11,12]. Various mechanisms underlying dysregulated metabolism associated with type 2 diabetes[13,14], aging[15], and cancer[16] have been elucidated in flies. Moreover, several generic GEMs, such as *FlySilico*[17], *iDrosophila*[18], and *Fruitfly1*[19], have recently been developed, enabling systems-level evaluations of metabolic networks in this organism. However, they lack the resolution needed for tissue-specific metabolic analysis.

While GEMs are powerful computational tools for analyzing metabolic network structures and simulating fluxes, experimental techniques such as metabolomics, ^{13}C isotope tracing, and redox proteomics also serve as valuable complementary and validation approaches for quantitative metabolic analyses. Metabolomics provides a comprehensive snapshot of metabolite profiles[20,21], while ^{13}C isotope tracing techniques can estimate specific metabolic pathway activity[22,23]. Furthermore, redox proteomics reveals the extent of redox modifications on sensitive amino acid residues (e.g., cysteine and methionine), providing insight into the post-translational regulation of enzyme activity[24–27]. However, such experimental analyses are often underrepresented in GEM-focused metabolic studies, limiting both quantitative metabolic investigation and empirical validation when studying complex metabolic diseases. As such, leveraging both computational modeling and experimental approaches is essential for advancing quantitative understanding of complex metabolic disorders like type 2 diabetes (T2D).

T2D is characterized by insulin resistance and hyperglycemia, posing a significant global health challenge[28–30]. *Drosophila* effectively models key metabolic features of human T2D through high-sugar

67 diet (HSD) feeding, which impairs glucose homeostasis, and induces mitochondrial dysfunction and
68 tissue-specific metabolic dysregulation[13,14,31,32]. Among affected tissues, muscle plays a central role in
69 glucose metabolism and insulin sensitivity. While perturbations in glycolytic and TCA cycle activities
70 have been observed in diabetic muscle[29,33,34], many questions remain unanswered. Specifically, the extent
71 to which NAD(H)-dependent reactions are altered, the identity of potential rate-controlling steps within
72 glycolysis, and the additionally dysregulated metabolic pathways beyond central carbon metabolism
73 remain to be elucidated.

74 In this study, we first reconstructed 32 tissue-specific GEMs for adult *Drosophila* by integrating a
75 curated *Drosophila* metabolic network model with pseudo-bulk single-nuclei transcriptomics data. These
76 GEMs enabled us to systematically evaluate similarities and differences in metabolic network structures
77 across individual tissues. After validating GEM-based predictions on enriched pathways using targeted
78 metabolomics and pathway enrichment analyses, we demonstrated the utility of tissue-specific GEMs in
79 modeling human metabolic disease. Specifically, we applied the muscle-GEM to simulate metabolic
80 changes induced by a high-sugar diet (HSD), a well-established *Drosophila* model of T2D. Constraint-
81 based flux analyses revealed altered fluxes in NAD(H)-dependent fluxes, including a decreased maximal
82 NADH production capacity, and sensitivity analysis indicated distributed control of glycolytic fluxes
83 across several enzymes, including GAPDH. [U-^{13}C]-glucose tracing and redox proteomics further
84 confirmed decreased glycolytic flux and revealed that these changes were associated with increased redox
85 modifications of glycolytic enzymes. Pathway-level flux comparisons further highlighted dysregulated
86 fructose metabolism. Together, this work establishes a quantitative framework for tissue-specific
87 metabolic modeling in *Drosophila* and demonstrates its utility for identifying high sugar diet-induced
88 metabolic perturbations at reaction and pathway levels.

Results

Reconstruction of 32 tissue-specific genome-scale metabolic models (GEMs) in *Drosophila melanogaster*

To evaluate tissue-specific metabolism in *Drosophila*, we designed a strategy to reconstruct 32 tissue-specific genome-scale metabolic models (GEMs) and analyze their metabolic network structures and functions (**Fig. 1a,** Error! Reference source not found.**a-e**). The reconstructed tissue-specific GEMs revealed variations in their metabolic network structures, reflected in the differing numbers of reactions, metabolites, and genes across tissues (Error! Reference source not found.**a**). Among 32 tissue-specific GEMs, fat body and oenocytes, analogous to human adipose tissue and liver, contained the highest number of reactions (n = 5,447 and 5,015), while most neuronal tissues had the fewest number of reactions (n = 2,533 to 3,077). A similar trend was observed for the metabolite numbers across tissue-specific GEMs. Additionally, we observed a positive correlation between the number of reactions and metabolites ($R^2 = 0.92$), consistent with the expected increase of metabolite numbers as reactions number increases. The number of genes also varied across models, ranging from 565 to 858, with the germline and fat body containing the higher numbers. Similarly, we observed a positive correlation between the number of reactions and genes ($R^2 = 0.54$) (Error! Reference source not found.**b**).

Based on these differences, we hypothesized that the tissues performing similar metabolic functions would show similar metabolic network structures. To test this hypothesis, we compared the metabolic network structures of 32 tissue-specific GEMs by specifically comparing their reaction contents (**Fig. 1b)**. Hierarchical clustering analysis revealed 13 distinct clusters of similar metabolic network structures (Error! Reference source not found.**c** and Error! Reference source not found.**f**). As expected, tissues of similar functions were grouped together - muscle and indirect muscle; fat body and oenocytes; hindgut and enteroendocrine cells; seven neuron GEMs, and six glia cells distributed across three different clusters. Additionally, to assess how these GEM-based clusters compared to transcriptomics-based clustering, we performed hierarchical clustering of gene expression data and calculated Jaccard indices to quantify overlap (Error! Reference source not found.**d-e**). While we observed high overlap between the two approaches for muscle and neuron clusters (Jaccard index = 1) and fat body/oenocytes (0.75), clustering of glia and gut tissues showed lower overlap between the two approaches (**Fig 1c** and Error! Reference source not found.**g**). These results indicate that clustering based on metabolic network structures, which incorporate stoichiometric constraints of biochemical reactions, reveals metabolic distinctions not apparent from transcriptomics alone.

Next, to further evaluate differences in metabolic network structures across tissue-specific GEMs, we analyzed their metabolic subsystem coverage. We found that transport reaction subsystem accounted for the largest proportion of all subsystems, comprising approximately 35 ± 4 % of all reactions (**Fig 1d**). Within this subsystem, extracellular transporter reactions accounted for approximately 80 ± 6 %. Interestingly, while muscle group did not have the most transport reactions compared to other tissue groups, it had the highest fraction of the extracellular transport reactions (f = 0.86 ± 0.02) (**Fig 1e** and Error! Reference source not found.**h**). Additionally, we calculated the percent difference in subsystem coverage and identified 33 subsystems with more than 50% deviation from mean coverage across tissues (**Fig 1f**, Error! Reference source not found.**i-j)**. Notably, fat body and oenocyte GEMs had the highest reaction counts, particularly in beta-oxidation subsystems ($n_{reactions}$ = 36.6 ± 15, $p < 0.0001$) (Error! Reference source not found.**f**), supporting their known function in beta-oxidation of fatty acids[11,35].

Moreover, we performed a metabolic task analysis to determine the extent to which tissue-specific GEMs could perform 219 pre-defined metabolic tasks (Error! Reference source not found.**k**)[7,36]. Tissue-specific GEMs could pass an average of 40 ± 10 tasks, with germline cells completing the most metabolic tasks (n_{pass} = 66) and polar follicle cells the least (n_{pass} = 17) (Error! Reference source not found.**g-h**). Additionally, consistent with the known role of fat body in performing gluconeogenesis and trehalose synthesis[37], we confirmed that fat body-GEM could synthesize trehalose from various substrates, including alanine, pyruvate, glutamine, and glycerol (Error! Reference source not found.**l**). Furthermore, after categorizing metabolic tasks into seven metabolic systems, we performed Fisher's exact test and found significant tissue-specific associations with the specific metabolic systems: fat body with carbohydrate/amino acid metabolism, and CNS glia/gustatory neurons with lipid metabolism (Error! Reference source not found.**l** and Error! Reference source not found.**m-n**). Taken together, our reconstructed tissue-specific GEMs provide a systems-level framework to evaluate metabolic differences and similarities across tissues in *Drosophila*, enabling quantitative comparisons of tissue-specific metabolic network structures and metabolic capabilities.

Validation of tissue-specific GEMs through regional metabolomics and pathway analysis

Validating the predictions from tissue-specific GEMs is essential to establish confidence in GEM-based analyses. Although gene essentiality analysis is commonly used for validation[38,39], *in vivo* growth rate data were unavailable for the tissues we investigated. Thus, we performed targeted metabolomics and pathway enrichment analysis, while comparing these results to GEM-based pathway analysis. We

152 hypothesized that enriched pathways identified through metabolomics would also be represented in the
153 corresponding tissue-specific GEMs. To test the hypothesis, we first profiled 303 polar metabolites in
154 four dissected *Drosophila* regions - head (containing neuronal and glial cells), thorax (containing muscle
155 cells), gut (containing hindgut/enteroendocrine cells), and abdomen (containing fat body, oenocytes, and
156 other tissues) (**Fig. 2a** and Error! Reference source not found.**a**).

157 Principal component analysis and hierarchical clustering revealed distinct metabolite profiles
158 among these regions **(Fig. 2b-c)**. Specifically, we identified 10 significantly enriched metabolites in
159 thorax, 13 in head, 20 in gut, and 1 in abdomen ($Log_2FC > 2$ and p-value < 0.05) (**Fig. 2d,** Error!
160 Reference source not found.**b**). Qualitatively, these enriched metabolites aligned with known tissue
161 functions. For instance, in thorax, energy-related metabolites such as adenosine, adenylosuccinate,
162 adenine, and AMP were enriched, consistent with muscle's high demand on energy metabolism compared
163 to other tissues[11] (Error! Reference source not found.**a**). In heads, 4-aminobutyrate (GABA), N-acetyl-L-
164 aspartate, GMP, and ascorbates, were enriched. GABA is a major inhibitory neurotransmitter, and N-
165 acetyl-L-aspartate is often used as a marker for neuronal health[40,41]. In gut, including Malpighian tubules
166 (MT), dietary-related metabolites, such as pyridoxine, betaine, and uric acids, were enriched, consistent
167 with their dietary origin and uric acids generated from MT's purine excretion[42–45]. In abdominal carcass,
168 containing fat body and oenocytes, nucleotide and one-carbon metabolites were enriched, such as
169 xanthosine and hypoxanthine, methionine s-adenosyl-l-methioninamine and 5-methyl-THF.

170 Next, we performed KEGG pathway enrichment analysis using the hypergeometric test based on
171 the enriched metabolite sets[46] (**Fig. 2e** and Error! Reference source not found.**c**). The most significantly
172 enriched pathway was purine metabolism (KEGG ID: dme00230) for thorax, pyrimidine metabolism
173 (dme00240) for gut, and one carbon pool by folate (dme00670) for head and abdomen (Error! Reference
174 source not found.**b**). We also identified six pathways commonly enriched across all regions, such as TCA
175 cycle, glyoxylate, purine, and pyrimidine metabolism (Error! Reference source not found.**c**). Moreover,
176 several region-specific enriched pathways were identified, such as starch/sucrose metabolism, histidine
177 metabolism, and fatty acid degradation in thorax.

178 Next, we compared these metabolomics-derived enriched pathways to those predicted from
179 subsystem coverage analysis of tissue-specific GEMs, using weighted Jaccard index[47,48] (**Fig. 2f** and
180 Error! Reference source not found.). In brief, the index quantifies the degree of pathway overlap between
181 the two datasets. We expected higher index values for tissues associated with specific regions (e.g.,
182 muscle with thorax[49] and fat body/oenocytes with abdomen[50]). Indeed, muscle-GEM showed the highest
183 index value with thorax (index: 0.8 ± 0.1), compared to those for other regions (head: 0.48 ± 0.2,
184 abdomen: 0.44 ± 0.1, gut: 0) (**Fig. 2g** and Error! Reference source not found.**d-f)**. The overlapped

pathways included butanoate, glycolysis, lipoic, and starch metabolism. Additionally, fat body-GEM also showed high index value with abdomen, with overlapped pathways including cysteine, nicotinamide, and pantothenate metabolism (**Fig. 2h)**. However, pathway overlaps were less distinct for neuron/glia cells and gut groups, as no uniquely enriched pathways were identified for these regions in our datasets (Error! Reference source not found.**d**). Furthermore, when we repeated this analysis using gene expression data, we observed significantly lower Jaccard index values across all tissues, with no distinct trends (Error! Reference source not found.**e** and Error! Reference source not found.**g-h**). This indicated that GEM-predicted enriched pathways more accurately reflect metabolomics-derived pathways, compared to gene expression-derived enriched pathways. Taken together, these results validate GEM-predicted pathway analysis, particularly for muscle and fat body.

Constraint-based flux analyses predict perturbations in NAD(H)-dependent reactions in muscle under high sugar diet

Among the reconstructed tissue-specific GEMs, we further applied the muscle-GEM to evaluate how muscle metabolism could be rewired in response to high sugar diet (HSD), which induces type 2 diabetes-like phenotypes in *Drosophila*[14,31,51]. We first defined a HSD-muscle-GEM by constraining reaction rates to simulate metabolic phenotypes observed in type 2 diabetic muscle based on the literature evidence[28,29,33,34,52–54] (**Fig. 3a** and Error! Reference source not found.**a-b**). These constraints included glucose uptake rates, GAPDH, and several reactions in TCA cycle[53,55]. Consistent with our applied constraints, flux variability analysis with sampling (FVA-sampling) showed a reduction in glucose uptake rate, along with decreased fluxes through GAPDH, OGDH, and SDH (Error! Reference source not found.**a-b**, Error! Reference source not found., and Error! Reference source not found.**c-d**). The decrease in model-generated glucose uptake rate was confirmed experimentally by measuring glucose uptake rates in w^{1118} male flies fed with HSD (Error! Reference source not found.**c**).

Next, to identify perturbed reactions beyond those we directly constrained, we systematically compared differential fluxes obtained from flux balance analysis (FBA), FVA-sampling, and parsimonious FBA (pFBA) (Error! Reference source not found.). In brief, we performed pFBA to complement FVA-sampling analysis, which could generate non-physiologically high fluxes in reactions such as NAD(H)-dependent cycling reactions and generate fluxes near boundaries due to under-constrained nature of network (Error! Reference source not found.**d-g,** Error! Reference source not found.**e-f**). By comparing these analyses, we identified 77 reactions showing consistently decreased fluxes and 18 with increased fluxes in the HSD-muscle-GEM relative to the unconstrained model (Error!

217 Reference source not found.**h** and Error! Reference source not found.**g**). Among the reactions with
218 decreased fluxes, many were associated with transport, aminoacyl-tRNA biosynthesis, and glycolysis,
219 with associated genes including *Dic1*, *Cd98hc*, *Gapdh1/2*, *Aldo*, *Eno*, *Pfk*, and aminoacyl-tRNA
220 synthetases such as *AsnRS* and *AspRS* (**Fig. 3b**). In contrast, reactions with increased fluxes were mainly
221 linked to transport, aromatic amino acid biosynthesis, and TCA/glyoxylate metabolism, with associated
222 genes including *Hrm*, *Cg6231*, *Got1/2*, *Kdn*, *Scsa1*, and *Mdh2*.

223 As perturbed NADH metabolism has also been implicated in type 2 diabetes[56,57], we further
224 investigated individual NAD(H) dependent reactions to identify specific reactions showing altered fluxes.
225 By comparing differential fluxes of 135 active NAD(H) dependent reactions across three different flux
226 simulations, we identified 23 reactions showing consistently decreased fluxes and 3 reactions with
227 increased flux (Error! Reference source not found.**i-j and** Error! Reference source not found.**h-j**).
228 Associated genes with decreased fluxes included *Dhfr, Ldh, Gs,* and *Gapdh1/2*, while those with
229 increased fluxes included *Mdh2* and *CG5955*. Profiling differential fluxes of NAD(H)-dependent
230 reactions further highlighted a variety of significantly perturbed reactions and their magnitudes **(Fig. 3c).**
231 Next, to further investigate whether the network's maximum capacity of NADH production was
232 perturbed, we introduced an artificial NADH demand reaction and maximized its flux (**Fig. 3d**). This
233 analysis revealed approximately a 27% reduction in NADH maximum production capacity in the HSD-
234 muscle GEM, accompanied by altered contributions of individual NADH-producing reactions (**Fig. 3e**
235 and Error! Reference source not found.**k**). Although this change does not directly predict the cellular
236 NAD^+/NADH ratio, it suggests impaired NADH turnover, consistent with our experimental observation
237 of a decreased NAD^+/NADH ratio in thoracic muscle of w^{1118} flies fed with HSD (**Fig. 3f**). Together, our
238 constraint-based semi-quantitative flux analyses predicted perturbations in specific subsystems, reactions,
239 and genes in muscle under HSD, highlighting disrupted NAD(H)-dependent reactions characterized by
240 altered flux distributions and decreased NADH production capacity.

241

242 Sensitivity analysis reveals distributed control of glycolytic flux

243 Given that NAD(H)-dependent reaction fluxes were perturbed in the HSD-muscle GEM and
244 GAPDH functions as one of the key NAD^+-dependent glycolytic enzymes, we examined whether
245 GAPDH could serve as a rate controlling step in glycolysis under HSD condition. To test this, we
246 performed a sensitivity analysis (See **Methods**). In brief, we systematically decreased the baseline flux of
247 each glycolytic reaction, defined as the median flux from FVA-sampling, and quantified the total
248 pyruvate consumption flux as a proxy for glycolytic output flux (**Fig. 3g** and Error! Reference source not

found.**l**). At relatively larger perturbation (e.g., 20 to 50 %), most of the lower glycolytic enzymes showed positive sensitivity coefficients, suggesting that decreases in these fluxes led to reductions in total pyruvate consumption **(Fig. 3h** and Error! Reference source not found.**k)**. In contrast, at smaller perturbations (e.g., 5 and 10 %), several enzymes, including Hex-a/b, Pgk and Gapdh1/2, showed strong negative sensitivity coefficients, suggesting that decreases in these fluxes may trigger compensatory increases in total pyruvate consumption through alternative reactions. Indeed, evaluation of individual pyruvate consuming reactions revealed diverse responses to perturbations. Specifically, while alanine transaminase (*CG1640*) consistently showed decreased flux in response to high perturbation (e.g., 50 %), monocarboxylate transporter (*MCT1*), or other reactions showed increased fluxes in response to varying perturbations, reflecting the nonlinear and compensatory nature of metabolic network (Error! Reference source not found.**m)**. When comparing absolute magnitudes of sensitivity coefficients across all perturbations, we found Aldo exhibited the highest average sensitivity coefficient (0.13), with Pgk (0.12), Gapdh1/2 (0.12), and Hex-a/b (0.11) showing comparable sensitivity (**Fig. 3h**). Altogether, these results suggest that glycolytic flux is not solely controlled by GAPDH as initially hypothesized, but is distributed among several other enzymes and varies with perturbation magnitude under this condition.

Model-predicted decreases in glycolytic flux, including GAPDH, validated through ^{13}C-glucose tracing

To validate the predicted fluxes in glycolysis, particularly involving GAPDH, we performed *in vivo* ^{13}C-glucose isotopic tracing experiments. After feeding w^{1118} male flies with a HSD containing uniformly labeled ^{13}C-glucose tracer for five days, we dissected the thoracic muscle and evaluated both the metabolite intensities and labeling patterns of downstream metabolites using mass spectrometry (**Fig. 4a**). As the [U-^{13}C]glucose is metabolized in cells, glycolytic intermediates will have M+6 or M+3 mass isotopomers, and TCA cycle metabolites will show M+2 mass isotopomers after the first cycle (**Fig. 4b)**. Based on our sensitivity analysis, where we observed strong control around Aldo, Pgk, and Gapdh, we hypothesized that a bottleneck step would result in decreased fractional labeling of downstream isotopomers, accompanied by accumulation of upstream substrates and decreased levels of downstream products.

Indeed, we observed that upper glycolytic intermediates increased by approximately 23 %, including F6P, F16BP, and glyceraldehyde 3-phosphate, a substrate of GAPDH (Error! Reference source not found.**a-b** and Error! Reference source not found.**a-b**). Conversely, lower glycolytic intermediates,

280 such as 3PG and lactate, decreased by 27% and 14%, respectively. Moreover, the fractional labeling of
281 lower glycolytic intermediates was significantly decreased compared to that of upper glycolytic
282 intermediates (**Fig. 4c)**. Specifically, the M+3 fractional labeling of 1,3-BPG, the product GAPDH, was
283 nearly 90 % lower in response to HSD, indicating a significantly reduced GAPDH activity. In TCA cycle,
284 the abundances of citrate, succinate, fumarate, malate, and glutamate, increased by 40%, 34%, 14%, 97%,
285 and 24%, respectively (Error! Reference source not found.**c-d** and Error! Reference source not found.**c**).
286 Moreover, their M+2 fractional labeling decreased relative to M+6 glucose, suggesting a decreased
287 contribution of glucose-derived carbon to the TCA cycle (**Fig. 4d**).

288 Furthermore, to investigate the extent to which our model-predicted fluxes align with
289 experimental measurements, we performed a correlation analysis by mapping the flux of each reaction in
290 the HSD-muscle-GEM to the fractional labeling of its corresponding metabolite product. Notably, we
291 observed a strong correlation between the fractional labeling data and model-predicted relative fluxes
292 within glycolysis ($\rho = 0.81$, $p = 0.03$), supporting the accuracy of model predictions for this pathway (**Fig.**
293 **4e)**. In contrast, correlation in the TCA cycle was weaker ($\rho = 0.12$), potentially due to the contributions
294 from other carbon sources (e.g., fatty acids[58]) accounting the predicted fluxes in the TCA cycle (Error!
295 Reference source not found.**e**). Taken together, these results confirm the model-predicted flux changes,
296 specifically for glycolysis, and reveal GAPDH as one of the key regulatory steps in muscle in response to
297 HSD.

298

299 Model-predicted decreases in glycolytic flux correlate with increased
300 redox modification of glycolytic enzymes

301 Since redox modification, including oxidation of cysteine residue, can directly alter enzyme
302 activity such as GAPDH[24,26,59,60], we were wondering whether the decreased glycolytic fluxes, particularly
303 GAPDH, were linked to redox modifications (**Fig. 5a**). Given the increased oxidative stress observed in
304 diabetic muscle[53,61,62], we hypothesized that redox modification at cysteine or methionine residues would
305 also be elevated in HSD-fed fly muscle. Indeed, PCA of redox proteomics revealed greater variability in
306 peptide oxidation profiles in HSD samples compared to NSD controls (**Fig. 5b**). Among 1049 detected
307 peptides, 189 peptides exhibited significantly increased redox modifications ($Log_2|FC| > 0.5$ and adjusted
308 p-value < 0.05) (**Fig. 5c,** Error! Reference source not found.**a** and Error! Reference source not found.**a**).
309 Next, based on these significantly oxidized peptides, we performed KEGG over-representation analysis[63]
310 to identify pathways enriched for redox-modified enzymes (Error! Reference source not found.**b**).

311 Consistent to prior studies, the most affected pathways were oxidative phosphorylation (dme00190), a
312 well-known site of mitochondrial dysfunction observed in diabetic muscle[64,65]. Within this pathway, we
313 observed increased redox modifications in peptides, including succinate dehydrogenase, NADH
314 dehydrogenase, V-ATPase, citrate synthase, and isocitrate dehydrogenase (Error! Reference source not
315 found.**b**). Interestingly, glycolysis was also significantly affected, with increased redox modifications
316 observed in peptides, including Ald1, Gapdh1/2, Pyk, Pgi, Pfk, Pgm1, Eno, Fdh, and Pgk (**Fig. 5e**).

317 To further evaluate the relationship between the extent of redox modification and predicted fluxes
318 in glycolysis, we performed a correlation analysis and found a significant negative correlation ($r = -0.78$,
319 $p = 0.025$) (**Fig. 5f**). Specifically, Pyk exhibited the highest level of redox modification and corresponded
320 to the largest flux decrease, whereas Pgm1 showed minimal redox modification and the smallest flux
321 change (Error! Reference source not found.**c-d**). Notably, protein levels of most glycolytic enzymes
322 remained unchanged, except for Pyk, suggesting that redox modifications, rather than enzyme abundance,
323 more strongly associate with changes in glycolytic flux (Error! Reference source not found.**e-f**).

324 Moreover, since our flux analyses and isotope tracing results revealed GAPDH as one of the key
325 perturbed steps in glycolysis, we further evaluated this enzyme. In *Drosophila*, two isoforms of GAPDH
326 are present, both closely related to human GAPDH and known to perform partially redundant functions in
327 glycolysis (Error! Reference source not found.**g**)[66]. While the enzyme levels of both GAPDH1 and
328 GAPDH2 remained unchanged (Error! Reference source not found.**h**), we observed significant redox
329 modifications at Met-40 residue in GAPDH1 and at Cys-130, Met-127, 141 and 172 in GAPDH2
330 (referenced to Uniprot:P07486 for GAPDH1 and M9PJN8 for GAPDH2) (**Fig. 5g** and Error! Reference
331 source not found.**i-j**). Structural modeling using AlphaFold further predicted that Met-40 is in near to the
332 NAD^+ binding site (~9 Å), suggesting that redox modification at this residue could indirectly affect NAD^+
333 binding and impair activity (Error! Reference source not found.**k**). Additionally, to further investigate the
334 functional role of GAPDH in muscle, we used a muscle-specific Mhc-Gal4 driver combined with a
335 temperature-sensitive Gal80ts system to knock down GAPDH1 in fly muscle. Indeed, muscle-specific
336 downregulation of GADPH1 led to a significant decline in climbing ability in male flies fed with HSD
337 starting at day 10, suggesting a physiologically important role for GAPDH1 in maintaining muscle
338 function (**Fig. 5h** and Error! Reference source not found.**l**). In summary, these results indicate a strong
339 association between increased redox modifications and decreased glycolytic fluxes, identifying the redox
340 modification of GAPDH and its knockdown causing climbing defects.

341

Pathway-level flux analysis reveals dysregulated fructose metabolism

Next, to identify pathway-level perturbations beyond glycolysis under HSD conditions, we evaluated differential pathway fluxes obtained from FVA sampling and pFBA analyses (**Fig. 6a** and **Methods**). In brief, we defined pathway flux as the average of non-zero flux magnitudes within each pathway. Using this approach, we identified 77 significantly perturbed pathways, with 33 pathways overlapping between flux sampling and pFBA analyses (**Fig. 6b** and Error! Reference source not found.**a**). Consistent with our prior findings, we observed significant decrease in pathway fluxes through glycolysis, oxidative phosphorylation, and the TCA cycle, with fructose showing the most pronounced decrease in the HSD muscle compared to control. Among the top perturbed pathways with increased pathway fluxes, we found fatty acid metabolism (e.g., β-oxidation, desaturation, elongation, and omega-3/6 metabolism), lipid droplet turnover (pool reactions), butanoate metabolism, glycerophospholipid, and several amino acid metabolism pathways (e.g., tryptophan, phenylalanine-tyrosine).

To validate the predicted pathway-level perturbations, we performed targeted metabolomics in thoracic muscles in response to HSD (**Fig. 6c)**. PCA revealed distinct metabolite profiles between HSD and NSD conditions (**Fig. 6d**). Among the six most significantly altered metabolites, three were involved in either fructose/sucrose metabolism (e.g., sorbitol and trehalose/sucrose) or butanoate metabolism (e.g., acetoacetyl-CoA) ($Log_2|FC| > 2$ and p-value < 0.01), consistent with the pathways identified as highly perturbed (**Fig. 6e** and Error! Reference source not found.**b**). To further investigate how these metabolite changes relate to fluxes and enzyme redox modifications, we created an integrated metabolic map focusing on fructose/sucrose metabolism (**Fig. 6f)**. Beyond the perturbations in upper glycolysis, we found that Trehalase, an enzyme that converts trehalose to glucose, showed a decreased predicted flux ($Log_2FC = -5.4$) and significant oxidation at a methionine residue ($Log_2FC = 1.75$, $p = 0.006$). Collectively, these results demonstrate that our pathway-level flux analysis, supported by metabolomics and redox proteomics, effectively identifies candidate dysregulated metabolic pathways, such as fructose metabolism in muscle under HSD condition.

Discussion

Modeling tissue-specific metabolism is essential to dissect the complex interplay of metabolic activities in multicellular organisms. In this study, we reconstructed 32 tissue-specific GEMs by integrating pseudo-bulk single-nuclei transcriptomics datasets with the manually curated generic *Drosophila* metabolic model. These tissue-specific GEMs enable quantitative comparisons of their

373 metabolic network structures, representing a significant advance over existing *Drosophila* generic GEMs,
374 such as Fruitfly1[19], FlySilico[17], and iDrosophila[18], which lack tissue-level metabolic analyses.

375 Furthermore, our tissue-specific GEMs offer distinct advantages by enabling network-level flux
376 analyses that are difficult to achieve with pathway-specific or resource-intensive isotope tracing
377 experiments. Specifically, using the muscle-GEM, we predicted active NAD(H)-dependent flux changes,
378 identified reactions that may control glycolytic fluxes, and uncovered pathway-level flux perturbations
379 under high sugar diet. These analyses were further integrated with other omics data, such as
380 metabolomics and redox proteomics, confirming pathway perturbations and their link to redox-dependent
381 enzyme modifications. Collectively, our *in silico* predictions generate testable hypotheses and
382 prioritize key reactions and pathways for targeted experimental investigation, complementing the
383 precise and tissue-specific genetic tools available in *Drosophila*.

384 Additionally, our tissue-specific GEMs, validated through metabolomics and pathway-level
385 analysis, not only recapitulated known metabolic functions of individual tissue groups, but also revealed
386 distinct tissue metabolism. For instance, fat body and oenocytes exhibited the highest overall reaction
387 numbers, indicating a broad metabolic capacity of these tissues, particularly in carbohydrate and fatty acid
388 metabolism. Conversely, muscle tissue, despite having fewer overall reaction numbers, showed the
389 highest fraction of extracellular transport reactions and enriched reactions in protein degradation and
390 lipoic acid metabolism. This suggests that muscle may serve as a major hub for systemic metabolite
391 exchange and distribution. Indeed, muscle is known to be a major reservoir of amino acids, releasing
392 them into circulation to support other tissue metabolism when needed[67]. As inter-organ communication is
393 essential to maintain whole-body homeostasis and compensate for the limitations of individual tissue
394 functions[2], future studies in evaluating transport reactions and their associated metabolic pathways using
395 these tissue-specific GEMS may reveal additional layers of systemic metabolic coordination among
396 tissues.

397 Moreover, we demonstrated the utility of our tissue-specific GEMs to evaluate muscle
398 metabolism in response to high sugar diet. Our analyses revealed altered NAD(H)-dependent reactions
399 and suggested that regulation of glycolytic flux is distributed among several enzymes, including Aldo and
400 GAPDH. Previous studies recognized GAPDH as a rate-limiting step in glycolysis, particularly in the
401 context of aerobic glycolysis in cancer, where it regulates flux and is influenced by fructose 1,6-
402 bisphosphate levels[68]. Our findings expand this role, demonstrating that GAPDH also acts as a regulatory
403 node in muscle in response to HSD and through redox modifications of the enzyme. While GAPDH is
404 typically known to undergo redox regulation at cysteine residues in response to oxidative stress[26,69], our
405 data also revealed increased methionine oxidation. In fact, methionine oxidation has previously been

shown to affect GAPDH function. For example, Samson et al., demonstrated that oxidation at Met-46 promoted GAPDH aggregation, a process linked to disease[70]. In our study, methionine oxidation occurred near the NAD^+ binding site, which may interfere with cofactor binding and enzymatic activity. Moreover, GAPDH enzyme levels, as well as most other glycolytic enzyme levels, were not significantly altered, indicating a potentially greater role of redox regulation on modulating glycolytic activity in this condition.

Finally, our muscle-GEM enabled predictions of additional dysregulated metabolic pathways, with fructose metabolism among the most substantially perturbed under HSD. While liver, intestine, and kidney are typically considered as primary sites of fructose metabolism due to high ketohexokinase expression, recent evidence showed that muscle can also metabolize fructose and affect muscle glucose handling[71]. Our pathway-level flux analysis predicted muscle could catabolize fructose and showed a significant decrease in the activity of Hex-A, a *Drosophila* hexokinase capable of phosphorylating fructose to fructose-6-phosphate in response to HSD[72]. The accumulation of metabolites such as sorbitol, trehalose and/or sucrose, along with increased oxidation of Trehalase, supported the perturbation of fructose and sucrose metabolism. Yet, these experimental data do not indicate whether fructose catabolic activities were increased or decreased, as elevated concentrations of upstream metabolites can increase flux through mass action. Future studies using fructose isotope tracing will be required to validate the direction and magnitude of flux changes within this pathway.

We acknowledge several limitations in this study. First, the choice of GEM reconstruction algorithm can influence model content and predictive performance[73]. When comparing our tissue-specific GEMs reconstructed through the tINIT algorithm with those generated by CORDA, we found that the final GEMs from CORDA contained fewer reactions and lower metabolic task pass rates compared to those generated by tINIT, but maintained similar metabolic structures for major tissue groups (Error! Reference source not found.**a-c**). This underscores the importance of careful selection and parameter tuning of reconstruction algorithms to minimize potential biases. Second, we acknowledge the challenges of validating all 32 tissue-specific GEMs. Additional context-specific validation will be required to improve model accuracy. Third, using a single pseudo-biomass objective for flux balance analysis may not fully predict tissue- or context-specific flux predictions. Incorporating tailored objectives functions could refine flux predictions across tissues. Fourth, most reactions in the GEMs retained the default flux bounds, representing computational conventions rather than experimentally derived limits. This underscores that our flux predictions are semi-quantitative, given the limited availability of comprehensive in vivo nutrients exchange data. Incorporating high-quality *in vivo* nutrients exchange rates will improve flux prediction accuracy. Finally, certain reactions within fructose metabolism were

438 absent in the current muscle-GEM, highlighting a need for continued curation and targeted data
439 integration to enhance model completeness and flux predictions.

440 In summary, we reconstructed tissue-specific genome-scale metabolic models for *Drosophila* and
441 demonstrated the utility of the muscle-GEM to identify high sugar diet-induced metabolic dysregulation
442 at both reaction and pathway levels. These GEMs provide a quantitative, systems-level framework that
443 further complements the diverse experimental and genetic tools available for *Drosophila*, advancing
444 metabolic investigations in this model organism.

Methods

Genome-scale metabolic model for *Drosophila*

We selected *Fruitfly1* as a base GEM[19], as it offered the comprehensive coverage of reactions (n_{rxn} = 12,308), metabolites (n_{met} = 8,117), and genes (n_{gene} = 1,810) compared to alternative GEMs such as *FlySilico* (n_{rxn} = 363, n_{met} = 293) or *iDrosophila1* (n_{rxn} = 8230, n_{met} = 6990, and n_{gene} = 2388)[17,18].

Update of genes and gene-transcript-protein-reaction associations in Fruitfly1-GEM

Fruitfly1.0 is a generic genome-scale metabolic model describing metabolic networks of *Drosophila melanogaster*[19]. To update the gene information within the model, we first used Gene List Annotation for Drosophila (GLAD) database, containing a metabolic gene set of 2,629 genes (https://www.flyrnai.org/tools/glad/web/, Metabolic_vs3). We compared these genes with those listed in the GEM. We found that 1,465 genes from GLAD were not included. These missing genes included transcription factors, kinases, phosphatases, and dehydrogenases. Before adding those genes directly into Fruitfly1, we evaluated those genes had human orthologs by using DIOPT score[74]. Of 1,465 genes analyzed, 564 genes (38.5 %) were predicted to have human orthologs assigned with a high rank score[74]. Among those, 36 genes were already linked to reactions and gene-rules in human-GEM. Thus, we added these genes into Fruitfly1 (see Supplementary Data). For reactions that already had gene-rules (grRules), we integrated the new genes using the Boolean operator 'or'. To address gene redundancy, we investigated overlapping gene symbols within Fruitfly1 and found that three gene symbols (*Sur/sur, Argk2/CG5144, and Argk/Argk1*) were mapped to the same FlyBase gene IDs. To resolve these redundancies, we retained *Sur* (FBgn0028675)*, Argk2* (FBgn0035957)*, Argk1* (FBgn0000116). Following these updates, we named the revised model Fruitfly2. In summary, we added 36 missing genes (Error! Reference source not found.**a**).

Update the Enzyme Commission number

To update Enzyme commission (EC) numbers, a systematic classification of enzymes based on the reactions, we used KEGG ID to map reactions with EC numbers within the Fruitfly1-GEM. We first examined whether the reactions present in Fruitfly1-GEM were associated with EC numbers and found that 7,411 out of 12,038 reactions (approximately 61.6%) lacked EC number annotations in Fruitfly2. We then assessed whether these reactions had associated KEGG reaction IDs, which could be used to retrieve

475 EC numbers. Only 161 reactions were linked to KEGG reaction IDs, of which 78 were associated with
476 EC numbers. Based on this information, we assigned EC numbers to these 78 reactions. Additionally, by
477 using gene–KEGG reaction ID associations, we assigned EC numbers to a further 576 reactions. In total,
478 we assigned EC numbers to 654 reactions in Fruitfly2 (Error! Reference source not found.**b**),and
479 designated the updated GEM as Fruitfly3.

480

481 Reconstruction of tissue-specific genome-scale metabolic models in *Drosophila*

482 To generate tissue-specific genome-scale metabolic models (GEMs), we integrated Fruitfly3 with tissue-
483 specific pseudo-bulk single-nuclei transcriptomics data for 32 individual tissues from Fly Cell Atlas,
484 while using the Task-driven Integrative Network Inference for Tissues (tINIT) algorithm, implemented
485 via the getINITModel2 function from the Human-GEM repository (Error! Reference source not
486 found.**c**)[7,75]. For generating tissue-specific pseudo-bulk gene expression data, we first retrieved the Seurat
487 objects from Fly Cell Atlas dataset and used *AggregateExpression* function in Seurat to pseudobulk the
488 counts per tissue[76,77]. Gene expression values were converted to counts per million (CPM), rather than
489 TPM or FPKM, by normalizing to library size and scaling by a factor of 1e6[78]. The resulting normalized
490 gene expression values are expressed in unit of CPM. To incorporate these gene expression data as input
491 for tINIT, we applied a global and relaxed expression threshold of 1, selected based on the distribution of
492 average gene expression levels across tissues (mean – 1 × SD = 1.02). This ensured the inclusion of
493 moderately expressed genes while maintaining consistency across all tissues.

494 In addition to transcriptomic data, tINIT requires a set of essential metabolic tasks as inputs.
495 Accordingly, we used a 57 predefined essential metabolic tasks, adapted from prior study (Error!
496 Reference source not found.**d**)[75]. These tasks span key metabolic functions, including rephosphorylation
497 of nucleoside triphosphates, de novo synthesis of nucleotides, uptake of essential amino acids, protein
498 turnover, electron transport chain and TCA, beta oxidation of fatty acids, de novo synthesis of
499 phospholipids, growth based on media components, and synthesis of vitamins and cofactors. Although
500 these tasks were originally designed for human GEM reconstruction, we reviewed available *Drosophila*
501 literature, including KEGG pathway annotations and FlyBase resources, and found no direct evidence that
502 these core tasks would not be performed in *Drosophila*. While we did identify *Drosophila*-specific
503 pathways in the KEGG database, such as dorso-ventral axis formation, insect hormone biosynthesis, and
504 Toll and Imd signaling pathway, we did not include these as essential tasks for reconstruction, as their
505 essentiality has not been validated across all 32 tissues.

To compare the GEM reconstruction outcomes, we also applied the Cost Optimization Reaction Dependency Assessment (CORDA) algorithm[5] to reconstruct tissue-specific GEMs using the same dataset used for tINIT. CORDA categorizes reactions into essential (ES), present (PR), and not present (NP) based on gene expression levels. Specifically, reactions associated with genes expressed above the mean were designated as ES; those with expression between one and the mean as PR; and those less than or equal to 1 as NP.

Metabolic network structure, subsystem coverage, and metabolic task analysis

Metabolic network analysis

The analysis of metabolic network structure, subsystem coverage, and metabolic tasks was performed following a previously established protocol[75]. In brief, to compare model structures, we used *compareMultipleModels* function from the RAVEN package. This function constructs a binary reaction matrix, where rows represent reactions and columns represent individual GEMs. A value of 1 indicates the presence of a reaction in a given GEM, while a value of 0 indicates its absence. For visualization, we applied t-distributed stochastic neighbor embedding (t-SNE) to the binary reaction matrix, using the Hamming distance as the similarity metric. The resulting two-dimensional projection revealed the relative proximity of models based on their metabolic reaction content. Additionally, we performed hierarchical clustering to classify the tissue-specific GEMs. A Euclidean distance matrix was computed from the same binary reaction matrix, followed by average linkage clustering to generate a dendrogram. Cluster assignments were defined by partitioning the dendrogram into a fixed number of groups, capturing major tissue classes such as muscle, fat body/oenocyte, gut, glia, and neurons. These clusters were annotated and visualized in the t-SNE plot.

Quantification of cluster overlap using Jaccard index

To assess the agreement between GEM-derived and gene expression-based tissue clusters, we calculated the Jaccard index. This metric quantifies the similarity between two sets as the size of their intersection divided by the size of their union, ranging from 0 (no overlap) to 1 (complete overlap)[47], as follows:

$$J(A \cap B) = \frac{|A \cap B|}{|A \cup B|}$$

, where A and B represent the sets of tissues assigned to a given cluster based on GEM-derived and gene expression-derived clusters, respectively.

536 We first performed hierarchical clustering on both datasets. For tissue-specific GEMs, clustering was
537 based on the binary reaction presence matrix, as described in the metabolic network analysis method. For
538 gene expression-based clustering, we applied hierarchical clustering to pseudobulk expression data.
539 Jaccard indices were then calculated by comparing each pair of clusters. For glial tissues, which
540 were distributed across three distinct GEM-based clusters, the corresponding Jaccard indices
541 were averaged to represent them as a unified group.

542

543 *Metabolic subsystem coverage analysis*

544 Variation in model structures was further investigated by analyzing the coverage of metabolic subsystems
545 in each tissue-specific GEMs. Subsystem coverage (SC) refers to the total number of reactions present in
546 a specific metabolic subsystem. For each subsystem, the SC was calculated for individual tissue-specific
547 GEMs and compared to the average subsystem coverage across all tissue-specific GEMs (SC_{mean}). The
548 relative deviation from the mean coverage was calculated using the following formula:

549 $$\%\ differences\ in\ subsystem\ coverage = \frac{SC - SC_{mean}}{SC_{mean}} \times 100\ \%$$

550 To facilitate the visualization, we applied a threshold of 100 %, showing only those subsystems in which
551 at least one tissue-GEM exhibited more than 50 % differences from the mean subsystem coverage.

552

553 *Metabolic task analysis*

554 To evaluate and compare each GEM's metabolic functionality, we assessed the ability of each GEM to
555 perform a set of curated 219 metabolic tasks. This list was primarily based on the updated metabolic task
556 collection from Richelle *et al.* (2021)[36], which includes 195 tasks. This list also includes system and
557 subsystem categories. Given the well-characterized role of trehalose metabolism in *Drosophila*, we added
558 eight trehalose biosynthesis tasks with different substrate conditions. Additionally, we compared this
559 updated list with the earlier Human-GEM task set[75]. From this comparison, we added an additional 16
560 tasks related to energy metabolism (eight oxidative phosphorylation, one Krebs cycle, four glycolysis)
561 and carbohydrate metabolism (two glycogen metabolism), resulting in the final list of 219 metabolic tasks
562 (Error! Reference source not found.**k**). For clarity, this list is distinct from the set of 57 essential
563 metabolic tasks used for tissue-specific GEM reconstruction (Error! Reference source not found.**d**).

564 Task performance was evaluated using *checkTasks* function in the RAVEN toolbox. A task was
565 considered "passed" (assigned a value of 1) if the model could carry flux through the required reactions to

566 convert the defined input metabolite(s) into the specified output product(s), indicating that the metabolic
567 function is feasible within the network[79]. Conversely, a task was considered "failed" (assigned a value of
568 0) if no such flux could be achieved, suggesting that the function was not supported by the model.
569 Additionally, we used Fisher's Exact test to evaluate the association between individual tissue-specific
570 GEMs and metabolic systems, defined as groups of functionally related metabolic tasks[36].

571

572 Fly stocks and maintenance

573 All flies were reared at 25°C and 60% humidity with a 12-hour on/off light cycle on standard laboratory
574 food. Standard laboratory food is made as follows: 12.7 g/liter deactivated yeast, 7.3 g/liter soy flour, 53.5
575 g/liter cornmeal, 0.4% agar, 4.2 g/liter malt, 5.6% corn syrup, 0.3% propionic acid, and 1%
576 Tegosept/ethanol. The semi-defined synthetic media for high sugar and normal diet were made according
577 to the previously reported recipe[80], with a slight modification of sugar concentration. The normal diet
578 (NSD) consisted of 10 g/L of agar, 80 g/L of yeast, 20 g/L of yeast extract, 20 g/L of peptone, 262 mM of
579 sucrose, 0.3% propionic acid, and 1% Tegosept/ethanol. The high sugar diet (HSD) consisted of the same
580 amount of all the components except 1 M of sucrose. For diet intervention experiments, we collected 3
581 days old w^{1118} male flies and transferred approximately 30 flies to vials containing either NSD or HSD.
582 The food was replaced every two days. Bloomington *Drosophila* stock center (BDSC): attp40 (36304)
583 and UAS-GAPDH1 RNAi (62212). Laboratory stocks: w^{1118}. w; tub-gal80[TS]; MHC-gal4/ TM6b.

584

585 Intracellular metabolites extraction and LC/MS analysis

586 Metabolites quantification in *Drosophila* were adapted from a published protocol[81,82]. 20 thoraces, head,
587 gut, and abdomen were dissected in ice-cold 0.9% normal saline buffer after placing the flies under light
588 CO2 anesthesia. Dissected thoraces were immediately placed in 1.5 mL tubes in dry ice. 450 µL of cold
589 80% (v/v) aqueous methanol were added to the tubes, and intracellular metabolites were extracted by
590 homogenizing tissues with pellet pestle for 1 minute by repeating a cycle of 20 seconds of grinding and
591 10 seconds of break. Samples were centrifuged at maximum speed for 10 minutes in the cold room.
592 Supernatants were transferred to a new 1.5 mL tube, pelleted by vacuum centrifugation using speedvac
593 and stored in -80 °C until mass-spectrometry analysis.

594 Samples were re-suspended using 22 µL HPLC grade water for mass spectrometry. 5-7 µL were
595 injected and analyzed using a hybrid 6500 QTRAP triple quadrupole mass spectrometer (AB/SCIEX)
596 coupled to a Prominence UFLC HPLC system (Shimadzu) via selected reaction monitoring (SRM) of a

597 total of 300 endogenous water soluble metabolites for steady-state analyses of samples. Some metabolites
598 were targeted in both positive and negative ion mode for a total of 311 SRM transitions using
599 positive/negative ion polarity switching. ESI voltage was +4950V in positive ion mode and –4500V in
600 negative ion mode. The dwell time was 3 ms per SRM transition and the total cycle time was 1.55
601 seconds. Approximately 9-12 data points were acquired per detected metabolite. For targeted 13C flux
602 analyses, isotopomers from ~140 polar molecules were targeted with a total of 460 SRM transitions.
603 Samples were delivered to the mass spectrometer via hydrophilic interaction chromatography (HILIC)
604 using a 4.6 mm i.d x 10 cm Amide XBridge column (Waters) at 400 µL/min. Gradients were run starting
605 from 85% buffer B (HPLC grade acetonitrile) to 42% B from 0-5 minutes; 42% B to 0% B from 5-
606 16minutes; 0% B was held from 16-24 minutes; 0% B to 85% B from 24-25 minutes; 85% B was held for
607 7 minutes to re-equilibrate the column. Buffer A was comprised of 20 mM ammonium hydroxide/20 mM
608 ammonium acetate (pH=9.0) in 95:5 water:acetonitrile. Peak areas from the total ion current for each
609 metabolite SRM transition were integrated using MultiQuant v3.2 software (AB/SCIEX).

610

611 Metabolites profiling data analysis

612 Statistical analysis was performed using MetaboAnalystR[46]. The hierarchical clustering analysis and
613 heatmap was generated using *PlotHeatMap* function, in which *hclust* function used to normalize the data
614 across the samples and the Euclidean distance and ward.d were used as parameters for clustering
615 algorithm. Principal component analysis was performed using *PCA.anal* function. In comparison of the
616 means of the normalized metabolite peaks, the Anova test was used using *ggpubr* package in R. For
617 evaluation of the normalized metabolites peak areas, the peak areas were normalized to the protein mass
618 of individual tissues.

619

620 KEGG over-representation analysis for metabolomics

621 To identify pathway-level metabolic changes, we performed over-representation analysis (ORA) using
622 KEGG pathway annotations[63]. First, we constructed a reference pathway and metabolite database by
623 utilizing the *keggrest* R package, retrieving all *D. melanogaster* pathways (e.g., dme00010, dme00020,
624 etc) via *keggList*, and extracting associated metabolites for each pathway using *keggGet*, removing
625 duplicate metabolites to create a unique reference compound list. A total of 105 *Drosophila* pathways and
626 their associated compounds were compiled to serve as the reference database for subsequent over-
627 representation analysis. Region-specific metabolomics data, containing KEGG IDs from MetaboAnalyst,

were then analyzed through ANOVA testing for significant metabolite alterations across regions. Log_2 fold changes (log_2FC) were calculated relative to the mean intensity of other tissues, and metabolites with $p < 0.05$ and $log_2FC > 0.5$ were considered significantly enriched. For the abdomen, due to lower metabolite coverage, a relaxed threshold $log_2FC > 0$ was used, maintaining comparable input metabolite sizes compared to other regions. ORA was conducted using a hypergeometric test to calculate statistical overrepresentation, comparing altered metabolites against the background of all detected metabolites, with Benjamini-Hochberg adjustment for multiple testing, considering pathways with adjusted $p < 0.05$ as significantly enriched pathways. Enrichment results were visualized as bubble plots, with bubble size representing the enrichment ratio (the proportion of observed significant metabolites within a pathway relative to the expected proportion based on the reference dataset) and color indicating log-transformed adjusted p-values.

Quantification of pathway overlap using weighted Jaccard index

To evaluate the degree of overlap between metabolomics-derived enriched pathways and those predicted by tissue-specific genome-scale metabolic models (GEMs), we calculated a weighted Jaccard index. A traditional Jaccard index measures the similarity between two sets as the size of their intersection divided by their union[47]. We extended this to incorporate significance derived from metabolomics data, allowing pathways with stronger statistical support to contribute more to the similarity score[48]. For each experimentally enriched pathway, we assigned a weight based on the negative log_{10} of its adjusted p-value ($-log_{10}(q)$), normalized across all pathways within each region. For GEM-based enriched pathways, we determined pathways with reaction content above the median across tissues as the enriched pathways. For each region–tissue pair, the weighted Jaccard index was calculated as:

$$J_{weighted}(A,B) = \frac{\sum_{i \in A \cap B} min\ (w_A(i), w_B(i))}{\sum_{i \in A \cup B} max\ (w_A(i), w_B(i))}$$

, where:

A and B are the sets of enriched pathways in the experimental region and predicted tissue-specific GEMS, respectively;

$w_A(i)$ refers to the normalized significance weights assigned to pathway i from experimentally determined enriched pathways for region A, calculated as $w_A(i) = \frac{-\log_{10}(q_i)}{\sum_{j \in A} -\log_{10}(q_j)}$, where q_i is the adjusted p-value for pathway *i*. For any pathway *i* that is not part of set A (e.g., $i \in A \cup B$ and $i \notin A$), $w_A(i) = 0$. The sum of all $w_A(i)$ equals 1;

658 $w_B(i)$ refers to the normalized weights assigned to GEM-based enriched pathways. Since the enriched
659 pathways identified from GEM do not have statistical significance values, each pathway i in set B is
660 assigned an equal weight, calculated as $w_B(i)$=1/n_B, where n_B is the number of enriched pathways in that
661 tissue-specific GEM (set B). For any pathway i that is not part of set B (e.g., $i \in A \cup B$ and $i \notin B$), $w_B(i)$
662 = 0. The sum of all $w_B(i)$ equals 1.

663 To assess the statistical robustness of the weighted Jaccard index, we performed 10,000 bootstrap
664 resampling of the experimental enriched pathway dataset. For each bootstrap iteration, enriched pathways
665 were randomly sampled, and the weighted Jaccard index was recalculated against model-predicted tissue-
666 specific enriched pathways. This generated a distribution of indices for each region-tissue pair. We then
667 used one-way ANOVA followed by Bonferroni-corrected post-hoc tests to determine whether a specific
668 region (e.g., thorax) exhibited significantly higher similarity to a given tissue GEM (e.g., Muscle-GEM)
669 compared to other regions. Significance levels were visualized on box plots to highlight region-specific
670 alignment between experimental data and model predictions.

671

672 Definition of HSD-muscle-GEM

673 We defined a high sugar diet (HSD)-muscle-GEM by constraining reaction rates to recapitulate
674 key known features of type 2 diabetic muscle based on the literature evidence[28,29,33,34,52–54]. These
675 constraints included reduced upper bounds of reactions rates in glucose uptake, glyceraldehyde-3-
676 phosphate dehydrogenase, citrate synthase, oxoglutarate dehydrogenase, succinate dehydrogenase, and
677 fumarate hydratase (Error! Reference source not found.**a**). Since *Drosophila* also utilizes trehalose as a
678 fuel source, and its circulating levels increase in response to HSD[13,83], we also constrained the upper
679 bounds of trehalose uptake rates. Because glycolysis and TCA cycle activities are closely linked to
680 NAD(P)H redox metabolism[56], we updated reaction directionality of redox-related reactions based on
681 supporting evidence from the literature[9,84–89] (Error! Reference source not found.**a**). Furthermore, to focus
682 the model on metabolic pathways relevant to our measured metabolites, we constrained the upper bounds
683 of exchange rates for the undetected metabolites to one tenth of the default upper bound (Error! Reference
684 source not found.**b**). Lastly, given the muscle tissue serving as a major tissue for energy and redox
685 metabolism, we included artificial demand reactions for ATP production under HSD, NAD^+ regeneration,
686 and NADPH regeneration. These reactions reflect fundamental physiological needs of muscle in
687 *Drosophila*: ATP production was required for flight[90], NAD^+ regeneration to sustain glycolysis[91], and
688 NADPH regeneration to mitigate oxidative stress[92,93]. While we originally intended to use these reactions
689 as objective functions, similar to prior approaches modeling energy and redox metabolism[84,94], they were

not used as objectives in our FBA simulations of HSD-muscle-GEM, but were still retained as auxiliary buffer reactions for energy and cofactor metabolism. Simulations were performed using a biomass objective function (reaction ID: *MAR00021*), which captures broad metabolic maintenance and biosynthesis requirements of muscle tissue. Details of this objective function are provided in the Flux Balance Analysis section.

Flux balance analysis

Flux balance analysis (FBA) was performed to determine the optimal metabolic flux distributions that maximizes a defined objective function, while satisfying stoichiometric constraints under steady state assumption[95]. A metabolic network is represented by a stoichiometric matrix S of size m × n, in where m and n represents the number of metabolites and reactions, respectively. The elements in S_{ij} corresponds to the stoichiometric coefficient of metabolites i in reaction j. The relationship between metabolites and reaction rates is given by the following equation:

$$S\mathbf{v} = \frac{d\mathbf{m}}{dt}$$

, where $\mathbf{v}$ is the n × 1 vector of reaction rate vector and $\mathbf{m}$ is an m × 1 vector of metabolite concentrations. Under the steady-state assumption, the concentration of metabolites does not change over time, making the right side equal to 0. FBA solves a linear optimization problem to determine flux distributions that satisfy this constraint, formulated as:

$$\text{maximize } \mathbf{c}^T\mathbf{v},$$

$$\text{subject to } \mathrm{S}\mathbf{v} = 0,$$

$$\text{and } \mathbf{v}_{\mathbf{min}} \leq \mathbf{v} \leq \mathbf{v}_{\boldsymbol{max}}$$

, where

S : Stoichiometry matrix (m × n)

v : flux vector representing reaction rates at steady state (v ∈ R^n)

c : vetor defining the linear objective function

$\mathrm{v}_{min}, \mathrm{v}_{max}$: Lower and upper bounds for each flux

715 For FBA simulations, we used a biomass objective function (reaction ID:*MAR00021*), which
716 aggregates the demand for key metabolic precursors — including amino acids (e.g., alanine, glutamine,
717 valine), lipids (e.g., cholesterol, lipid droplets), glycogen, nucleotides (DNA, RNA), and metabolic pools
718 (e.g., phospholipids, cofactors, vitamins) — into a single pseudo-biomass reaction, as follows:

719 $$CL_{pool}[c] + DNA[n] + DNA\text{-}methylcytosine[n] + PI\ pool[c] + RNA[c] + SM\ pool[c] + alanine[c]$$
720 $$+ arginine[c] + asparagine[c] + aspartate[c] + cholesterol[c] + cholesterol$$
721 $$- ester\ pool[r] + cofactors\ and\ vitaminc\ [c] + cysteine[c] + glutamate[c]$$
722 $$+ glutamine[c] + glycine[c] + glycogen[c] + histidine[c] + isoleucine[c]$$
723 $$+ leucine[c] + lipid\ droplet[c] + lysine[c] + methionine[c] + phenylalanine[c]$$
724 $$+ phosphatidate\text{-}LD\text{-}TAG\ pool[c] + proline[c] + serine[c] + threonine[c]$$
725 $$+ tryptophan[c] + tyrosine[c] + valine[c] \rightarrow biomass[c]$$

726 This formulation was used here as a general proxy for basal cell maintenance, including protein
727 turnover, membrane lipid remodeling, and nucleotide recycling. These processes remain active and
728 physiologically relevant to tissues like muscle[67,96,97]. Thus, rather than using energy and redox demands as
729 sole objective functions, which could bias the solution space or do not recapitulate other core metabolic
730 activities, we adopted this biomass objective function to capture broader metabolic requirements. The
731 resulting flux through this reaction was approximately 1.1 (arbitrary unit). While this value represents the
732 demand for cell biosynthesis and maintenance, the energetic and precursor requirements for synthesizing
733 biomass are distributed among the various reaction fluxes throughout the metabolic network.

734

735 Flux variability analysis

736 Flux Variability Analysis (FVA) was used to evaluate the range of feasible fluxes for each reaction under
737 sub-optimal conditions, characterizing the flexibility of individual reactions[98]. FVA involves solving two
738 optimization problems—one to maximize and one to minimize each flux v_i of interest,

739 $$\text{maximize / minimize } v_i,$$

740 $$\text{subject to } S\mathbf{v} = 0,$$

741 $$\mathbf{c}^T\mathbf{v} \geq \alpha \times z_{common,opt},$$

742 $$\text{and } \mathbf{v_{min}} \leq \mathbf{v} \leq \mathbf{v}_{max}$$

743 , where α is the optimality parameter ($0 \leq \alpha \leq 1$), where α = 1 corresponds to the fully optimal solution
744 obtained from FBA. In this study, we set α = 0.9 to allow a small deviation from the optimal solution,
745 enabling exploration of alternative flux distributions that are biologically plausible while still near-
746 optimal. We used flux variability analysis to probe the range of fluxes (differences between Vmax and
747 Vmin) as a measure of feasible flux range, not as a proxy for statistical uncertainty.

748

749 Flux sampling analysis

750 We performed flux sampling analysis after unconstrained reaction bounds with the minimum and
751 maximum flux values obtained from flux variability analysis (FVA). To explore the feasible solution
752 space, we applied the *GpSampler* algorithm, which implements the Artificial Centering Hit-and-Run
753 (ACHR)[99]. A total of 10,000 randomly sampled flux distributions were generated using uniformly
754 distributed initial points.

755

756 Parsimonious flux balance analysis (pFBA)

757 Parsimonious enzyme usage flux balance analysis (pFBA) is a commonly used extension of standard flux
758 balance analysis that identifies flux distributions with minimal total flux while achieving the optimal
759 value of a specified objective (e.g., biomass production)[100]. The rationale is that cells are expected to
760 minimize enzyme usage and avoid unnecessary internal cycling, leading to more realistic and
761 interpretable flux predictions. It uses a bilevel optimization in which the objective function is first
762 optimized using FBA, followed by the minimization of total flux through all gene-associated reactions.
763 The second part of the optimization is expressed as follows:

764 $$\min \sum_{j=1}^{m} v_{irrev,j}$$

765 $$s.t.\, v_{objective,lb} = v_{objective,FBA},$$

766 $$S_{irrev} * \mathbf{v_{irrev}} = 0$$

767 $$0 \leq v_{irrev,j} \leq v_{max}$$

768 ,where m is the number of irreversible reactions in the network, $v_{objective,FBA}$ is the optimal flux value
769 obtained from FBA and $v_{objective,lb}$ is the lower bound for the objective function for the second
770 optimization problem.

Differential flux analyses

To identify reactions with altered fluxes between HSD and NSD conditions, we calculated the difference in flux values for each reaction across FBA, pFBA, and FVA_sampling analyses. Flux values from FBA and pFBA represent single optimal solutions, whereas for FVA_sampling, median flux values across the sampling points were used as a representative flux value. Reactions were classified as increased or decreased based on a flux difference threshold of ±1, which can be adjusted for stringency. This analysis produced three independent sets of perturbed reactions for each method. Then, we identified the commonly perturbed reactions shared across all three methods and visualized their overlaps using *UpSet* and *ggvenn* functions in R. For these shared reaction sets, we assigned each reaction to its corresponding subsystem and associated gene(s). Within each direction (increased or decreased), the top three subsystems with the largest numbers of perturbed reactions were selected. Gene–subsystem relationships were visualized as bipartite network graphs, where node size corresponds to the number of associated reactions and edge width represents the number of shared genes between subsystems and reactions. Networks were generated using the *igraph* (v1.3.5) and *ggraph* (v2.1.0) in R.

For FVA-sampling analysis of NAD(H)-dependent reactions, we additionally performed two-sample Z-tests to evaluate the statistical significance of flux changes between NSD and HSD conditions[101]. Z-score was calculated as follows:

$$Z_i = \frac{\bar{X}_{HSD}(v_i) - \bar{X}_{NSD}(v_i)}{\sqrt{\frac{\sigma^2_{HSD}(v_i)}{n_{HSD}} + \frac{\sigma^2_{NSD}(v_i)}{n_{NSD}}}}$$

, where i represents each reaction, $\bar{X}_{cond}(v_i)$ is the average of the sampled fluxes of each reaction for condition (NSD or HSD), $\sigma^2_{cond}(v_i)$ is the sample variance, and n_{cond} is the number of flux samples per condition. Two-tailed p-values were computed using the standard normal cumulative distribution function, and Bonferroni correction was applied to adjust for multiple testing.

Evaluation of maximum NADH production capacity

To assess the network's maximum NADH production capacity, we introduced an artificial total NADH demand reaction ($\mathrm{NADH} \rightarrow \mathrm{NAD^+} + \mathrm{H^+}$) accounting for relevant compartments (cytosol, mitochondria, and peroxisome) into the muscle-GEM. Specifically, the reaction is represented as:

$$\begin{aligned} &\mathrm{NADH[c]} + \mathrm{NADH[m]} + \mathrm{NADH[p]} \\ &\rightarrow \mathrm{NAD^+[c]} + \mathrm{H^+[c]} + \mathrm{NAD^+[m]} + \mathrm{H^+[m]} + \mathrm{NAD^+[p]} + \mathrm{H^+[p]} \end{aligned}$$

, where [c], [m], and [p] refer to the cytosol, mitochondria, and peroxisome, respectively. As solely maximizing the NADH demand reaction may yield biologically nonviable solutions, we first performed FBA by maximizing the original pseudo-biomass objective function[84]. Then, we set the lower bounds of this reaction at 50% of the optimized solution and performed pFBA to maximize the NADH demand reaction.

Sensitivity analysis

To assess the control of individual glycolytic reactions on overall pathway flux, we performed a sensitivity analysis. This analysis is conceptually analogous to metabolic control analysis, where flux control strength is quantified as the relative change in pathway output flux in response to variations in individual enzyme activities[102,103]. It also aligns with general sensitivity analyses of reaction rates used in reaction networks[85,104]. For each glycolytic reaction, the baseline flux was defined as the median flux of 5,000 sampling data obtained from FVA. Then, each reaction was perturbed by constraining its flux to 95%, 90%, 70%, and 50% of the baseline, and FVA-sampling was repeated to obtain the perturbed flux distributions. The total pyruvate consumption flux was used as a proxy for glycolytic output flux, because unlike mammalian systems where lactate production rate by lactate dehydrogenase (LDH) is commonly used as the glycolytic output, LDH activity is relatively low in insect muscle[105], and pyruvate is substantially converted for the production of other metabolites such as alanine and acetate[106,107]. The normalized sensitivity coefficient (S_i) was calculated as follows:

$$Normalized\ sensitivity\ coefficient\ (S_i) = \frac{\Delta v_{total_pyr_con}}{\Delta v_i} \times \frac{v_{i,base}}{v_{total_pyr_con,base}}$$

,where $v_{total_pyr_con,base}$ represents the sum of fluxes through all pyruvate-consuming reactions at baseline, $\Delta v_{total_pyr_con}$ represents the difference in the summed flux of all pyruvate-consuming

825 reactions between the baseline and perturbed states, v_i represents the baseline flux of with glycolytic
826 reaction, and Δv_i represents the difference in flux of the ith reaction between the baseline and perturbed
827 states.

828

829 Pathway-level flux analysis

830 To evaluate the pathway-level flux changes and statistical significance between NSD and HSD
831 conditions, we defined pathway flux (V_i) as the average of non-zero flux magnitudes within each
832 pathway. For FVA_sampling analysis, we used 10,000 flux sampling points per condition and performed
833 a two-sample Z-test, adapting the approach from a previous study[101]:

834
$$Z_i = \frac{\bar{X}_{HSD}(V_i) - \bar{X}_{NSD}(V_i)}{\sqrt{\frac{\sigma^2_{HSD}(V_i)}{n_{HSD}} + \frac{\sigma^2_{NSD}(V_i)}{n_{NSD}}}}$$

835 , where i represents each pathway, $\bar{X}_{cond}(V_i)$ is the average of the pathway flux across all sampling points
836 for condition (NSD or HSD), $\sigma^2_{cond}(V_i)$ is the sample variance of pathway flux across all sampling points
837 for each condition, and n_{cond} is the number of flux sampling points per condition. Two-tailed p-values
838 were computed using the standard normal cumulative distribution function. For pFBA, which yields a
839 single optimal flux solution per condition, no statistical test was performed and pathway flux changes
840 were quantified using the log2 fold change between HSD and NSD.

841

842 ^{13}C-isotopic labeling experiments and mass isotopomer analysis

843 We prepared the normal and high sugar diet with 13 mM and 50 mM of [U-$^{13}C_6$]glucose (Cambridge
844 Isotope Laboratories, Inc. CLM-1396), respectively, maintaining the molar ratio of the labeled glucose to
845 sucrose consistent. For ^{13}C-isotopic labeling experiments, we collected 3 days old w^{1118} male flies and
846 placed approximately 30 flies in vials containing either NSD or HSD with isotope tracers at room
847 temperature. The food was replaced every two days. On day five, twenty thoraces were dissected per
848 biological replicate and intracellular metabolites were extracted using 80% (v/v) aqueous methanol.
849 Q1/Q3 SRM transitions for incorporation of 13C-labeled metabolites were established for polar
850 metabolite isotopomers, and data were acquired by LC-MS/MS. Peak areas were generated using
851 MultiQuant version 2.1 software. The natural isotope abundance was corrected using AccuCor (Github:
852 https://github.com/XiaoyangSu/AccuCor)[108].

853

854 Switch-tagging redox proteomics

855 Muscle tissues were solubilized in 4% SDS in 100mM triethylammonium bicarbonate (TEAB) pH 7.0
856 lysis buffer and digested using S-Trap micro columns (Protifi, Huntington, NY) following the
857 manufacturer's procedure. Each sample was loaded onto individual Evotips for desalting and washing.
858 The Evosep One system (Evosep, Odense, Denmark) was used to separate peptides on a Pepsep colum
859 (150 um inter diameter, 15 cm) packed with ReproSil C18 1.9 um, 120A resin using pre-set 15 samples
860 per day gradient. The system was coupled to the timsTOF Pro mass spectrometer (Bruker Daltonics,
861 Bremen, Germany) via the nano-electrospray ion source (Captive Spray, Bruker Daltonics). Raw data
862 files conversion to peak lists in the MGF format, downstream identification, validation, filtering and
863 quantification were managed using FragPipe version 13.0. MSFragger version 3.0 was used for database
864 searches against a *Drosophila* database with decoys and common contaminants added.

865

866 Prediction of *Drosophila* GAPDH protein complexes using AlphaFold-Multimer

867 For the prediction of protein complexes using AlphaFold-Multimer (AFM), we employed
868 LocalColabFold version 1.5.2[109]. It integrates AFM version 2.3.1[110] and utilizes MMseqs2 for generating
869 multiple sequence alignments. Computations were performed on the Harvard O2 high-computing cluster.
870 Our prediction involved five models for each complex, each undergoing five recycling iterations. The
871 model displaying the highest prediction quality was selected for each protein complex. The protein
872 complexes examined in this study include *Drosophila* GAPDH1 homodimer, GAPDH1:GAPDH2
873 heterodimer, and GAPDH2 homodimer. The prediction results have been made publicly available on the
874 Fly Predictome website (https://www.flyrnai.org/tools/fly_predictome/web/)[111]. For visualization of the
875 predicted structures we utilized ChimeraX[112].

876

877 KEGG over-representation analysis (ORA) for redox proteomics

878 Similar to the metabolomics-based ORA analysis, we conducted KEGG over-representation analysis
879 using proteins with significantly altered oxidation states. Significantly altered peptides of proteins were
880 identified by calculating the $\log_2$ fold change between high sugar diet and normal sugar diet conditions.
881 Statistical significance was determined using an unpaired two-sample t-test, with p-values corrected for
882 multiple testing using the Benjamini-Hochberg (FDR) method. Proteins were considered significantly

883 altered if they met the thresholds of $\log_2|FC| > 0.5$ and adjusted p-value < 0.05. After obtaining a list of
884 significantly altered protein sets, we performed KEGG overrepresentation analysis using the
885 *clusterProfiler* R package. First, protein names were converted to gene symbols. Next, these gene
886 symbols were mapped to entrez IDs using the *bitr* function in the *org.Dm.eg.db* database. Only unique
887 Entrez Gene IDs were retained for downstream analysis. Finally, overrepresentation analysis was
888 performed using the *enrichKEGG* function. The enrichment results were visualized using dot plots using
889 *dotplot* function.

890

891 Climbing assay

892 Flies were tested for vertical climbing ability at day 5 and 10[82,113]. In this assay, male flies separated by
893 genotypes were transferred to empty vials. Flies were tapped three times and observed for 10 seconds.
894 The percentage of flies that climbed above 5 cm was recorded. Consecutive trials were separated by 30
895 seconds of rest.

896

897 RNA extraction and qRT-PCR

898 RNA was extracted and analyzed by qRT-PCR[49]. Five thoraces were collected per sample. Samples were
899 homogenized in TRIzol reagent (Ambion). The RNAs were isolated and purified using Direct-zol RNA
900 MicroPrep columns (Zymo Research) according to the manufacturer instructions. Reverse transcription
901 was done by using iScript cDNA Synthesis Kit (Bio-Rad)**.** qRT-PCR was done in a CFX96 Real-Time
902 System (Bio-Rad) using iQ SYBRGreen Supermix (Bio-Rad). Relative mRNA levels were calculated
903 using the ΔΔCt method. For thoraces, values were normalized to the housekeeping gene a-tubulin84.

904

905 Quantification of cellular NADH/NAD$^+$

906 Measurements of NADH/NAD$^+$ was adapted from a published protocol[86], using the NADH/NAD$^+$ Glo
907 Assay (Promega: G9071, G9072) with a modification in manufacturer instruction. In brief, five thoraces
908 were dissected, weighted, and stored in 1.5 mL tubes in dry ice. 300 µL of PBS with 1 % DTAB solution
909 was added the tubes and the thoraces were homogenized with the pellet and homogenizer. 110 µL of the
910 cell lysates were split into two separate ice-cold 1.5 mL tubes: one for NADH and the other for NAD$^+$.
911 For NADP$^+$ tube, 55 µL of 0.4 M HCl with 1 mM ascorbate were added. We added ascorbic acid to
912 prevent the oxidation of NADH into NAD$^+$ under low pH, avoiding the overestimation of intracellular

913 NAD^+ levels[114]. The other NADH tube remained untreated. Both tubes were placed into the heat block
914 with 60 °C temperature for 20 minutes to destroy NAD^+. Tubes were equilibrated at room temperature for
915 10 minutes. 55 μL 0.5 M Trizma/base was added to the NAD^+ tubes to neutralize the acid, while 110 μL
916 of HCl/ascorbate/base buffer was added to the untreated NADH tube. Afterwards, NADH, NAD^+, and the
917 ratio were measured following the manufacturer's instruction with the generation of standard curves with
918 known concentration.

919

920 Data analysis, statistics, and reproducibility

921 Statistical analyses were performed in GraphPad Prism (v9.5.1), MATLAB (2020b), or R (4.2.1). For
922 analysis of two groups, including metabolomics, isotope tracing, and redox-proteomics between HSD and
923 NSD conditions, Welch's unequal variances two-sided t-test was used to calculate a p-value. For
924 metabolomics data involving multiple group comparisons, one-way ANOVA was conducted followed by
925 Benjamini-Hochberg (BH) correction for controlling the false discovery rate (FDR). The significance was
926 represented as follows: $*$ $P < 0.05$, $**$ $P < 0.01$, $***$ $P < 0.001$, $****$ $P < 0.0001$. In pathway
927 enrichment analyses, hypergeometric tests were applied to identify over-represented pathways. To
928 account for multiple comparisons, p-values were adjusted for false discovery rate (FDR) using the
929 Benjamini-Hochberg (BH) method. For weighted Jaccard index analyses, pathway enrichment data were
930 bootstrap-resampled (n = 10,000) and analyzed using one-way ANOVA, followed by Bonferroni-
931 corrected pairwise comparisons relative to a predefined reference region. For correlation analyses
932 between model-generated flux changes and metabolite or proteomic measurements, Pearson's correlation
933 coefficient (*r*) and associated *p*-values were calculated. For model-generated flux sampling analysis, the
934 Mann–Whitney U test (ranksum test) was used to compare flux distributions between NSD and HSD
935 conditions, as the distributions are not assumed to be normal. Significance levels were indicated in the
936 boxplots. No samples or data points were excluded from statistical analysis. All analyses from
937 experimental data were based on biologically independent replicates. The statistical methods used for
938 each analysis are described in the corresponding figure legends or methods sections.

939

940 Data Availability

941 All data generated in this study, including ^{13}C-glucose isotope tracing, high-sugar-diet (HSD)
942 metabolomics, regional metabolomics, and redox proteomics, are provided in the Source Data. Processed

943 and analyzed data are provided in Supplementary Data. Source Data and Supplementary Data are
944 provided with this paper.

945

946 Code Availability

947 MATLAB and R scripts used for reconstruction of genome-scale metabolic models and flux analyses are
948 available on GitHub (https://github.com/sunjjmoon/FlyTissueGEMs). An achieved version of the code
949 used in this study is available on Zenodo: doi.org/10.5281/zenodo.17684286[115].

950

951 References

952 1. Droujinine, I. A. & Perrimon, N. Interorgan Communication Pathways in Physiology : Focus on
953 Drosophila. *Annu. Rev. Genet.* **50**, 539–570 (2016).

954 2. Priest, C. & Tontonoz, P. Inter-organ cross-talk in metabolic syndrome. *Nat. Metab.* **1**, 1177–1188
955 (2019).

956 3. Yilmaz, L. & Walhout, A. J. M. A Caenorhabditis elegans Genome-Scale Metabolic Network
957 Model. *Cell Syst.* **2**, 297–311 (2016).

958 4. Yilmaz, L. S. *et al.* Modeling tissue-relevant Caenorhabditis elegans metabolism at network,
959 pathway, reaction, and metabolite levels. *Mol. Syst. Biol.* **16**, 1–20 (2020).

960 5. Schultz, A. & Qutub, A. A. Reconstruction of Tissue-Specific Metabolic Networks Using
961 CORDA. *PLoS Comput. Biol.* **12**, 1–33 (2016).

962 6. Wang, Y., Eddy, J. A. & Price, N. D. Reconstruction of genome-scale metabolic models for 126
963 human tissues using mCADRE. *BMC Syst. Biol.* **6**, 1–16 (2012).

964 7. Agren, R. *et al.* Identification of anticancer drugs for hepatocellular carcinoma through
965 personalized genome-scale metabolic modeling. *Mol. Syst. Biol.* **10**, 1–13 (2014).

966 8. Agren, R. *et al.* Reconstruction of genome-scale active metabolic networks for 69 human cell
967 types and 16 cancer types using INIT. *PLoS Comput. Biol.* **8**, e1002518 (2012).

968 9. Metallo, C. M. & Vander Heiden, M. G. Understanding Metabolic Regulation and Its Influence on

969 Cell Physiology. *Mol. Cell* **49**, 388–398 (2013).

970 10. Jang, C. & Sheng Hui, Xianfeng Zeng, Joseph H. Gorman III, Robert C. Gorman, J. D. R.
971 Metabolite Exchange between Mammalian Organs Quantified in Pigs Resource. *Cell Metab.* **30**,
972 594–606 (2019).

973 11. Chatterjee, N. & Perrimon, N. What fuels the fly: Energy metabolism in Drosophila and its
974 application to the study of obesity and diabetes. *Sci. Adv.* **7**, 1–15 (2021).

975 12. Ugur, B., Chen, K. & Bellen, H. J. Drosophila tools and assays for the study of human diseases.
976 *DMM Dis. Model. Mech.* **9**, 235–244 (2016).

977 13. Dam, E. Van, Santos, E., Franke, A., Kaleta, C. & Cocheme, H. M. Sugar-Induced Obesity and
978 Insulin Resistance Are Uncoupled from Shortened Survival in Drosophila. *Cell Metab.* **31**, 710–
979 725 (2020).

980 14. Musselman, L. P. *et al.* A high-sugar diet produces obesity and insulin resistance in wild-type
981 Drosophila. *Dis. Model. Mech.* **849**, 842–849 (2011).

982 15. Parkhitko, A. A. *et al.* Downregulation of the tyrosine degradation pathway extends drosophila
983 lifespan. *Elife* **9**, 1–27 (2020).

984 16. Kwon, Y. *et al.* Systemic Organ Wasting Induced by Localized Expression of the Secreted Insulin
985 / IGF Antagonist ImpL2. *Dev. Cell* **33**, 36–46 (2015).

986 17. Schönborn, J. W., Jehrke, L., Mettler-Altmann, T. & Beller, M. FlySilico: Flux balance modeling
987 of Drosophila larval growth and resource allocation. *Sci. Rep.* **9**, 1–16 (2019).

988 18. Cesur, M. F., Basile, A., Patil, K. R. & Çak, T. A new metabolic model of Drosophila
989 melanogaster and the integrative analysis of Parkinson's disease. *Life Sci. Alliance* **6**, 1–21 (2023).

990 19. Wang, H. *et al.* Genome-scale metabolic network reconstruction of model animals as a platform
991 for translational research. *Proc. Natl. Acad. Sci. U. S. A.* **118**, e2102344118 (2021).

992 20. D'Alessandro, A. *et al.* Omics markers of the red cell storage lesion and metabolic linkage. *Blood*
993 *Transfus.* **15**, 137–144 (2017).

994 21. Jang, C., Chen, L. & Rabinowitz, J. D. Leading Edge Primer Metabolomics and Isotope Tracing.
995 *Cell* **173**, 822–837 (2018).

996 22. Dong, W., Rawat, E. S., Stephanopoulos, G. & Abu-Remaileh, M. Isotope tracing in health and
997 disease. *Curr. Opin. Biotechnol.* **76**, 102739 (2022).

998 23. Antoniewicz, M. R. A guide to 13C metabolic flux analysis for the cancer biologist. *Exp. Mol.*
999 *Med.* **50**, 1–13 (2018).

1000 24. Xiao, H. *et al.* A Quantitative Tissue-Specific Landscape of Protein Redox Regulation during
1001 Aging. *Cell* **180**, 968-983.e24 (2020).

1002 25. Jones, D. P. & Sies, H. The Redox Code. *Antioxid. Redox Signal.* **23**, 734–746 (2015).

1003 26. Talwar, D. *et al.* The GAPDH redox switch safeguards reductive capacity and enables survival of
1004 stressed tumour cells. *Nat. Metab.* **5**, 660–676 (2023).

1005 27. Gallogly, M. M. & Mieyal, J. J. Mechanisms of reversible protein glutathionylation in redox
1006 signaling and oxidative stress. *Curr. Opin. Pharmacol.* **7**, 381–391 (2007).

1007 28. DeFronzo, R. A. & Tripathy, D. Skeletal muscle insulin resistance is the primary defect in type 2
1008 diabetes. *Diabetes Care* **32**, 157–163 (2009).

1009 29. Gaster, M., Nehlin, J. O. & Minet, A. D. Impaired TCA cycle flux in mitochondria in skeletal
1010 muscle from type 2 diabetic subjects: Marker or maker of the diabetic phenotype. *Arch. Physiol.*
1011 *Biochem.* **118**, 156–189 (2012).

1012 30. Jensen, M. V. *et al.* Metabolic cycling in control of glucose-stimulated insulin secretion. *Am. J.*
1013 *Physiol. - Endocrinol. Metab.* **295**, 1287–1297 (2008).

1014 31. Alfa, R. W. & Kim, S. K. Using Drosophila to discover mechanisms underlying type 2 diabetes.
1015 *Co. Biol.* **9**, 365–376 (2016).

1016 32. Na, J. *et al.* A Drosophila Model of High Sugar Diet-Induced Cardiomyopathy. *plos Genet.* **9**,
1017 e1003175 (2013).

1018 33. Randle, P. J., England, P. J. & Denton, R. M. Control of the tricarboxylate cycle and its
1019 interactions with glycolysis during acetate utilization in rat heart. *Biochem. J.* **117**, 677–695
1020 (1970).

1021 34. Gaster, M. Reduced TCA flux in diabetic myotubes: A governing influence on the diabetic
1022 phenotype? *Biochem. Biophys. Res. Commun.* **387**, 651–655 (2009).

1023 35. Palanker, L., Tennessen, J. M., Lam, G. & Thummel, C. S. Drosophila HNF4 Regulates Lipid
1024 Mobilization and β-Oxidation. *Cell Metab.* **9**, 228–239 (2009).

1025 36. Richelle, A. *et al.* Model-based assessment of mammalian cell metabolic functionalities using
1026 omics data. *Cell Reports Methods* **1**, 100040 (2021).

1027 37. Miyamoto, T. & Amrein, H. Neuronal Gluconeogenesis Regulates Systemic Glucose Homeostasis
1028 in Drosophila melanogaster Article Neuronal Gluconeogenesis Regulates Systemic Glucose
1029 Homeostasis in Drosophila melanogaster. *Curr. Biol.* **29**, 1263-1272.e5 (2019).

1030 38. Chiappino-Pepe, A. & Hatzimanikatis, V. PhenoMapping: a protocol to map cellular phenotypes
1031 to metabolic bottlenecks, identify conditional essentiality, and curate metabolic models. *STAR*
1032 *Protoc.* **2**, 100280 (2021).

1033 39. Stanway, R. R. *et al.* Genome-Scale Identification of Essential Metabolic Processes for Targeting
1034 the Plasmodium Liver Stage. *Cell* **179**, 1112-1128.e26 (2019).

1035 40. Moffett, J. R., Ross, B., Arun, P., Madhavarao, C. N. & Namboodiri, A. M. A. N-Acetylaspartate
1036 in the CNS: From neurodiagnostics to neurobiology. *Prog. Neurobiol.* **81**, 89–131 (2007).

1037 41. Enomoto, Y., Phan, N. T. A. N., Yamaguchi, M., Fukusaki, E. & Shimma, S. Mass spectrometric
1038 imaging of GABA in the Drosophila melanogaster adult head. *Anal. Sci.* **34**, 1055–1059 (2018).

1039 42. Ren, W. & Peng, Y. Betaine in inflammation : Mechanistic Aspects and Applications. *Front.*
1040 *Immunol.* **9**, 1–13 (2018).

1041 43. Hadtstein, F. & Vrolijk, M. Vitamin B-6-Induced Neuropathy : Exploring the Mechanisms of
1042 Pyridoxine Toxicity. *Adv. Nutr.* **12**, 1911–1929 (2021).

1043 44. Liu, X., Kiss, I. & Lengyel, J. A. Identification of genes controlling Malpighian tubule and other
1044 epithelial morphogenesis in Drosophila melanogaster. *Genetics* **151**, 685–695 (1999).

1045 45. Yamauchi, T. *et al.* Gut Bacterial Species Distinctively Impact Host Purine Metabolites during
1046 Aging in Drosophila. *iScience* **23**, 101477 (2020).

1047 46. Chong, J. & Xia, J. Systems biology MetaboAnalystR : an R package for flexible and reproducible
1048 analysis of metabolomics data. *Bioinformatics* **34**, 4313–4314 (2018).

1049 47. Vorontsov, I. E., Kulakovskiy, I. V & Makeev, V. J. Jaccard index based similarity measure to
1050 compare transcription factor binding site models. *algorithms Mol. Biol.* **8**, 1–11 (2013).

1051 48. Ioffe, S. Improved Consistent Sampling , Weighted Minhash and L1 Sketching. in *2010 IEEE*
1052 *international conference on data mining* 246–255 (2010). doi:10.1109/ICDM.2010.80.

1053 49. Saavedra, P. *et al.* REPTOR/CREBRF encode key regulators of muscle energy metabolism. *Nat.*
1054 *Commun.* **14**, 4943 (2023).

1055 50. Bilder, D., Ong, K., Hsi, T. C., Adiga, K. & Kim, J. Tumour–host interactions through the lens of

1056 Drosophila. *Nat. Rev. Cancer* **21**, 687–700 (2021).

1057 51. Graham, P. & Pick, L. *Drosophila as a Model for Diabetes and Diseases of Insulin Resistance*.
1058 *Current Topics in Developmental Biology* vol. 121 (Elsevier Inc., 2017).

1059 52. Blatnik, M., Thorpe, S. R. & Baynes, J. W. Succination of proteins by fumarate: Mechanism of
1060 inactivation of glyceraldehyde-3-phosphate dehydrogenase in diabetes. *Diabetes* **1126**, 272–275
1061 (2008).

1062 53. Befroy, D. E. *et al.* Impaired mitochondrial substrate oxidation in muscle of insulin-resistant
1063 offspring of type 2 diabetic patients. *Diabetes* **56**, 1376–1381 (2007).

1064 54. Oberbach, A. *et al.* Altered fiber distribution and fiber-specific glycolytic and oxidative enzyme
1065 activity in skeletal muscle of patients with type 2 diabetes. *Diabetes Care* **29**, 895–900 (2006).

1066 55. Petersen, K. F., Dufour, S., Befroy, D., Garcia, R. & Shulman, G. I. Impaired Mitochondrial
1067 Activity in the Insulin-Resistant Offspring of Patients with Type 2 Diabetes. *N. Engl. J. Med.* **350**,
1068 664–671 (2004).

1069 56. Xiao, W., Wang, R. S., Handy, D. E. & Loscalzo, J. NAD(H) and NADP(H) Redox Couples and
1070 Cellular Energy Metabolism. *Antioxidants Redox Signal.* **28**, 251–272 (2018).

1071 57. Wu, J., Jin, Z., Zheng, H. & Yan, L. J. Sources and implications of NADH/NAD+ redox
1072 imbalance in diabetes and its complications. *Diabetes, Metab. Syndr. Obes.* **9**, 145–153 (2016).

1073 58. Lowell, B. B. & Shulman, G. I. Mitochondrial dysfunction and type 2 diabetes. *Curr. Diab. Rep.*
1074 **5**, 177–183 (2005).

1075 59. Sies, H. & Jones, D. P. Reactive oxygen species (ROS) as pleiotropic physiological signalling
1076 agents. *Nat. Rev. Mol. Cell Biol.* **21**, 363–383 (2020).

1077 60. Reisz, J. A. *et al.* Oxidative modifications of glyceraldehyde 3-phosphate dehydrogenase regulate
1078 metabolic reprogramming of stored red blood cells GLUT. *Blood* **128**, e32–e42 (2016).

1079 61. Yokota, T. *et al.* Systemic oxidative stress is associated with lower aerobic capacity and impaired
1080 skeletal muscle energy metabolism in patients withmetabolic syndrome. *Diabetes Care* **36**, 1341–
1081 1346 (2013).

1082 62. Henriksen, E. J., Diamond-Stanic, M. K. & Marchionne, E. M. Oxidative stress and the etiology of
1083 insulin resistance and type 2 diabetes. *Free Radic. Biol. Med.* **51**, 993–999 (2011).

1084 63. Wieder, C. *et al.* Pathway analysis in metabolomics: Recommendations for the use of over-

representation analysis. *PLoS Comput. Biol.* **17**, 1–23 (2021).

64. Kelley, D. E., He, J., Menshikova, E. V. & Ritov, V. B. Dysfunction of mitochondria in human skeletal muscle in type 2 diabetes. *Diabetes* **51**, 2944–2950 (2002).

65. Daly, M. J. *et al.* PGC-1α-responsive genes involved in oxidative phosphorylation are coordinately downregulated in human diabetes. *Nat. Genet.* **34**, 267–273 (2003).

66. Dar, G. H. *et al.* GAPDH controls extracellular vesicle biogenesis and enhances the therapeutic potential of EV mediated siRNA delivery to the brain. *Nat. Commun.* **12**, 1–15 (2021).

67. Argilés, J. M., Campos, N., Lopez-pedrosa, J. M., Rueda, R. & Rodriguez-mañas, L. Skeletal Muscle Regulates Metabolism via Interorgan Crosstalk : Roles in Health and Disease. *J. Am. Med. Dir. Assoc.* **17**, 789–796 (2016).

68. Shestov, A. A. *et al.* Quantitative determinants of aerobic glycolysis identify flux through the enzyme GAPDH as a limiting step. *Elife* **3**, 1–18 (2014).

69. Peralta, D. *et al.* A proton relay enhances H2O2 sensitivity of GAPDH to facilitate metabolic adaptation. *Nat. Chem. Biol.* **11**, 156–163 (2015).

70. Samson, A. L. *et al.* Oxidation of an exposed methionine instigates the aggregation of glyceraldehyde-3-phosphate dehydrogenase. *J. Biol. Chem.* **289**, 26922–26936 (2014).

71. Helsley, R. N. *et al.* Tissue-Specific Fructose Metabolism in Obesity and Diabetes. *Curr. Diab. Rep.* **20**, 64 (2020).

72. Maser, D., Johnson, L. & Lee, C.-Y. Multiple Forms of Drosophila Hexokinase. *J. Biol. Chem.* **10**, 4673–4679 (1980).

73. Opdam, S. *et al.* A Systematic Evaluation of Methods for Tailoring Genome-Scale Metabolic Models. *Cell Syst.* **4**, 318-329.e6 (2017).

74. Hu, Y. *et al.* An integrative approach to ortholog prediction for disease-focused and other functional studies. *BMC Bioinformatics* **12**, 357 (2011).

75. Robinson, J. L. *et al.* An atlas of human metabolism. *Sci. Signal.* **13**, 1–12 (2020).

76. Satija, R., Farrell, J. A., Gennert, D., Schier, A. F. & Regev, A. Spatial reconstruction of single-cell gene expression data. *Nat. Biotechnol.* **33**, 495–502 (2015).

77. Li, H. *et al.* Fly Cell Atlas: A single-nucleus transcriptomic atlas of the adult fruit fly. *Science*

1113 *(80-.).* **375**, 991 (2022).

1114 78. Genomics, 10x. Should I calculate TPM , RPKM or FPKM , instead of counts for 10x Genomics
1115 data ? vol. 000002525 9–10 https://kb.10xgenomics.com/s/article/115003684783-Should-I-
1116 calculate-TPM-RPKM-or-FPKM-instead-of-counts-for-10x-Genomics-data (2024).

1117 79. Richelle, A., Chiang, A. W. T., Kuo, C.-C. & Lewis, N. E. Increasing consensus of context-
1118 specific metabolic models by integrating data-inferred cell functions. *PLoS Comput. Biol.* **15**,
1119 e1006867 (2019).

1120 80. Tennessen, J. M., Barry, W. E., Cox, J. & Thummel, C. S. Methods for studying metabolism in
1121 Drosophila. *Methods* **68**, 105–115 (2014).

1122 81. Jouandin, P. *et al.* Lysosomal cystine mobilization shapes the response of TORC1 and tissue
1123 growth to fasting. *Science (80-.).* **375**, eabc4203 (2022).

1124 82. Parkhitko, A. A. *et al.* A genetic model of methionine restriction extends Drosophila health- and
1125 lifespan. *Proc. Natl. Acad. Sci.* **118**, e2110387118 (2021).

1126 83. Matsushita, R. & Nishimura, T. Trehalose metabolism confers developmental robustness and
1127 stability in Drosophila by regulating glucose homeostasis. *Commun. Biol.* **3**, 1–12 (2020).

1128 84. Lewis, J. E. *et al.* Genome-scale modeling of NADPH-driven β-lapachone sensitization in head
1129 and neck squamous cell carcinoma. *Antioxid. Redox Signal.* **29**, 7048 (2017).

1130 85. Stein, K. T., Moon, S. J., Nguyen, A. N. & Sikes, H. D. Kinetic modeling of H2O2 dynamics in
1131 the mitochondria of HeLa cells. *PLoS Comput. Biol.* **16**, 1–21 (2020).

1132 86. Moon, S. J., Dong, W., Stephanopoulos, G. N. & Sikes, H. D. Oxidative pentose phosphate
1133 pathway and glucose anaplerosis support maintenance of mitochondrial NADPH pool under
1134 mitochondrial oxidative stress. *Bioeng. Transl. Med.* **5**, 1–18 (2020).

1135 87. Rajagopalan, P. T. R. *et al.* Interaction of dihydrofolate reductase with methotrexate: Ensemble
1136 and single-molecule kinetics. *Proc. Natl. Acad. Sci. U. S. A.* **99**, 13481–13486 (2002).

1137 88. Mdluli, K., Booth, M. P. S., Brady, R. L. & Rumsby, G. A preliminary account of the properties of
1138 recombinant human Glyoxylate reductase (GRHPR), LDHA and LDHB with glyoxylate , and
1139 their potential roles in its metabolism. *Biochim. Biophys. Acta* **1753**, 209–216 (2005).

1140 89. Ghosh, A. C., Tattikota, S. G., Liu, Y. & Comjean, A. Drosophila PDGF / VEGF signaling from
1141 muscles to hepatocyte-like cells protects against obesity. *Elife* **9**, 1–29 (2020).

1142 90. Wegener, G. Flying insects: Model systems in exercise physiology. *Experientia* **52**, 404–412
1143 (1996).

1144 91. Goody, M. F. & Henry, C. A. A need for NAD+ in muscle development, homeostasis, and aging.
1145 *Skelet. Muscle* **8**, 1–14 (2018).

1146 92. Augustin, H. & Partridge, L. Invertebrate models of age-related muscle degeneration. *Biochim.*
1147 *Biophys. Acta - Gen. Subj.* **1790**, 1084–1094 (2009).

1148 93. Hagen, J. L. *et al.* Skeletal muscle aging in F344BN F1-hybrid rats: I. Mitochondrial dysfunction
1149 contributes to the age-associated reduction in VO2max. *Journals Gerontol. - Ser. A Biol. Sci. Med.*
1150 *Sci.* **59**, 1099–1110 (2004).

1151 94. Coquin, L., Feala, J. D., McCulloch, A. D. & Paternostro, G. Metabolomic and flux-balance
1152 analysis of age-related decline of hypoxia tolerance in Drosophila muscle tissue. *Mol. Syst. Biol.* **4**,
1153 1–13 (2008).

1154 95. Orth, J. D., Thiele, I. & Palsson, B. Ø. What is flux balance analysis ? *Nat. Publ. Gr.* **28**, 245–248
1155 (2010).

1156 96. Schiaffino, S., Reggiani, C., Akimoto, T. & Blaauw, B. Molecular Mechanisms of Skeletal Muscle
1157 Hypertrophy. *J. Neuromuscul. Dis.* **8**, 169–183 (2021).

1158 97. Meinild Lundby, A. K. *et al.* Exercise training increases skeletal muscle mitochondrial volume
1159 density by enlargement of existing mitochondria and not de novo biogenesis. *Acta Physiol.* **222**, 1–
1160 14 (2018).

1161 98. Gudmundsson, S. & Thiele, I. Computationally efficient flux variability analysis. *BMC*
1162 *Bioinformatics* **11**, 2–4 (2010).

1163 99. Megchelenbrink, W., Huynen, M. & Marchiori, E. optGpSampler: An improved tool for uniformly
1164 sampling the solution-space of genome-scale metabolic networks. *PLoS One* **9**, e86587 (2014).

1165 100. Lewis, N. E. *et al.* Omic data from evolved E . coli are consistent with computed optimal growth
1166 from genome-scale models. *Mol. Syst. Biol.* **6**, 1–13 (2010).

1167 101. Bordel, S., Agren, R. & Nielsen, J. Sampling the Solution Space in Genome-Scale Metabolic
1168 Networks Reveals Transcriptional Regulation in Key Enzymes. *PLoS Comput. Biol.* **6**, 1–13
1169 (2010).

1170 102. Heinrich, R. & Rapoport, T. A. A Linear Steady-State Treatment of Enzymatic Chains: General

1171 Properties, Control and Effector Strength. *Eur. J. Biochem.* **42**, 89–95 (1974).

1172 103. Fell, D. A. Increasing the flux in metabolic pathways: A metabolic control analysis perspective.
1173 *Biotechnol. Bioeng.* **58**, 121–124 (1998).

1174 104. Yue, H. *et al.* Insights into the behaviour of systems biology models from dynamic sensitivity and
1175 identifiability analysis: A case study of an NF-κB signalling pathway. *Mol. Biosyst.* **2**, 640–649
1176 (2006).

1177 105. Beenakkers, A. M., Van Der Horst, D. J. & Marrewijk, W. J. A. Inset flight muscle metabolism.
1178 *Insect Biochem* **14**, 243–260 (1984).

1179 106. Feala, J. D., Coquin, L., McCulloch, A. D. & Paternostro, G. Flexibility in energy metabolism
1180 supports hypoxia tolerance in Drosophila flight muscle: Metabolomic and computational systems
1181 analysis. *Mol. Syst. Biol.* **3**, 1–7 (2007).

1182 107. Volkenhoff, A. *et al.* Glial glycolysis is essential for neuronal survival in drosophila. *Cell Metab.*
1183 **22**, 437–447 (2015).

1184 108. Su, X., Lu, W. & Rabinowitz, J. D. Metabolite Spectral Accuracy on Orbitraps. *Anal. Chem.* **89**,
1185 5940–5948 (2017).

1186 109. Mirdita, M. *et al.* ColabFold: making protein folding accessible to all. *Nat. Methods* **19**, 679–682
1187 (2022).

1188 110. Jumper, J. *et al.* Highly accurate protein structure prediction with AlphaFold. *Nature* **596**, 583–
1189 589 (2021).

1190 111. Ah-ram, K. *et al.* A Structure-Guided Kinase–Transcription Factor Interactome Atlas Reveals
1191 Docking Landscapes of the Kinome. *bioRxiv* 681672 (2025) doi:10.1101/2025.10.10.681672.

1192 112. Meng, E. C. *et al.* UCSF ChimeraX: Tools for structure building and analysis. *Protein Sci.* **32**, 1–
1193 13 (2023).

1194 113. Parkhitko, A. A. *et al.* Tissue-specific down-regulation of S-adenosyl-homocysteine via
1195 suppression of dAhcyL1 / dAhcyL2 extends health span and life span in Drosophila. *Genes Dev.*
1196 **30**, 1409–1422 (2016).

1197 114. Cracan, V., Titov, D. V., Shen, H., Grabarek, Z. & Mootha, V. K. A genetically encoded tool for
1198 manipulation of NADP+/NADPH in living cells. *Nat. Chem. Biol.* **13**, 1088–1095 (2017).

1199 115. Moon, S. J. Modeling tissue-specific Drosophila metabolism identifies high sugar diet-induced

metabolic dysregulation in muscle at reaction and pathway levels. at https://doi.org/10.5281/zenodo.17684286 (2025).

Acknowledgements

We thank members of the Perrimon laboratory for useful discussions and experimental advice, including Dr. Stephanie Mohr for feedback on the manuscript. We also thank to the Research Computing Group at Harvard Medical School for access to the O2 High Performance Compute Cluster. We additionally thank Dr. Anush Chiappino-Pepe and Dr. Steven Marygold for valuable feedback on genome-scale metabolic modeling work. We also thank Dr. Jason Tennessen for valuable feedback on fly metabolism. We also thank Dr. Travis Nemkov for valuable feedback on metabolomics analysis. We also thank Dr. Safak Yilmaz and Dr. Marian Walhout for valuable feedback on genome-scale metabolic models. AK was supported by Postdoctoral Fellowship Program (Nurturing Next-generation Researchers) through the National Research Foundation of Korea (NRF) funded by the Ministry of Education (2021R1A6A3A14039622). The mass spectrometry work was partially funded by NIH grants 5P01CA120964 (J.M.A.) and 5P30CA006516 (J.M.A.). This research was supported by NIH/NIDDK 1R01DK136945, NIH NIAMS R01 AR057352, Cancer 509 Research UK (CGCATF-2021/100022) and the National Cancer Institute (1OT2 CA278685-01). NP is an investigator of Howard Hughes Medical Institute. This article is subject to HHMI's Open Access to Publications policy. HHMI lab heads have previously granted a nonexclusive CC BY 4.0 license to the public and a sublicensable license to HHMI in their research articles. Pursuant to those licenses, the author-accepted manuscript of this article can be made freely available under a CC BY 4.0 license immediately upon publication.

Author Contributions

S.J.M. and N.P. designed the study. Y.H. performed bioinformatics analyses related to the Fly Cell Atlas datasets. S.J.M. performed the computational analyses and follow-up experiments. S.J.M. and J.M.A. performed metabolomics and subsequent analyses. S.J.M., M.D., and A.D. performed redox proteomics and subsequent analyses. A.R.K. performed the AlphaFold structural analysis. N.P. supervised the work. S.J.M. and N.P. wrote the manuscript. S.J.M., Y.H., M.D., A.R.K., J.M.A., A.D., and N.P. reviewed and edited the manuscript.

Competing interests

The authors declare no competing interests.

1232 # Figure legends

1233 **Fig. 1: Reconstruction of 32 tissue-specific genome-scale metabolic models (GEMs) in *Drosophila***
1234 ***melanogaster***

1235 **a** Pipeline for reconstruction of tissue-specific GEMs in *Drosophila*. Elements created in BioRender.
1236 Moon, S. (2025) https://BioRender.com/1nasxv2. **b** t-SNE plot comparing the metabolic network
1237 structures of 32 tissue-specific GEMs using Hamming similarity. Each point represents one tissue-
1238 specific GEM, with marker shapes and colors indicating major tissue groups (muscle: red circles; fat
1239 body/oenocyte: purple squares; gut: orange diamonds; glia: green downward triangles; neurons: dark red
1240 upward triangles; others: gray stars). Abbreviations: PNS is peripheral nervous system; VNS is ventral
1241 nervous system; LMM neuron is leg muscle motor neuron; RN glial cell is reticular neuropil associated
1242 glial cell; CNSS glial cell is central nervous system surface associated glial cell. **c** Jaccard index analysis
1243 comparing overlap between clusters defined by tissue-GEM and those based on gene expression. **d**
1244 Number of reactions per subsystem across GEMs, highlighting the top 10 subsystems by reaction count.
1245 **e** Fraction of extracellular transport reactions relative to all transport reactions, with major tissue groups
1246 highlighted. Dashed lines indicate mean values. Correlation was assessed using a two-sided Pearson
1247 correlation test ($r = 0.93$, $p = 5e\text{-}15$). **f** Heatmap of differential subsystem coverage across tissues, with
1248 bright yellow indicating higher coverage and dark blue lower coverage. Subsystems with ≥15 reactions
1249 and >50% deviation from mean coverage are shown. Source data are provided as a Source Data file.

1250 **Fig. 2. Validation of tissue-specific GEMs through regional metabolomics and pathway analysis**

1251 **a** Schematics showing the metabolomics analysis performed on four *Drosophila* regions, followed by
1252 KEGG over-representation analysis. Elements created in BioRender. Moon, S. (2025)
1253 https://BioRender.com/1nasxv2. **b** Principal component analysis (PCA) of metabolite profiles across
1254 regions (n = 4). **c** Heatmap showing the metabolite profiles across thorax, head, abdomen, and gut. **d**
1255 Bubble plot showing enriched metabolites in each region compared to others. One-way ANOVA followed
1256 by Benjamini-Hochberg (BH) correction was used for multiple comparisons. **e** Over-representation
1257 analysis of enriched metabolite sets across regions, using a one-sided hypergeometric test, followed by
1258 BH correction for multiple comparisons. **f** Heatmap of weighted Jaccard index values showing pathway
1259 overlaps between metabolomics-derived and GEM-predicted pathways. **g-h** Boxplots showing weighted
1260 Jaccard index distributions between metabolomics-derived pathways and either (**g**) Muscle-GEM or (**h)**
1261 Fat body-GEM. Center line is median; box limits are first and third quartiles; whiskers are 1.5 ×
1262 interquartile range; red points are mean; gray points present individual bootstrap samples (n = 10,000),
1263 shown in full including those outside the whiskers. Statistical significance is based on comparisons
1264 against the reference region (g: thorax; h: abdomen) using one-way ANOVA followed by Bonferroni-
1265 corrected pairwise tests; *** $p < 0.001$. Overlapping pathways between GEM-predicted and region-
1266 specific enriched pathways are shown to the right. Source data are provided as a Source Data file.

1267 **Fig. 3. Constraint-based flux analyses predict perturbations in NAD(H)-dependent reactions in**
1268 **muscle under high sugar diet**

1269 **a** Schematics of constraint-based semi-quantitative flux analyses for muscle under HSD. Constraints were
1270 applied to reflect metabolic alterations observed in muscle under HSD, recapitulating features of type 2
1271 diabetes in *Drosophila*. FBA, pFBA, and FVA_sampling analyses were performed to estimate differential
1272 reaction fluxes, identifying commonly perturbed reactions across the methods. Elements created in
1273 BioRender. Moon, S. (2025) https://BioRender.com/1nasxv2. **b** Networks showing the top three most
1274 commonly perturbed subsystems, reactions, and genes from the decreased (blue) and increased (red)
1275 reaction sets identified across flux analyses. Node size indicates the number of reactions associated with
1276 each subsystem, and edge width represents the number of linked genes. **c** Differential fluxes of NAD(H)-
1277 dependent reactions between HSD and NSD from FVA_sampling analysis. Dot size reflects absolute
1278 differential flux and color scale indicates adjusted p-values from a two-sample Z-test. X-axis shows $\log_2$
1279 fold change, with threshold of ± 0.5. Reactions consistently decreased or increased across different flux
1280 analyses are labeled in blue or red, respectively. **d** Schematic of the pFBA evaluating maximum NADH
1281 production capacity under HSD and NSD conditions. An artificial NADH oxidation reaction (NADH →
1282 NAD^+) was introduced as a total NADH demand across cytosolic, mitochondrial, and peroxisomal
1283 compartments. **e** Maximal NADH demand flux estimated by pFBA between NSD and HSD conditions. **f**
1284 NAD^+/NADH ratio in w^{1118} male flies fed NSD or HSD for five days. Data are shown as mean ± SD from
1285 biological replicates (n = 5). Statistical significance was assessed using a two-tailed unpaired t-test; ** $p <$
1286 0.01. **g** Schematic of the sensitivity analysis workflow for glycolysis. Individual glycolytic fluxes were
1287 perturbed, followed by FVA-sampling to quantify changes in total pyruvate consumption flux, which
1288 served as a proxy for glycolytic output. Normalized sensitivity coefficients were calculated to assess each
1289 reaction's influence on the pathway output flux. **h** Bar plot showing normalized sensitivity coefficients
1290 (S_i) of glycolytic reactions under different perturbation magnitudes (5 – 50%). The bar plot on the right
1291 shows the average absolute sensitivity ($|S_i|$), highlighting reactions with the greatest overall influence
1292 under these simulations. Source data are provided as a Source Data file.
1293

Fig. 4. Model-predicted decreases in glycolytic flux, including GAPDH, validated through ^{13}C-glucose tracing

a Experimental design for ^{13}C-glucose isotope tracing experiments in *Drosophila* thoracic muscle under high sugar diet (HSD) conditions. Elements created in BioRender. Moon, S. (2025) https://BioRender.com/1nasxv2. **b** Isotopic labeling patterns generated by [U-$^{13}C_6$]glucose in glycolysis and TCA cycle. Red circles represent ^{13}C-labeled carbons. **c-d** Fractional labeling of mass isotopomers of (**c**) glycolytic or (**d**) TCA cycle intermediates, shown as both fractional labeling (left) and values normalized to M+6 glucose and scaled relative to normal sugar diet (NSD) (right). Bars represent mean ± SEM, and individual points indicate biological replicates (n = 6). M+x denotes a mass isotopomer containing x ^{13}C atoms. Statistical significance was assessed using two-tailed unpaired t-tests comparing NSD and HSD for each metabolite; * $p < 0.05$, ** $p < 0.01$, *** $p < 0.001$. **e** Correlation between model-predicted relative flux changes (HSD-muscle-GEM/Unconstrained) and fractional labeling of glycolytic intermediates (HSD/NSD). Relative flux of each reaction was mapped to the normalized fractional labeling of its corresponding product metabolite. Fractional labeling values (y-axis) are shown as mean ± SEM from biologically independent replicates (n = 6), and model-predicted flux values (x-axis) are shown as mean ± SEM from flux sampling simulations (n = 10,000). The dashed red line represents a linear regression fit, with the shaded region indicating the 95% confidence interval. Correlation was assessed using a two-sided Pearson correlation test ($r = 0.813$, $p = 0.0263$). Source data are provided as a Source Data file.

1313 **Fig. 5. Model-predicted decreases in glycolytic flux correlate with increased redox modification of**
1314 **glycolytic enzymes**

1315 **a** Experimental design for switch-tag redox proteomics in *Drosophila* thoracic muscle under HSD
1316 conditions. Elements created in BioRender. Moon, S. (2025) https://BioRender.com/1nasxv2. **b** PCA plot
1317 showing variance in oxidized peptides between HSD and NSD conditions. **c** Volcano plot displaying
1318 differentially oxidized peptides in thoracic muscle between HSD and NSD conditions. The intensities
1319 were normalized within each protein across samples. **d** Dot plot showing KEGG pathway enrichment
1320 (*Drosophila*) based on significantly oxidized peptides. **e** Heatmap showing the significantly oxidized
1321 peptides in glycolysis between NSD and HSD conditions. **f** Correlation between model-predicted relative
1322 flux changes (HSD-muscle-GEM/Unconstrained) and relative oxidation state changes of glycolytic
1323 enzyme peptides (HSD/NSD). Relative oxidation state was calculated as the average oxidation level of
1324 peptides from each enzyme in HSD, normalized to NSD. Relative oxidation state values (y-axis) are
1325 shown as mean ± SEM from biologically independent replicates (n = 6), and model-predicted flux values
1326 (x-axis) are shown as mean ± SEM from flux sampling simulations (n = 10,000). The dashed red line
1327 represents a linear regression fit, with the shaded region indicating the 95% confidence interval.
1328 Correlation was evaluated using a two-sided Pearson correlation test ($r = -0.771$, $p = 0.0251$). **g** Boxplot
1329 showing normalized intensity of significantly oxidized GAPDH peptide. Center line is median; box limits
1330 are first and third quartiles; whiskers are 1.5 × interquartile range; points represent biologically
1331 independent replicates (n = 6). Statistical significance was assessed using a two-tailed unpaired t-test and
1332 the p-value is shown above the plot. **h** Climbing ability of male Mhc^{ts}>attp40 (control), or *GAPDH1*-
1333 RNAi flies, measured at day 5 and 10 after fed with HSD. Bar represent mean ± SD, and individual points
1334 indicate biological replicates (n = 3). Statistical significance was assessed using two-tailed unpaired t-
1335 tests comparing control vs. *GAPDH1*-RNAi within each time point; ns = not significant, * $p < 0.05$.
1336 Source data are provided as a Source Data file.

1337 **Fig. 6. Pathway-level flux analysis reveals dysregulated fructose metabolism**

1338 **a** Schematic of the pathway-level flux analysis pipeline. FVA-sampling and pFBA were used to estimate
1339 pathway fluxes under HSD and NSD conditions, followed by calculation of Z-scores and $\log_2$ fold
1340 changes to identify perturbed pathways. Elements created in BioRender. Moon, S. (2025)
1341 https://BioRender.com/1nasxv2. **b** Pathway-level flux differences between HSD and NSD conditions.
1342 Each dot represents a pathway, with its size indicating absolute pathway flux difference and color
1343 representing adjusted *p*-value. The x-axis shows the $\log_2$ fold change in pathway flux. Pathways
1344 highlighted in blue or red show commonly decreased or increased fluxes across both FVA-sampling and
1345 pFBA. **c** Schematic representing the targeted metabolite profiling of thoracic muscles from w^{1118} male
1346 flies fed either HSD or NSD. Elements created in BioRender. Moon, S. (2025)
1347 https://BioRender.com/1nasxv2. **d** PCA of thoracic metabolite profiles under HSD and NSD (n = 4). **e**
1348 Volcano plot showing significantly altered metabolites in thoracic muscles in response to HSD. **f**
1349 Integrated schematic of fructose and sucrose metabolism (KEGG: dme00051 and dme00050),
1350 highlighting key metabolites, enzymes, and reactions. Box plots (black outline) display normalized
1351 metabolite levels under NSD and HSD. Center line is median; box limits are first and third quartiles;
1352 whiskers are 1.5 × interquartile range; points represent biologically independent replicates (n = 4).
1353 Statistical significance was assessed using a two-tailed unpaired t-test and the p-value is shown above the
1354 plot. Heatmaps (green outline) indicate significantly altered redox modifications for select enzymes ($p <$
1355 0.05). Histograms (purple outline) show model-predicted flux distributions from flux sampling analysis (n
1356 = 10,000). Black arrows indicate reactions not detected (ND) in the muscle-GEM. Colored metabolite
1357 names and arrows represent $\log_2$ fold changes (HSD/NSD) for both fluxes and metabolite levels, as
1358 shown in the color scale. Source data are provided as a Source Data file.

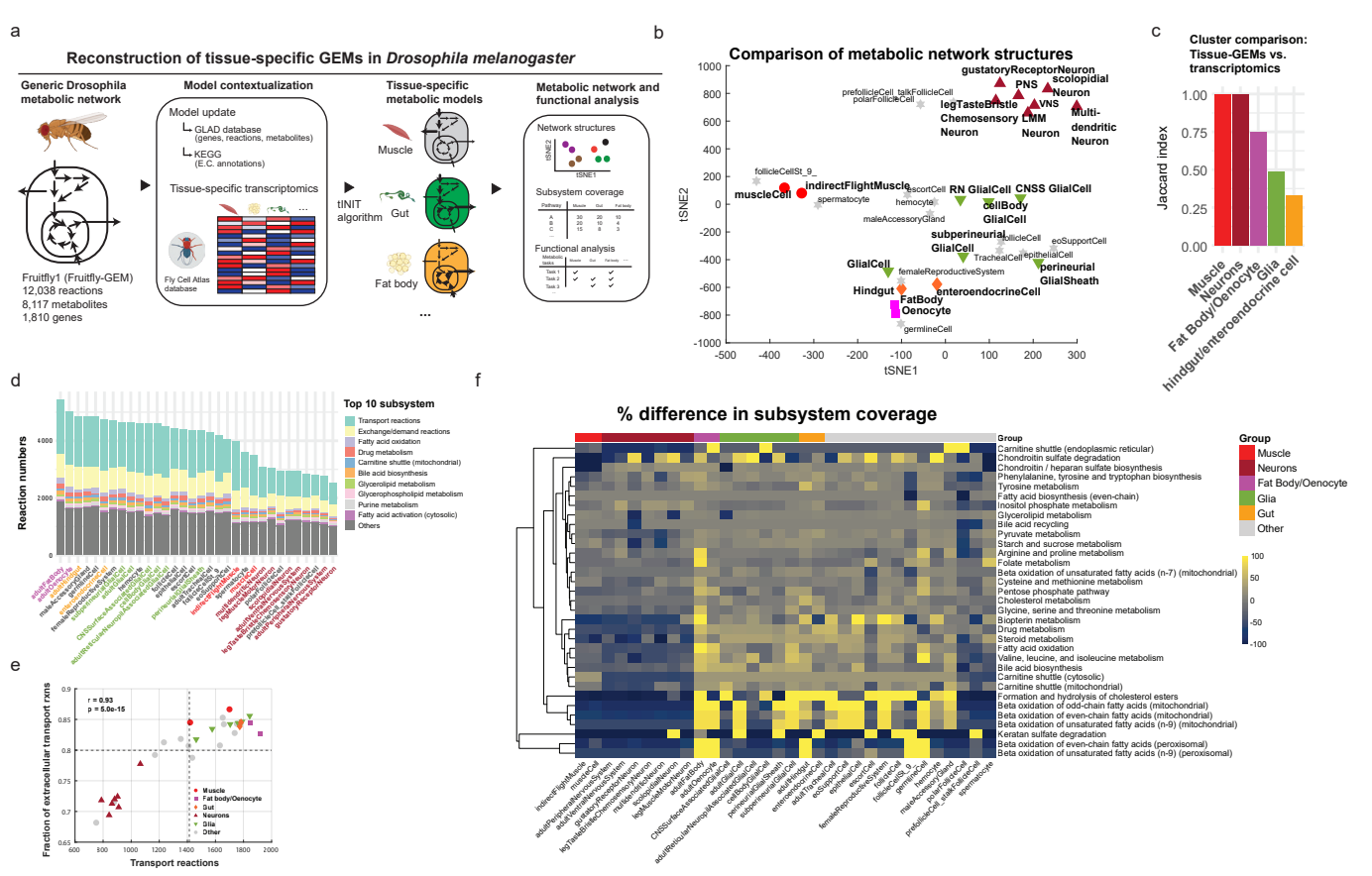
a
Reconstruction of tissue-specific GEMs in Drosophila melanogaster
Generic Drosophila metabolic network
Fruitfly1 (Fruitfly-GEM)
12,038 reactions
8,117 metabolites
1,810 genes
Model contextualization
Model update
GLAD database (genes, reactions, metabolites)
KEGG (E.C. annotations)
Tissue-specific transcriptomics
Fly Cell Atlas database
tINIT algorithm
Tissue-specific metabolic models
Muscle
Gut
Fat body
Metabolic network and functional analysis
Network structures
Subsystem coverage
Functional analysis
b
Comparison of metabolic network structures
tSNE1
tSNE2
muscleCell
indirectFlightMuscle
RN GlialCell
CNSS GlialCell
cellBody GlialCell
subperineurial GlialCell
perineurial GlialSheath
Hindgut
enteroendocrineCell
FatBody Oenocyte
GlialCell
gustatoryReceptorNeuron
scolopidial Neuron
PNS
legTasteHustle Chemosensory Neuron
VNS
LMM Neuron
Multi-dendritic Neuron
c
Cluster comparison: Tissue-GEMs vs. transcriptomics
Jaccard index
Muscle
Neurons
Fat Body/Oenocyte
Glia
hindgut/enteroendocrine cell
d
Reaction numbers
Top 10 subsystem
Transport reactions
Exchange/demand reactions
Fatty acid oxidation
Drug metabolism
Carnitine shuttle (mitochondrial)
Bile acid biosynthesis
Glycerolipid metabolism
Glycerophospholipid metabolism
Purine metabolism
Fatty acid activation (cytosolic)
Others
e
r = 0.93
p = 5.0e-15
Fraction of extracellular transport rxns
Transport reactions
Muscle
Fat body/Oenocyte
Gut
Neurons
Glia
Other
f
% difference in subsystem coverage
Group
Muscle
Neurons
Fat Body/Oenocyte
Glia
Gut
Other
Carnitine shuttle (endoplasmic reticular)
Chondroitin sulfate degradation
Chondroitin / heparan sulfate biosynthesis
Phenylalanine, tyrosine and tryptophan biosynthesis
Tyrosine metabolism
Fatty acid biosynthesis (even-chain)
Inositol phosphate metabolism
Glycerolipid metabolism
Bile acid recycling
Pyruvate metabolism
Starch and sucrose metabolism
Arginine and proline metabolism
Folate metabolism
Beta oxidation of unsaturated fatty acids (n-7) (mitochondrial)
Cysteine and methionine metabolism
Pentose phosphate pathway
Cholesterol metabolism
Glycine, serine and threonine metabolism
Biopterin metabolism
Drug metabolism
Steroid metabolism
Fatty acid oxidation
Valine, leucine, and isoleucine metabolism
Bile acid biosynthesis
Carnitine shuttle (cytosolic)
Carnitine shuttle (mitochondrial)
Formation and hydrolysis of cholesterol esters
Beta oxidation of odd-chain fatty acids (mitochondrial)
Beta oxidation of even-chain fatty acids (mitochondrial)
Beta oxidation of unsaturated fatty acids (n-9) (mitochondrial)
Keratan sulfate degradation
Beta oxidation of even-chain fatty acids (peroxisomal)
Beta oxidation of unsaturated fatty acids (n-9) (peroxisomal)

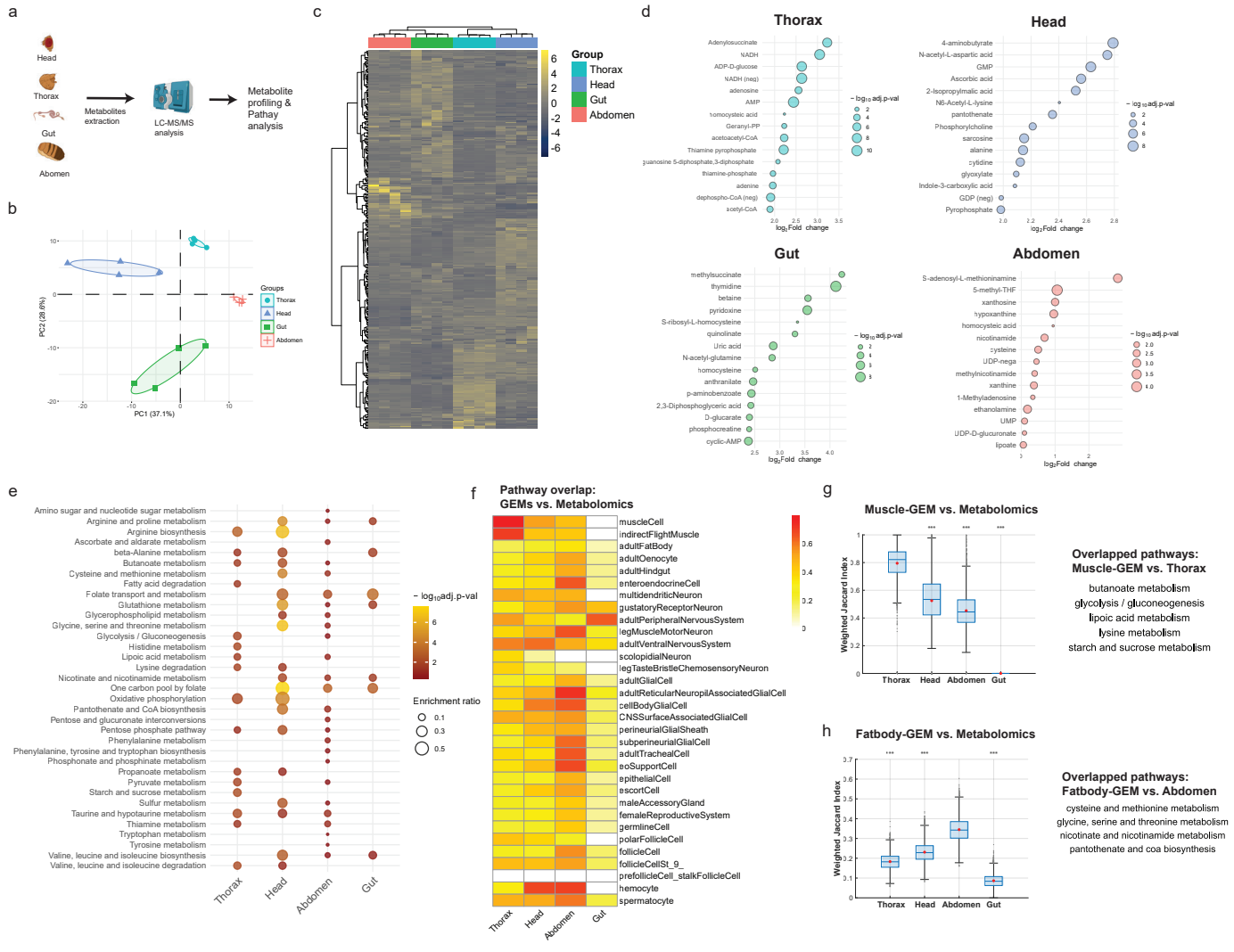
a
Head
Thorax
Gut
Abomen
Metabolites extraction
LC-MS/MS analysis
Metabolite profiling & Pathay analysis
b
PC2 (28.8%)
PC1 (37.1%)
Groups
Thorax
Head
Gut
Abdomen
c
Group
Thorax
Head
Gut
Abdomen
d
Thorax
Adenylosuccinate
NADH
ADP-D-glucose
NADH (neg)
adenosine
AMP
homocysteic acid
Geranyl-PP
acetoacetyl-CoA
Thiamine pyrophosphate
guanosine 5-diphosphate,3-diphosphate
thiamine-phosphate
adenine
dephospho-CoA (neg)
acetyl-CoA
log2Fold change
Head
4-aminobutyrate
N-acetyl-L-aspartic acid
GMP
Ascorbic acid
2-Isopropylmalic acid
N6-Acetyl-L-lysine
pantothenate
Phosphorylcholine
sarcosine
alanine
cytidine
glycolate
Indole-3-carboxylic acid
GDP (neg)
Pyrophosphate
log2Fold change
Gut
methylsuccinate
thymidine
betaine
pyridoxine
S-ribosyl-L-homocysteine
quinolinate
Uric acid
N-acetyl-glutamine
homocysteine
anthranilate
p-aminobenzoate
2,3-Diphosphoglyceric acid
D-glucarate
phosphocreatine
cyclic-AMP
log2Fold change
Abdomen
S-adenosyl-L-methioninamine
5-methyl-THF
xanthosine
hypoxanthine
homocysteic acid
nicotinamide
cysteine
UDP-nega
methylnicotinamide
xanthine
1-Methyladenosine
ethanolamine
UMP
UDP-D-glucuronate
lipoate
log2Fold change
e
Amino sugar and nucleotide sugar metabolism
Arginine and proline metabolism
Arginine biosynthesis
Ascorbate and aldarate metabolism
beta-Alanine metabolism
Butanoate metabolism
Cysteine and methionine metabolism
Fatty acid degradation
Folate transport and metabolism
Glutathione metabolism
Glycerophospholipid metabolism
Glycine, serine and threonine metabolism
Glycolysis / Gluconeogenesis
Histidine metabolism
Lipoic acid metabolism
Lysine degradation
Nicotinate and nicotinamide metabolism
One carbon pool by folate
Oxidative phosphorylation
Pantothenate and CoA biosynthesis
Pentose and glucuronate interconversions
Pentose phosphate pathway
Phenylalanine metabolism
Phenylalanine, tyrosine and tryptophan biosynthesis
Phosphonate and phosphinate metabolism
Propanoate metabolism
Pyruvate metabolism
Starch and sucrose metabolism
Sulfur metabolism
Taurine and hypotaurine metabolism
Thiamine metabolism
Tryptophan metabolism
Tyrosine metabolism
Valine, leucine and isoleucine biosynthesis
Valine, leucine and isoleucine degradation
Thorax
Head
Abdomen
Gut
Enrichment ratio
f
Pathway overlap:
GEMs vs. Metabolomics
muscleCell
indirectFlightMuscle
adultFatBody
adultOenocyte
adultHindgut
enteroendocrineCell
multidendriticNeuron
gustatoryReceptorNeuron
adultPeripheralNervousSystem
legMuscleMotorNeuron
adultVentralNervousSystem
scolopidialNeuron
legTasteBristleChemosensoryNeuron
adultGlialCell
adultReticularNeuropilAssociatedGlialCell
cellBodyGlialCell
CNSSurfaceAssociatedGlialCell
perineurialGlialSheath
subperineurialGlialCell
adultTrachealCell
eoSupportCell
epithelialCell
escortCell
maleAccessoryGland
femaleReproductiveSystem
germlineCell
polarFollicleCell
follicleCell
follicleCellSt_9_
prefollicleCell_stalkFollicleCell
hemocyte
spermatocyte
Thorax
Head
Abdomen
Gut
g
Muscle-GEM vs. Metabolomics
Weighted Jaccard Index
Thorax
Head
Abdomen
Gut
Overlapped pathways:
Muscle-GEM vs. Thorax
butanoate metabolism
glycolysis / gluconeogenesis
lipoic acid metabolism
lysine metabolism
starch and sucrose metabolism
h
Fatbody-GEM vs. Metabolomics
Weighted Jaccard Index
Thorax
Head
Abdomen
Gut
Overlapped pathways:
Fatbody-GEM vs. Abdomen
cysteine and methionine metabolism
glycine, serine and threonine metabolism
nicotinate and nicotinamide metabolism
pantothenate and coa biosynthesis

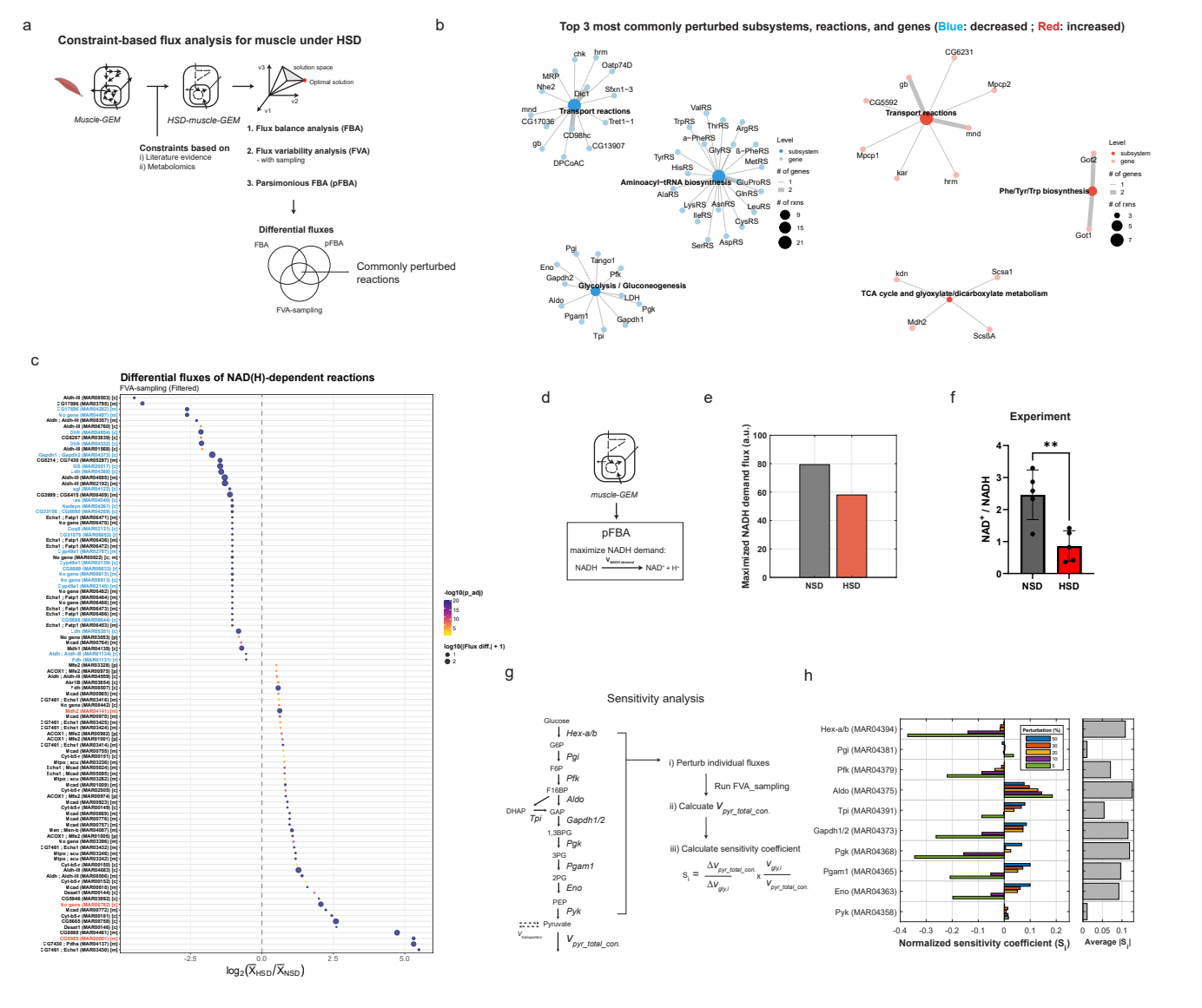
a
Constraint-based flux analysis for muscle under HSD
Muscle-GEM
HSD-muscle-GEM
solution space
Optimal solution
v3
v2
v1
Constraints based on
i) Literature evidence
ii) Metabolomics
1. Flux balance analysis (FBA)
2. Flux variability analysis (FVA)
- with sampling
3. Parsimonious FBA (pFBA)
Differential fluxes
FBA
pFBA
FVA-sampling
Commonly perturbed reactions
b
Top 3 most commonly perturbed subsystems, reactions, and genes (Blue: decreased ; Red: increased)
Transport reactions
Aminoacyl−tRNA biosynthesis
Glycolysis / Gluconeogenesis
Phe/Tyr/Trp biosynthesis
TCA cycle and glyoxylate/dicarboxylate metabolism
Level
subsystem
gene
# of genes
# of rxns
c
Differential fluxes of NAD(H)-dependent reactions
FVA-sampling (Filtered)
-log10(p_adj)
log10(|Flux diff.| + 1)
d
muscle-GEM
pFBA
maximize NADH demand:
NADH → NAD⁺ + H⁺
Maximized NADH demand flux (a.u.)
NSD
HSD
e
Experiment
NAD⁺ / NADH
f
Sensitivity analysis
Glucose
Hex-a/b
G6P
Pgi
F6P
Pfk
F16BP
Aldo
DHAP
Tpi
GAP
Gapdh1/2
1,3BPG
Pgk
3PG
Pgam1
2PG
Eno
PEP
Pyk
Pyruvate
i) Perturb individual fluxes
Run FVA_sampling
ii) Calcuate
iii) Calculate sensitivity coefficient
g
Perturbation (%)
Normalized sensitivity coefficient
Average
h

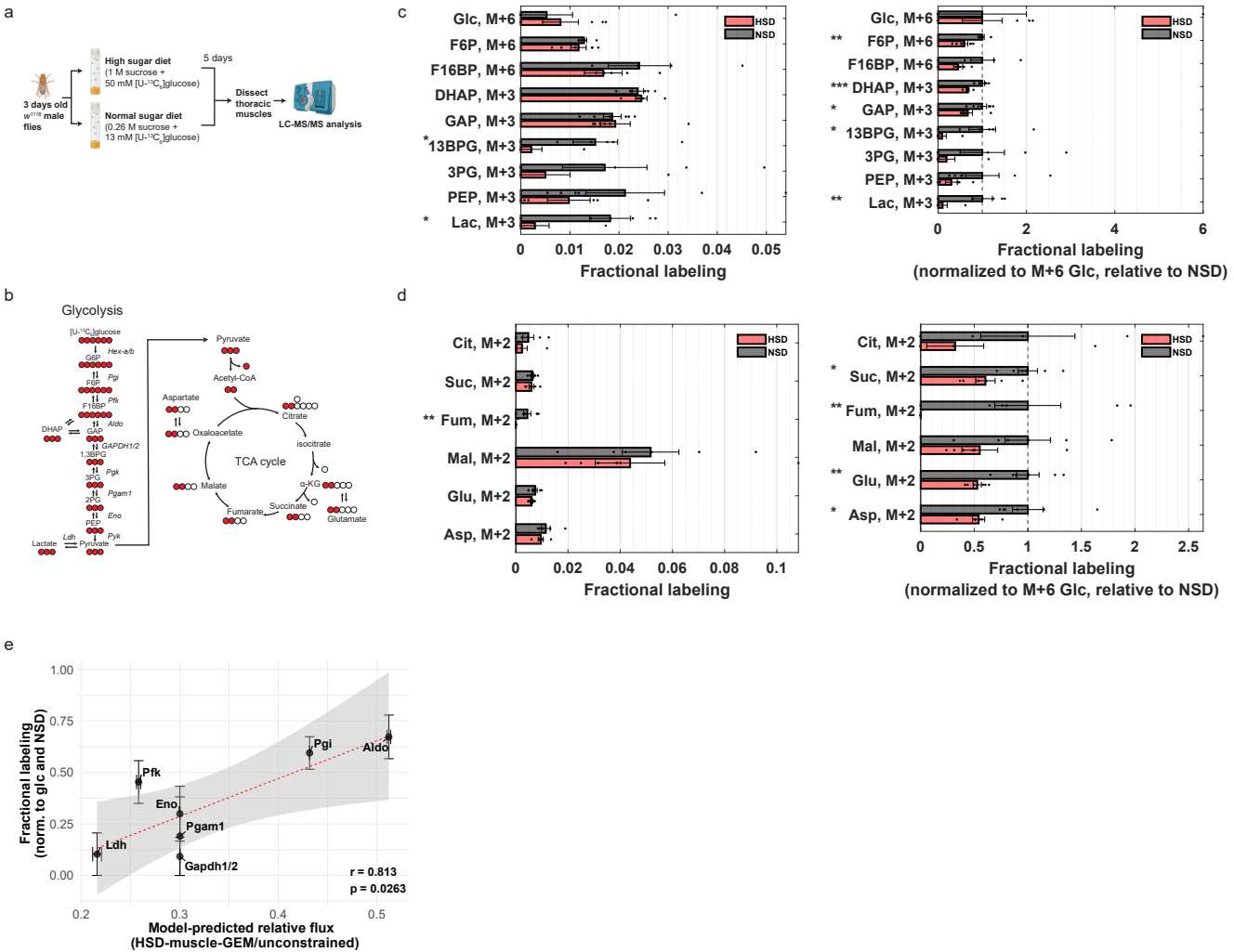
a
3 days old w1118 male flies
High sugar diet
(1 M sucrose + 50 mM [U-13C6]glucose)
Normal sugar diet
(0.26 M sucrose + 13 mM [U-13C6]glucose)
5 days
Dissect thoracic muscles
LC-MS/MS analysis
b
Glycolysis
[U-13C6]glucose
Hex-a/b
G6P
Pgi
F6P
Pfk
F16BP
Aldo
DHAP
GAP
GAPDH1/2
1,3BPG
Pgk
3PG
Pgam1
2PG
Eno
PEP
Pyk
Ldh
Lactate
Pyruvate
Acetyl-CoA
Aspartate
Citrate
Oxaloacetate
isocitrate
TCA cycle
Malate
α-KG
Succinate
Fumarate
Glutamate
c
HSD
NSD
Glc, M+6
F6P, M+6
F16BP, M+6
DHAP, M+3
GAP, M+3
*13BPG, M+3
3PG, M+3
PEP, M+3
* Lac, M+3
0 0.01 0.02 0.03 0.04 0.05
Fractional labeling
** F6P, M+6
*** DHAP, M+3
* GAP, M+3
* 13BPG, M+3
** Lac, M+3
0 2 4 6
Fractional labeling
(normalized to M+6 Glc, relative to NSD)
d
Cit, M+2
Suc, M+2
** Fum, M+2
Mal, M+2
Glu, M+2
Asp, M+2
0 0.02 0.04 0.06 0.08 0.1
Fractional labeling
* Suc, M+2
** Fum, M+2
** Glu, M+2
* Asp, M+2
0 0.5 1 1.5 2 2.5
Fractional labeling
(normalized to M+6 Glc, relative to NSD)
e
Fractional labeling
(norm. to glc and NSD)
1.00
0.75
0.50
0.25
0.00
Pgi
Aldo
Pfk
Eno
Pgam1
Ldh
Gapdh1/2
r = 0.813
p = 0.0263
0.2 0.3 0.4 0.5
Model-predicted relative flux
(HSD-muscle-GEM/unconstrained)

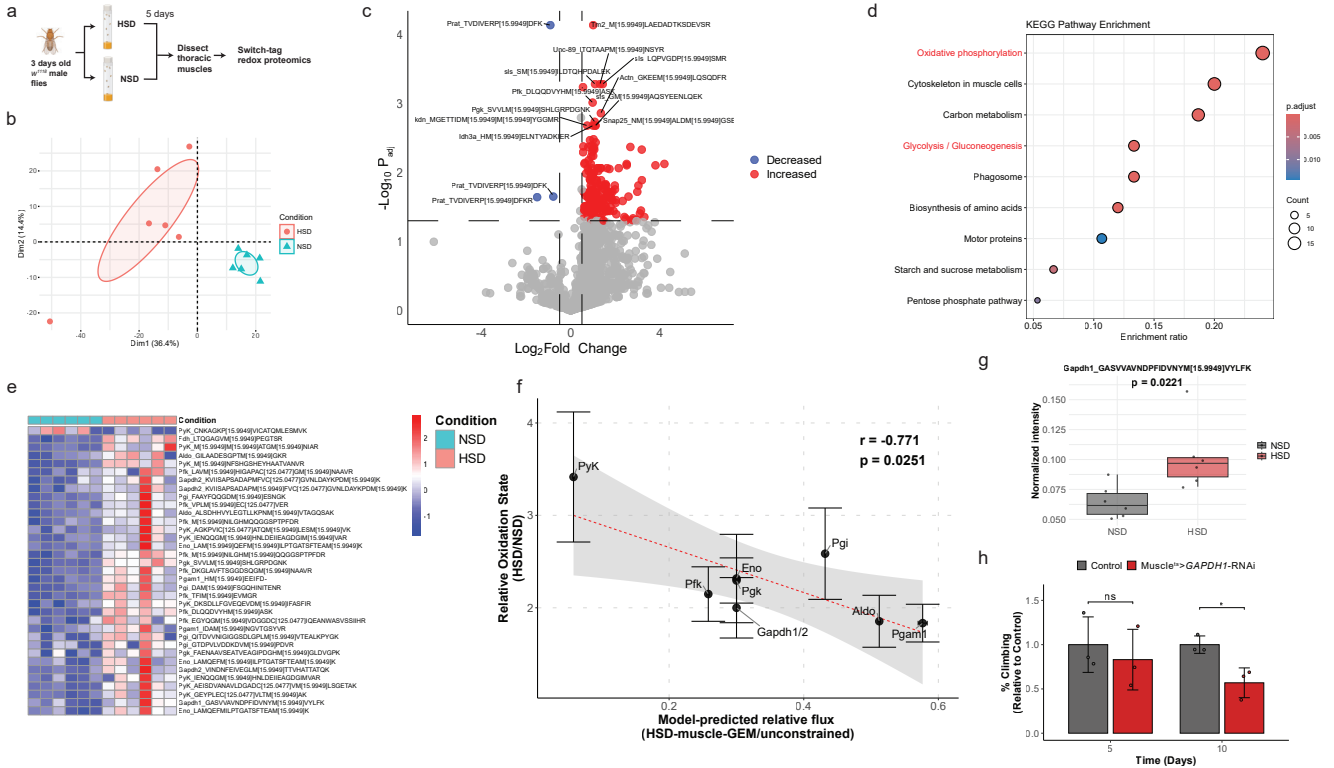
a
3 days old w1118 male flies
HSD
NSD
5 days
Dissect thoracic muscles
Switch-tag redox proteomics
b
Condition
HSD
NSD
Dim1 (36.4%)
Dim2 (14.4%)
c
Decreased
Increased
Log2Fold Change
-Log10 Padj
d
KEGG Pathway Enrichment
Oxidative phosphorylation
Cytoskeleton in muscle cells
Carbon metabolism
Glycolysis / Gluconeogenesis
Phagosome
Biosynthesis of amino acids
Motor proteins
Starch and sucrose metabolism
Pentose phosphate pathway
Enrichment ratio
p.adjust
Count
e
Condition
NSD
HSD
f
r = -0.771
p = 0.0251
PyK
Pgi
Eno
Pfk
Pgk
Gapdh1/2
Aldo
Pgam1
Relative Oxidation State (HSD/NSD)
Model-predicted relative flux (HSD-muscle-GEM/unconstrained)
g
Gapdh1_GASVVAVNDPFIDVNYM[15.9949]VYLFK
p = 0.0221
Normalized intensity
NSD
HSD
h
Control
Muscle>GAPDH1-RNAi
ns
% Climbing (Relative to Control)
Time (Days)

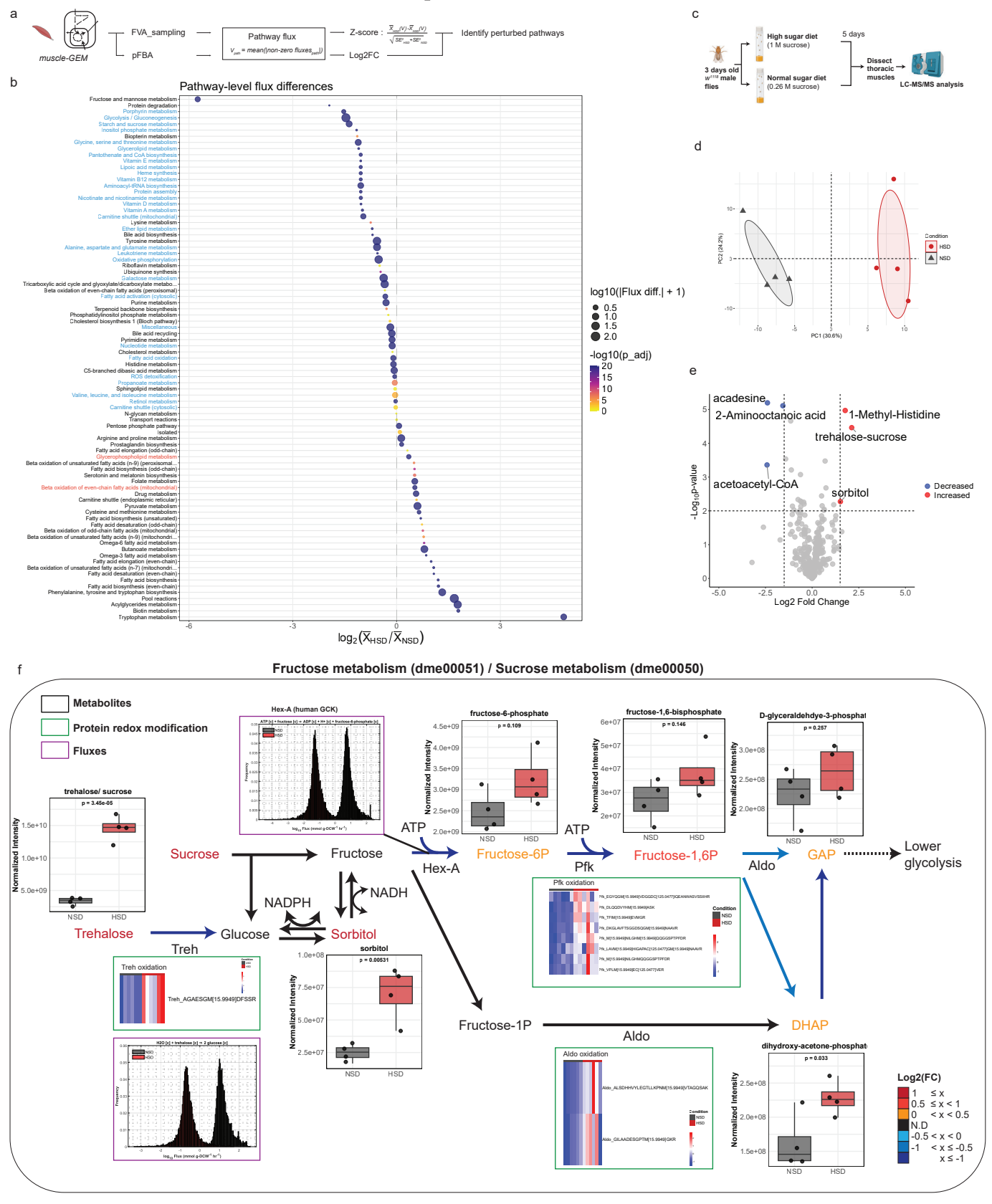
a
muscle-GEM
FVA_sampling
pFBA
Pathway flux
Z-score
Log2FC
Identify perturbed pathways
b
Pathway-level flux differences
log10(|Flux diff.| + 1)
-log10(p_adj)
c
High sugar diet
(1 M sucrose)
Normal sugar diet
(0.26 M sucrose)
3 days old
5 days
Dissect thoracic muscles
LC-MS/MS analysis
d
Condition
HSD
NSD
PC1 (30.6%)
PC2 (24.2%)
e
acadesine
2-Aminooctanoic acid
1-Methyl-Histidine
trehalose-sucrose
acetoacetyl-CoA
sorbitol
Decreased
Increased
Log2 Fold Change
f
Fructose metabolism (dme00051) / Sucrose metabolism (dme00050)
Metabolites
Protein redox modification
Fluxes
Hex-A (human GCK)
fructose-6-phosphate
fructose-1,6-bisphosphate
D-glyceraldehyde-3-phosphat
trehalose/ sucrose
Sucrose
Fructose
ATP
Hex-A
Fructose-6P
Pfk
Fructose-1,6P
Aldo
GAP
Lower glycolysis
NADPH
NADH
Trehalose
Treh
Glucose
Sorbitol
Fructose-1P
DHAP
Treh oxidation
sorbitol
Pfk oxidation
Aldo oxidation
dihydroxy-acetone-phosphat
Log2(FC)

Modeling tissue-specific *Drosophila* metabolism identifies high sugar diet-induced metabolic dysregulation in muscle at reaction and pathway levels

Sun Jin Moon[1*], Yanhui Hu[1], Monika Dzieciatkowska[2], Ah-Ram Kim[1], John M. Asara[3,4], Angelo D'Alessandro[2], Norbert Perrimon[1,5*]

[*]Correspondence: Sun Jin Moon and Norbert Perrimon

Emails: sunjin_moon@hms.harvard.edu and perrimon@genetics.med.harvard.edu

This document includes:

Supplementary Figures 2

Supplementary Figure 1 2

Supplementary Figure 2 4

Supplementary Figure 3 6

Supplementary Figure 4 8

Supplementary Figure 5 10

Supplementary Figure 6 12

Supplementary notes 14

Supplementary note 1: Pathway overlap between tissue-specific GEMs and experimental metabolomics 14

Supplementary note 2: Flux map representing central carbon metabolism 15

Supplementary note 3: Flux comparisons among FBA, FVA-sampling, and pFBA 16

3a. Total flux evaluation: 16

3b. NAD(P)-dependent internal cycling reactions evaluation: 16

3c. Flux boundary effects in FVA-sampling: 17

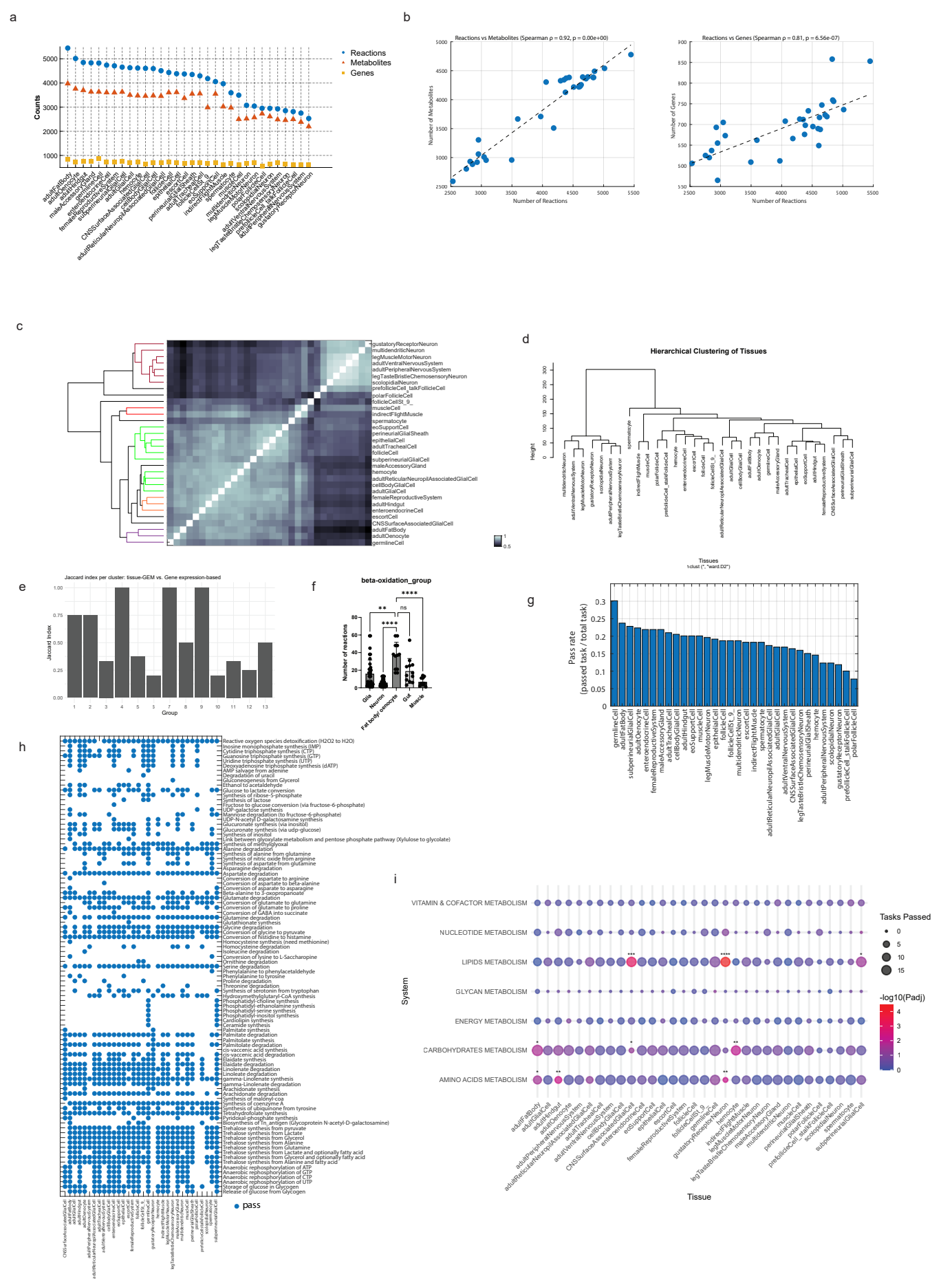
a
Counts
Reactions
Metabolites
Genes
b
Reactions vs Metabolites (Spearman ρ = 0.92, p = 0.00e+00)
Number of Metabolites
Number of Reactions
Reactions vs Genes (Spearman ρ = 0.81, p = 6.56e-07)
Number of Genes
Number of Reactions
c
d
Hierarchical Clustering of Tissues
Height
Tissues
hclust (*, "ward.D2")
e
Jaccard index per cluster: tissue-GEM vs. Gene expression-based
Jaccard index
Group
f
beta-oxidation_group
Number of reactions
Glia
Neuron
Fat body oenocyte
Gut
Muscle
g
Pass rate
(passed task / total task)
h
pass
i
VITAMIN & COFACTOR METABOLISM
NUCLEOTIDE METABOLISM
LIPIDS METABOLISM
GLYCAN METABOLISM
ENERGY METABOLISM
CARBOHYDRATES METABOLISM
AMINO ACIDS METABOLISM
System
Tasks Passed
-log10(Padj)
Tissue

Supplementary Figure 1. Reconstruction of 32 tissue-specific genome-scale metabolic models (GEMs) in *Drosophila melanogaster*

a Dot plot showing the number of reactions, metabolites, and genes across tissue-specific GEMs. **b** Scatter plot of reactions vs. metabolites (left) and vs. genes (right) with spearman correlation and p-value. The Spearman correlation coefficient and the p-values are displayed. **c** The heatmap representing the pairwise similarity matrix of tissue-specific GEMs, with branch colors highlighting distinct clusters for major tissues, including neuron, glia, muscle, gut, and fat body. The color scale on the bottom right indicates the degree of similarity, where lighter colors represent higher similarity and darker colors indicate lower similarity. **d** Dendrogram of hierarchical clustering of tissues based on pseudo-bulk snRNA-seq data. Euclidean distance metric and Ward's method were used to group tissues with similar gene expression profiles. **e** The bar plot shows the Jaccard indices for each cluster, comparing tissue-GEM-based clusters with gene expression derived clusters. Each bar is reference to a group obtained from tissue-specific GEMs. Representative groups are group 1(fat body, oenocyte), group 3 (hindgut and enteroendocrine cell), group 7 (muscle and indirect muscle), group 4 (seven types of neurons), group 2, 5, and 11 (six types of glia). The rest clusters consist of other tissues. **f** Number of reactions in beta-oxidation fatty acid metabolism subsystem. Statistical significance was assessed using a Kruskal–Wallis test followed by Dunn's multiple comparisons test (5 groups; $p < 0.0001$; $n_{glia} = 36$, $n_{neuron} = 42$, $n_{fatbody/oenocyte} = 12$, $n_{gut} = 12$, $n_{muscle} = 12$). Data are shown as mean ± SD from biological replicates (n = 5). The significance was represented as follows: $*\ P < 0.05$, $**\ P < 0.01$, $***\ P < 0.001$,$****\ P < 0.0001$. **g** Metabolic task pass rate. Total number of metabolic tasks were divided by the total number of metabolic tasks. **h** Visualization of tissue-specific GEMs' ability to complete distinct metabolic tasks. Of 219 metabolic tasks, at least one tissue-GEM was able to complete 93 metabolic tasks as shown in the plot. Blue dots represent the models' passing the metabolic tasks. The presence of a dot indicates that the tissue-GEM was able to complete the respective task. Data can be found in supplementary data 1. **i** Tissue-specific enrichment of metabolic tasks across tissue-specific GEMs. Enrichment of metabolic tasks was assessed using Fisher's exact test applied to a 2×2 contingency table for each metabolic system–tissue pair. P values were corrected for multiple testing using the Benjamini–Hochberg FDR method. Each bubble represents a metabolic system–task association, where bubble size indicates the number of tasks passed in that system for the given tissue-specific GEM, and color intensity reflects the statistical significance. $*\ P < 0.05$, $**\ P < 0.01$, $***\ P < 0.001$,$****\ P < 0.0001$.

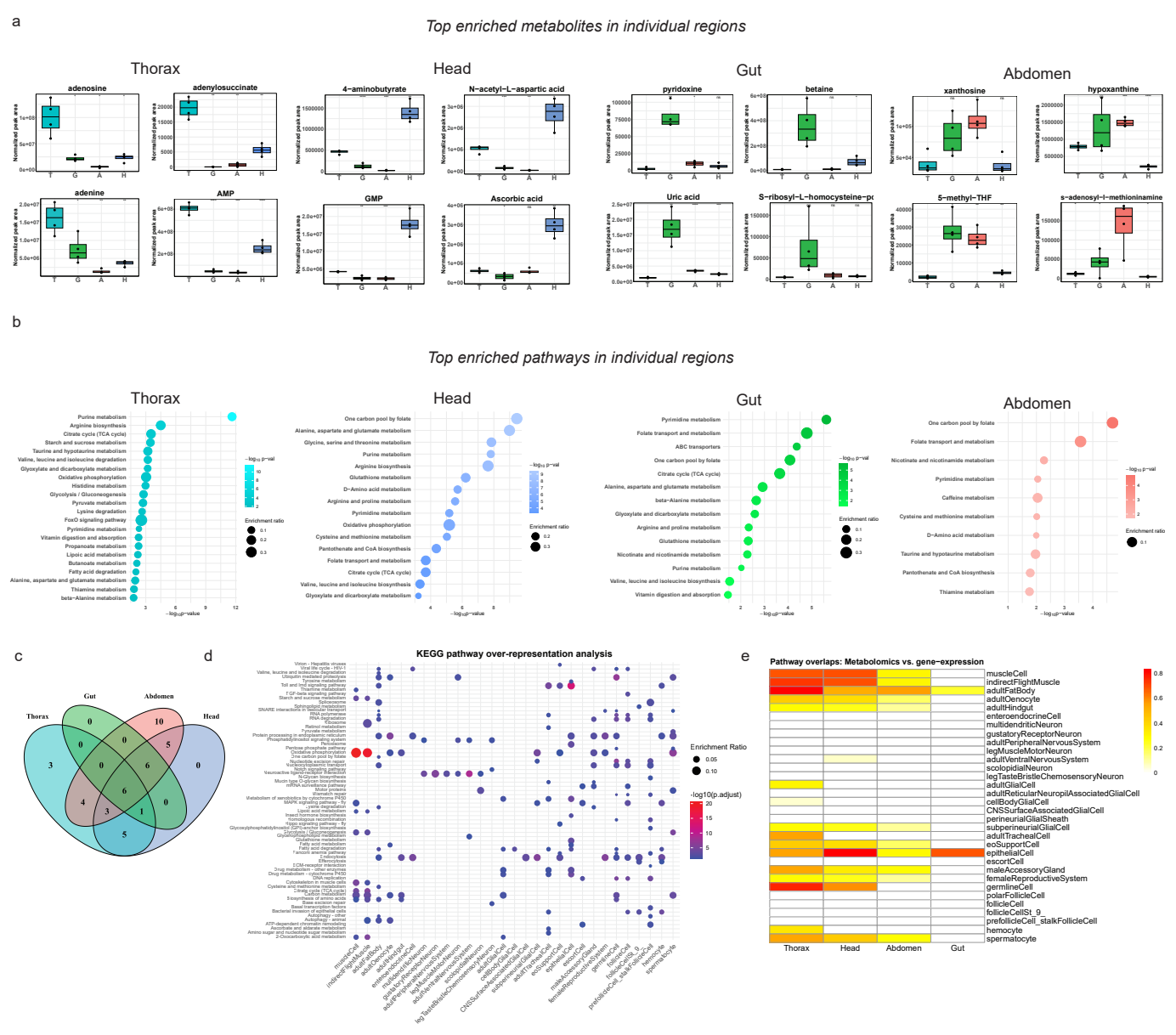
a
Top enriched metabolites in individual regions
Thorax
Head
Gut
Abdomen
adenosine
adenylosuccinate
4−aminobutyrate
N−acetyl−L−aspartic acid
pyridoxine
betaine
xanthosine
hypoxanthine
adenine
AMP
GMP
Ascorbic acid
Uric acid
S−ribosyl−L−homocysteine−pc
5−methyl−THF
s−adenosyl−l−methioninamine
Normalized peak area
T G A H
b
Top enriched pathways in individual regions
Thorax
Purine metabolism
Arginine biosynthesis
Citrate cycle (TCA cycle)
Starch and sucrose metabolism
Taurine and hypotaurine metabolism
Valine, leucine and isoleucine degradation
Glyoxylate and dicarboxylate metabolism
Oxidative phosphorylation
Histidine metabolism
Glycolysis / Gluconeogenesis
Pyruvate metabolism
Lysine degradation
FoxO signaling pathway
Pyrimidine metabolism
Vitamin digestion and absorption
Propanoate metabolism
Lipoic acid metabolism
Butanoate metabolism
Fatty acid degradation
Alanine, aspartate and glutamate metabolism
Thiamine metabolism
beta−Alanine metabolism
Head
One carbon pool by folate
Alanine, aspartate and glutamate metabolism
Glycine, serine and threonine metabolism
Purine metabolism
Arginine biosynthesis
Glutathione metabolism
D−Amino acid metabolism
Arginine and proline metabolism
Pyrimidine metabolism
Oxidative phosphorylation
Cysteine and methionine metabolism
Pantothenate and CoA biosynthesis
Folate transport and metabolism
Citrate cycle (TCA cycle)
Valine, leucine and isoleucine biosynthesis
Glyoxylate and dicarboxylate metabolism
Gut
Pyrimidine metabolism
Folate transport and metabolism
ABC transporters
One carbon pool by folate
Citrate cycle (TCA cycle)
Alanine, aspartate and glutamate metabolism
beta−Alanine metabolism
Glyoxylate and dicarboxylate metabolism
Arginine and proline metabolism
Glutathione metabolism
Nicotinate and nicotinamide metabolism
Purine metabolism
Valine, leucine and isoleucine biosynthesis
Vitamin digestion and absorption
Abdomen
One carbon pool by folate
Folate transport and metabolism
Nicotinate and nicotinamide metabolism
Pyrimidine metabolism
Caffeine metabolism
Cysteine and methionine metabolism
D−Amino acid metabolism
Taurine and hypotaurine metabolism
Pantothenate and CoA biosynthesis
Thiamine metabolism
−log10 p−val
Enrichment ratio
−log10p−value
c
Thorax
Gut
Abdomen
Head
d
KEGG pathway over-representation analysis
Enrichment Ratio
-log10(p.adjust)
e
Pathway overlaps: Metabolomics vs. gene−expression
muscleCell
indirectFlightMuscle
adultFatBody
adultOenocyte
adultHindgut
enteroendocrineCell
multidendriticNeuron
gustatoryReceptorNeuron
adultPeripheralNervousSystem
legMuscleMotorNeuron
adultVentralNervousSystem
scolopidialNeuron
legTasteBristleChemosensoryNeuron
adultGlialCell
adultReticularNeuropilAssociatedGlialCell
cellBodyGlialCell
CNSSurfaceAssociatedGlialCell
perineurialGlialSheath
subperineurialGlialCell
adultTrachealCell
eoSupportCell
epithelialCell
escortCell
maleAccessoryGland
femaleReproductiveSystem
germlineCell
polarFollicleCell
follicleCell
follicleCellSt_9
prefollicleCell_stalkFollicleCell
hemocyte
spermatocyte
Thorax
Head
Abdomen
Gut

Supplementary Figure 2. Validation of tissue-specific GEMs through regional metabolomics and pathway analysis

a Boxplots represent the normalized peak area of selected metabolites in thorax (T), head (H), gut (G), and abdomen (A). Center line is median; box limits are first and third quartiles; whiskers are 1.5 × interquartile range (n=4). One-way ANOVA was used to calculate p-values across groups. Pairwise comparisons between each tissue and thorax were then conducted using post-hoc t-tests with Benjamini–Hochberg (BH) correction for multiple comparisons. $*\ P < 0.05,\ **\ P < 0.01,\ ***\ P < 0.001, ****\ P < 0.0001$. **b** Bubble plots show significantly enriched metabolic pathways across four dissected *Drosophila* regions: thorax, head, gut, and abdomen. Each bubble represents a KEGG pathway. The x-axis displays the enrichment significance as $-\log_{10}$(p-value), calculated using a Fisher's exact over-representation test. Bubble size corresponds to the enrichment ratio (observed/expected). Bubble color reflects region-specific plots (cyan: thorax, blue: head, green: gut, pink: abdomen). **c** Venn diagram of enriched pathways across regions. **d** KEGG enrichment analysis (over-representation) for pseudo-bulk snRNA-seq data. Each dot represents a KEGG pathway enriched in a specific tissue or cell type, based on over-representation analysis of genes from pseudo-bulk single-nucleus RNA-seq (snRNA-seq) data. The x-axis shows *Drosophila* tissues/cell types; the y-axis lists KEGG pathways. Dot color represents the statistical significance of enrichment, scaled as $-\log_{10}$(adjusted p-value), with red colors indicating higher significance. Dot size reflects the enrichment ratio (observed vs. expected counts). Enrichment was assessed using a Fisher's exact test with Benjamini–Hochberg correction. Tissues with no significantly enriched pathways in a given category are left blank. **e** Pathway overlaps between metabolomics and gene-expression analysis. The heatmap shows the weighted Jaccard index between pathways enriched from metabolomics (per dissected region: thorax, head, abdomen, gut) and pathways inferred from KEGG over-representation analysis based on gene expression levels of individual tissues. Rows represent *Drosophila* cell types or tissues, and columns correspond to the four anatomical regions profiled in metabolomics. Color intensity reflects the degree of overlap, with red indicating stronger pathway agreement (weighted Jaccard index, scale 0–0.8). Blank cells indicate no overlap or missing data.

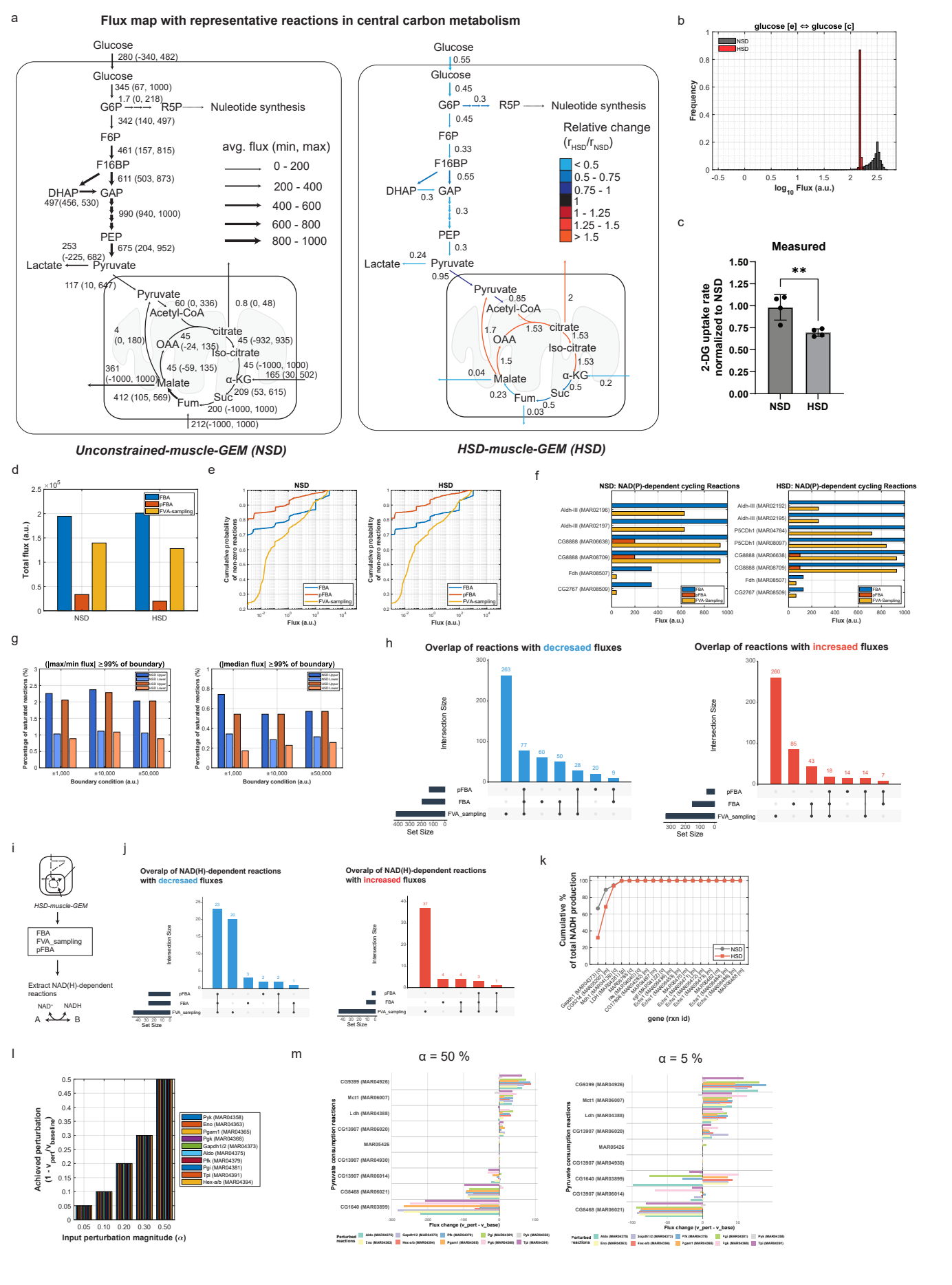
a
Flux map with representative reactions in central carbon metabolism
Glucose
280 (-340, 482)
Glucose
345 (67, 1000)
1.7 (0, 218)
G6P
R5P
Nuleotide synthesis
342 (140, 497)
F6P
461 (157, 815)
F16BP
611 (503, 873)
DHAP
GAP
497(456, 530)
990 (940, 1000)
PEP
675 (204, 952)
253
(-225, 682)
Lactate
Pyruvate
avg. flux (min, max)
0 - 200
200 - 400
400 - 600
600 - 800
800 - 1000
117 (10, 647)
Pyruvate
60 (0, 336)
0.8 (0, 48)
Acetyl-CoA
4
(0, 180)
45
(-24, 135)
citrate
45 (-932, 935)
OAA
Iso-citrate
45 (-59, 135)
45 (-1000, 1000)
361
(-1000, 1000)
Malate
α-KG
165 (30, 502)
412 (105, 569)
Fum
Suc
209 (53, 615)
200 (-1000, 1000)
212(-1000, 1000)
Unconstrained-muscle-GEM (NSD)
Glucose
0.55
Glucose
0.45
G6P
0.3
R5P
Nuleotide synthesis
0.45
F6P
0.33
F16BP
0.55
DHAP
0.3
GAP
0.3
PEP
0.3
Lactate
0.24
Pyruvate
0.95
Relative change
(r_HSD/r_NSD)
< 0.5
0.5 - 0.75
0.75 - 1
1
1 - 1.25
1.25 - 1.5
> 1.5
Pyruvate
0.85
2
Acetyl-CoA
1.7
1.53
citrate
1.53
OAA
Iso-citrate
1.5
1.53
0.04
Malate
α-KG
0.2
0.23
Fum
Suc
0.5
0.5
0.03
HSD-muscle-GEM (HSD)
b
glucose [e] ⇔ glucose [c]
NSD
HSD
Frequency
log10 Flux (a.u.)
c
Measured
2-DG uptake rate normalized to NSD
**
NSD
HSD
d
Total flux (a.u.)
FBA
pFBA
FVA-sampling
NSD
HSD
e
NSD
HSD
Cumulative probability of non-zero reactions
Flux (a.u.)
FBA
pFBA
FVA-sampling
f
NSD: NAD(P)-dependent cycling Reactions
HSD: NAD(P)-dependent cycling Reactions
Aldh-III (MAR02196)
Aldh-III (MAR02197)
CG8888 (MAR06638)
CG8888 (MAR08709)
Fdh (MAR08507)
CG2767 (MAR08509)
Aldh-III (MAR02192)
Aldh-III (MAR02195)
P5CDh1 (MAR04784)
P5CDh1 (MAR08097)
Flux (a.u.)
g
(|max/min flux| ≥99% of boundary)
(|median flux| ≥99% of boundary)
Percentage of saturated reactions (%)
Boundary condition (a.u.)
±1,000
±10,000
±50,000
h
Overlap of reactions with decresaed fluxes
Overlap of reactions with incresaed fluxes
Intersection Size
Set Size
pFBA
FBA
FVA_sampling
263
77
60
50
28
20
9
260
85
43
18
14
14
7
i
HSD-muscle-GEM
FBA
FVA_sampling
pFBA
Extract NAD(H)-dependent reactions
NAD+
NADH
A
B
j
Overalp of NAD(H)-dependent reactions with decresaed fluxes
Overalp of NAD(H)-dependent reactions with increased fluxes
Intersection Size
Set Size
pFBA
FBA
FVA_sampling
23
20
3
2
2
1
37
4
4
3
1
k
Cumulative % of total NADH production
NSD
HSD
gene (rxn id)
l
Achieved perturbation
Input perturbation magnitude (α)
Pyk (MAR04358)
Eno (MAR04363)
Pgam1 (MAR04365)
Pgk (MAR04368)
Gapdh1/2 (MAR04373)
Aldo (MAR04375)
Pfk (MAR04379)
Pgi (MAR04381)
Tpi (MAR04391)
Hex-a/b (MAR04394)
m
α = 50 %
α = 5 %
Pyruvate consumption reactions
CG9399 (MAR04926)
Mct1 (MAR06007)
Ldh (MAR04388)
CG13907 (MAR06020)
MAR05426
CG13907 (MAR04930)
CG13907 (MAR06014)
CG8468 (MAR06021)
CG1640 (MAR03899)
Flux change (v_pert - v_base)
Perturbed reactions

Supplementary Figure 3. Constraint-based flux analyses predict perturbations in NAD(H)-dependent reactions in muscle under high sugar diet

a Constraint-based flux analysis shows representative fluxes in central carbon metabolism. Arrows indicate the direction and magnitude of average predicted fluxes (arbitrary units), with the corresponding minimum and maximum fluxes for each reaction shown in parentheses. Representative fluxes were obtained from FVA-sampling. Only key reactions in central pathways are shown, while detailed reaction sets are provided in Supplementary Data 3c–d. **b** Model-predicted flux distribution of glucose uptake reaction (glucose[e] ⇔ glucose[c]) (n_{sim}=10,000). **c** Glucose uptake in thoracic muscle. 2-deoxyglucose (2-DG) uptake rate was measured in dissected thoracic muscles from adult male flies fed NSD or HSD after 5 days using the kit (Promega: J1341). Data are shown as mean ± SD from biological replicates (n = 5). Statistical significance was assessed using a two-tailed unpaired t-test; ** $p < 0.01$. **d** Total flux in the muscle-GEM was quantified. **e** Empirical cumulative distribution functions of non-zero reaction fluxes. **f** NAD(P)-dependent cycling reactions. Horizontal bars show flux magnitudes from FBA, pFBA, and FVA_sampling analysis for the top cycling reactions ranked by flux reduction. **g** Percentage of reactions exhibiting saturation across boundary conditions. **h** Overlap of reactions with commonly decreased (blue) and increased (red) fluxes under HSD compared to NSD, as identified by pFBA, FBA, and FVA sampling analyses. UpSet plots were used to indicate total and intersecting sets of reactions showing consistent flux changes across methods. **i** Workflow for identifying commonly perturbed NAD(H)-dependent reactions in HSD-muscle-GEM. Differential reaction fluxes were computed using FBA, FVA sampling, and pFBA. **j** Overlap of NAD(H)-dependent reactions. **k** Cumulative percentage contribution of individual NADH-producing reactions to total NADH production capacity under NSD and HSD conditions. **l** Bar plots showing achieved perturbation magnitude. Each colored bar represents the achieved perturbation for a specific enzyme across conditions, with baseline flux estimated as the median from 5,000 FVA sampling points per reaction. **m** Bar plots showing changes in flux through individual pyruvate-consuming reactions following 50% (left) and 5% (right) flux reductions in each targeted glycolytic enzyme.

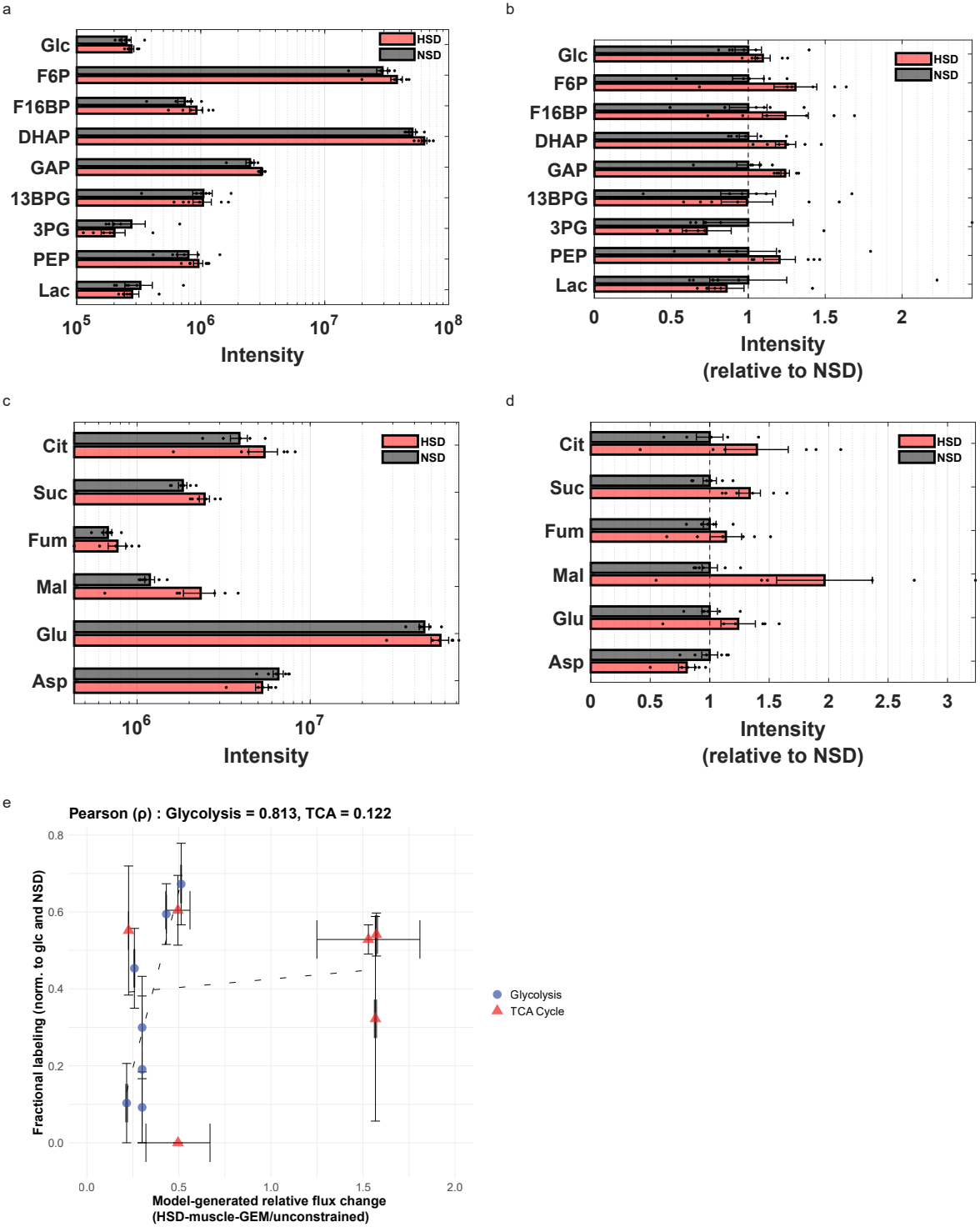
a
Glc
F6P
F16BP
DHAP
GAP
13BPG
3PG
PEP
Lac
HSD
NSD
10^5
10^6
10^7
10^8
Intensity
b
Glc
F6P
F16BP
DHAP
GAP
13BPG
3PG
PEP
Lac
HSD
NSD
0
0.5
1
1.5
2
Intensity
(relative to NSD)
c
Cit
Suc
Fum
Mal
Glu
Asp
HSD
NSD
10^6
10^7
Intensity
d
Cit
Suc
Fum
Mal
Glu
Asp
HSD
NSD
0
0.5
1
1.5
2
2.5
3
Intensity
(relative to NSD)
e
Pearson (ρ) : Glycolysis = 0.813, TCA = 0.122
Fractional labeling (norm. to glc and NSD)
0.0
0.2
0.4
0.6
0.8
0.0
0.5
1.0
1.5
2.0
Model-generated relative flux change
(HSD-muscle-GEM/unconstrained)
Glycolysis
TCA Cycle

Supplementary Figure 4. Model-predicted decreases in glycolytic flux, including GAPDH, validated through ^{13}C-glucose tracing

(a, b) absolute (**a**) and relative (**b**) intensities of glycolytic intermediates detected from LC/MS analysis in response to HSD and NSD. Bars represent mean ± SEM, and individual points indicate biological replicates (n = 6). M+x denotes a mass isotopomer containing x ^{13}C atoms. For (b), values are normalized to the mean NSD intensity for each metabolite. Measured metabolites: Glc (glucose), F6P (fructose-6-phosphate), F16BP (fructose-1,6-bisphosphate), DHAP (dihydroxyacetone phosphate), GAP (glyceraldehyde-3-phosphate), 13BPG (1,3-bisphosphoglycerate), 3PG (3-phosphoglycerate), PEP (phosphoenolpyruvate), and Lac (lactate). **(c, d)** Absolute (**c**) and relative (**d**) intensities of TCA cycle intermediates and amino acids. Metabolites: Cit (citrate), Suc (succinate), Fum (fumarate), Mal (malate), Glu (glutamate), Asp (aspartate). Bars represent mean ± SEM, and individual points indicate biological replicates (n = 6). M+x denotes a mass isotopomer containing x ^{13}C atoms. **e.** Scatter plot comparing experimentally measured fractional labeling (normalized to glucose and NSD) with relative flux changes predicted by the HSD muscle-GEM model for glycolytic (blue circles) and TCA cycle (red triangles) intermediates. Fractional labeling values (y-axis) are shown as mean ± SEM from biologically independent replicates (n = 6), and model-predicted flux values (x-axis) are shown as mean ± SEM from flux sampling simulations (n = 10,000). The dashed red line represents a linear regression fit. A two-sided Pearson's correlation coefficients (ρ) are shown for glycolysis and TCA cycle metabolites.

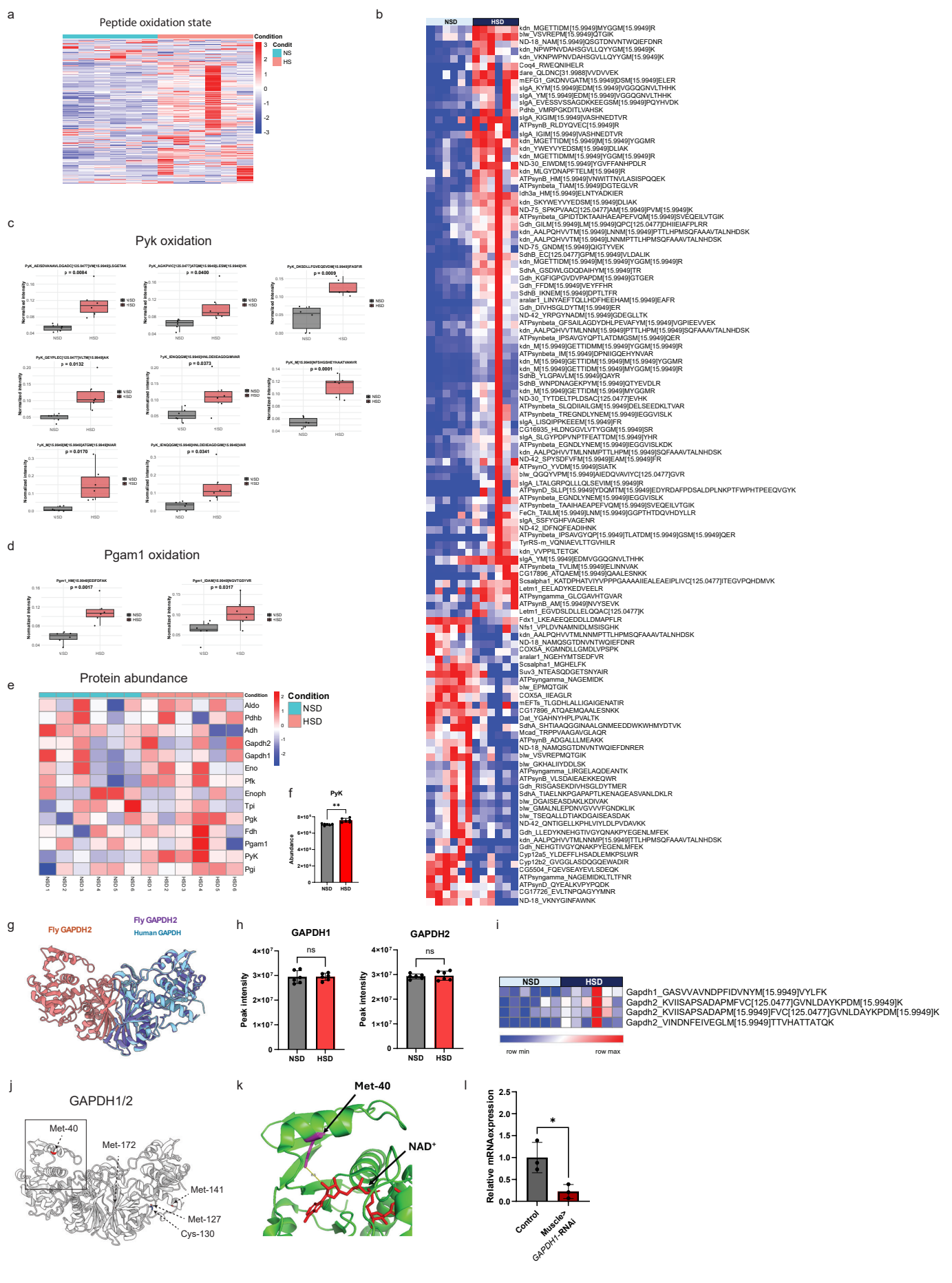
a
Peptide oxidation state
Condition
NS
HS
b
NSD
HSD
c
Pyk oxidation
d
Pgam1 oxidation
e
Protein abundance
Condition
NSD
HSD
Aldo
Pdhb
Adh
Gapdh2
Gapdh1
Eno
Pfk
Enoph
Tpi
Pgk
Fdh
Pgam1
PyK
Pgi
f
PyK
Abundance
g
Fly GAPDH2
Fly GAPDH2
Human GAPDH
h
GAPDH1
GAPDH2
Peak intensity
ns
NSD
HSD
i
NSD
HSD
Gapdh1_GASVVAVNDPFIDVNYM[15.9949]VYLFK
Gapdh2_KVIISAPSADAPMFVC[125.0477]GVNLDAYKPDM[15.9949]K
Gapdh2_KVIISAPSADAPM[15.9949]FVC[125.0477]GVNLDAYKPDM[15.9949]K
Gapdh2_VINDNFEIVEGLM[15.9949]TTVHATTATQK
row min
row max
j
GAPDH1/2
Met-40
Met-172
Met-141
Met-127
Cys-130
k
Met-40
NAD+
l
Relative mRNAexpression
Control
Muscle>
GAPDH1-RNAi

Supplementary Figure 5. Model-predicted decreases in glycolytic flux correlate with increased redox modification of glycolytic enzymes

a Heatmap showing the oxidation state values of significantly altered peptides under normal sugar diet (NSD) and high sugar diet (HSD) conditions (n=6). Each row represents a peptide; each column corresponds to a biological replicate. Color scale represents oxidation state, with red indicating greater oxidation. **b** Heatmap showing mitochondrial peptide oxidation states (n=6). The color scale reflects z-score normalized oxidation states, with red indicating increased oxidation levels and blue indicating decreased oxidation levels relative to mean of each row. The raw data is found in the supplementary data. 5a**. (c, d) (c)** Boxplot showing the normalized intensity of significantly oxidized peptides for pyruvate kinase (Pyk) and **(d)** phosphoglycerate mutase 1 (Pgam1) under NSD and HSD conditions**.** Center line is median; box limits are first and third quartiles; whiskers are 1.5 × interquartile range; points represent biologically independent replicates (n = 6). Statistical significance was assessed using a two-tailed unpaired t-test and the p-value is shown above the plot. **e** Heatmap of glycolytic enzyme abundances in muscle tissues under NSD and HSD conditions (n=6)**.** Rows correspond to individual enzymes and columns to biological replicates under each condition. **f** Bar plot showing relative abundance of pyruvate kinase (PyK) in NSD and HSD samples. Data are shown as mean ± SD from biological replicates (n = 6). Statistical significance was assessed using a two-tailed unpaired t-test; ** $p < 0.01$. g Predicted enzyme structures and the interactions among fly GAPDH1 (FBgn0001091), fly GAPDH2 (FBgn0001091) and the overlapped structure of human GAPDH by Alphafold2-multimer. **h** Bar plots show peak intensity values for GAPDH1 and GAPDH2 proteins measured in muscle under NSD and HSD conditions. Data are shown as mean ± SD from biological replicates (n = 6). Statistical significance was assessed using a two-tailed unpaired t-test; "ns" denotes no statistically significant difference. **i** Heatmap of peptide abundances for GAPDH1 and GAPDH2. Rows represent distinct peptides detected and assigned to GAPDH1 or GAPDH2, with peptide sequences listed at right (n=6). **j** Predicted enzyme structures and the interactions between GAPDH1 (FBgn0001091) and GAPDH2 (FBgn0001091) by Alphafold2-multimer. The oxidized methionine and cysteine residues are highlighted. **k** The NAD^+ binding pocket and the surrounding area from GAPDH monomer structure (PDB: 1U8F) is shown. NAD^+ and methionine resides are highlighted in red and purple, respectively. **l** qPCR analysis of dGAPDH1 mRNA Expression. Quantification of dGAPDH1 mRNA expression in muscle tissue from Control (gray) and Muscle>GAPDH1-RNAi (red) male flies using quantitative PCR (qPCR). The thoraces were collected after five days of GAPDH1-RNAi activation. Data are shown as mean ± SD from biological replicates (n = 6). Statistical significance was assessed using a two-tailed unpaired t-test; * $p < 0.05$.

a

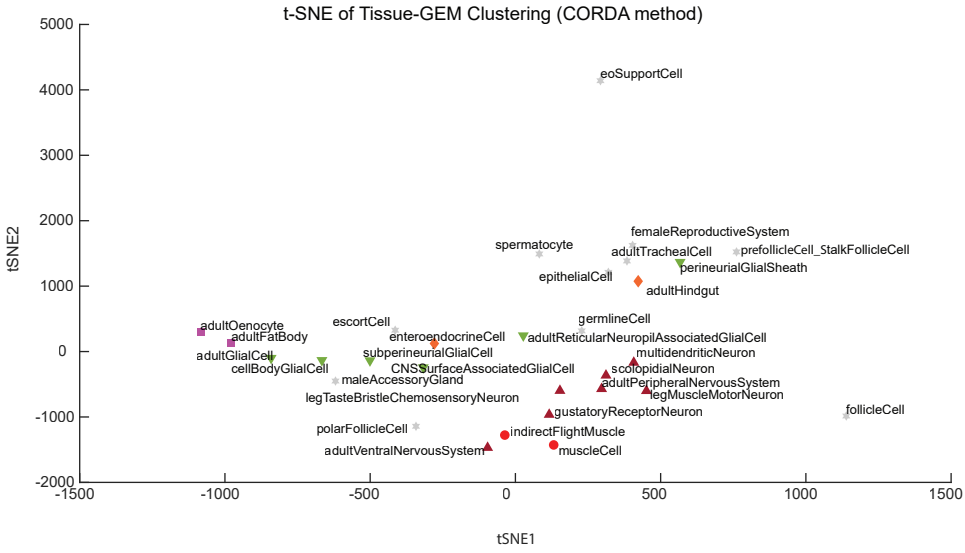
t-SNE of Tissue-GEM Clustering (CORDA method)
tSNE2
tSNE1
5000
4000
3000
2000
1000
0
-1000
-2000
-1500
-1000
-500
0
500
1000
1500
eoSupportCell
femaleReproductiveSystem
spermatocyte
adultTrachealCell
prefollicleCell_StalkFollicleCell
perineurialGlialSheath
epithelialCell
adultHindgut
adultOenocyte
escortCell
germlineCell
adultFatBody
enteroendocrineCell
adultReticularNeuropilAssociatedGlialCell
adultGlialCell
subperineurialGlialCell
multidendriticNeuron
cellBodyGlialCell
CNSSurfaceAssociatedGlialCell
scolopidialNeuron
maleAccessoryGland
adultPeripheralNervousSystem
legTasteBristleChemosensoryNeuron
legMuscleMotorNeuron
gustatoryReceptorNeuron
follicleCell
polarFollicleCell
indirectFlightMuscle
adultVentralNervousSystem
muscleCell

b

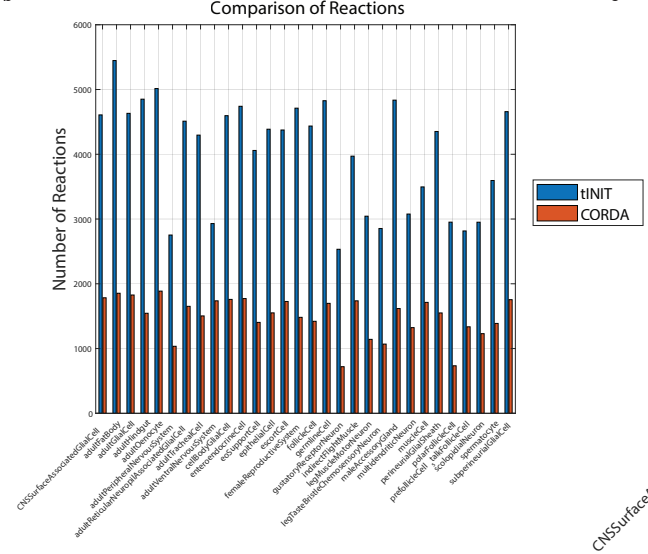
Comparison of Reactions
Number of Reactions
6000
5000
4000
3000
2000
1000
0
tINIT
CORDA
CNSSurfaceAssociatedGlialCell
adultFatBody
adultGlialCell
adultHindgut
adultOenocyte
adultNervousSystem
adultTrachealCell
adultVentralNervousSystem
cellBodyGlialCell
enteroendocrineCell
eoSupportCell
epithelialCell
escortCell
femaleReproductiveSystem
germlineCell
follicleCell
gustatoryReceptorNeuron
indirectFlightMuscle
legMuscleMotorNeuron
maleAccessoryGland
multidendriticNeuron
muscleCell
perineurialGlialSheath
polarFollicleCell
prefollicleCell
scolopidialNeuron
spermatocyte
subperineurialGlialCell

c

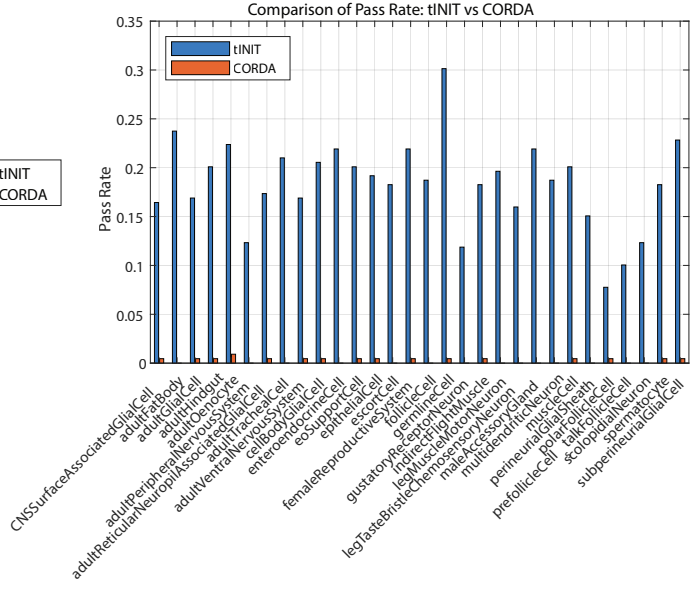
Comparison of Pass Rate: tINIT vs CORDA
Pass Rate
0.35
0.3
0.25
0.2
0.15
0.1
0.05
0
tINIT
CORDA
CNSSurfaceAssociatedGlialCell
adultFatBody
adultGlialCell
adultHindgut
adultOenocyte
adultNervousSystem
adultPeripheralNervousSystem
adultReticularNeuropilAssociatedGlialCell
adultTrachealCell
adultVentralNervousSystem
cellBodyGlialCell
enteroendocrineCell
eoSupportCell
epithelialCell
escortCell
femaleReproductiveSystem
follicleCell
germlineCell
gustatoryReceptorNeuron
indirectFlightMuscle
legMuscleMotorNeuron
legTasteBristleChemosensoryNeuron
maleAccessoryGland
multidendriticNeuron
muscleCell
perineurialGlialSheath
polarFollicleCell
prefollicleCell
scolopidialNeuron
spermatocyte
subperineurialGlialCell

Supplementary Figure 6. Comparison of metabolic network structures obtained through tINIT and CORDA algorithms

a t-SNE plot comparing the metabolic network structures of tissue-specific GEMs reconstructed by CORDA algorithm. Each point represents a tissue-specific GEM, positioned by t-SNE dimensionality reduction based on network structure similarities. Five major tissue groups were highlighted – muscle (red circles), fat body/oenocyte (purple squares), neuron (dark red upward triangles), glia (green downward triangles), gut (orange diamonds), and others (gray stars). **b** Bar plot compares the number of metabolic reactions included in tissue-specific metabolic models generated using two different reconstruction algorithms: tINIT (blue) and CORDA (orange). **c** Bar plot compares the metabolic task pass rate of metabolic models reconstructed using two different algorithms: tINIT (blue) and CORDA (orange).

Supplementary notes

Supplementary note 1: Pathway overlap between tissue-specific GEMs and experimental metabolomics

The goal of this analysis was to compare enriched pathways identified from tissue-specific GEMs with those from regional metabolomics data, using GEM subsystem annotations as a shared reference framework. The steps are as follows:

First, enriched pathways were determined from each tissue-specific GEM using subsystem coverage analysis (Methods: "Metabolic network structure, subsystem coverage, and metabolic task analysis"). Second, regional metabolomics data were analyzed using KEGG over-representation analysis (ORA) to determine significantly enriched pathways (Methods: *"KEGG over-representation analysis for metabolomics"*). Third, to enable direct comparison, enriched KEGG pathway identified from metabolomics were mapped to GEM subsystem names using a manually curated one-to-one mapping table (**Supplementary Data 2e**). Where no exact mapping existed, the original KEGG pathway names were retained. Subsequent analyses were conducted using the standardized GEM subsystem annotations. Fourth, pathway overlap was quantified using a weighted Jaccard index, which integrates both pathway overlap and enrichment significance (Methods: *"Quantification of pathway overlap using weighted Jaccard index"*).

Supplementary note 2: Flux map representing central carbon metabolism

This note provides additional context for the flux map analysis shown in **Supplementary Figure 3a** and the corresponding data in **Supplementary Data 3c** and **d**. Specifically, it illustrates how central carbon metabolism, particularly tricarboxylic acid (TCA) cycle, is altered in the HSD-muscle-GEM relative to the control model, based on the FVA sampling analysis.

As described in Methods (*Flux variability analysis and flux sampling analysis*), we calculated representative fluxes (e.g., mean, median, mode, minimum, and maximum flux values) across 13 TCA cycle–associated reactions. These included citrate synthase (KDN), aconitase (mAcon1/2), isocitrate dehydrogenase (IDH3, IDH), α-ketoglutarate dehydrogenase (OGDH), succinyl-CoA synthetase (Scsα1/β), succinate dehydrogenase (SDH), fumarase (FUM), malate dehydrogenase (MDH2), malic enzyme (MEN), and associated metabolite transporters (Dic1-mediated citrate, α-ketoglutarate, fumarate, and malate transport) (**Supplementary Data 3c).**

Comparison of individual reaction fluxes revealed decreases in OGDH and SDH by approximately 50% relative to control, and increases in MEN, MDH2, CS, and IDH by approximately 150%. When these 13 reactions were averaged across conditions, the overall TCA cycle flux decreased by about 50% in the HSD-muscle-GEM. Additionally, we confirmed balanced production and consumption rates for malate, citrate, α-ketoglutarate, fumarate in mitochondrial compartment, consistent with the steady-state assumption used in flux analyses (see **Supplementary Data 3d**)

Together, the model-predicted increase in upper-cycle and decrease in lower-cycle reactions indicate that the individual fluxes in TCA cycle is not strictly same in part due to transporter fluxes, leading to differential changes in individual reaction fluxes in HSD-muscle-GEM relative to the control.

Supplementary note 3: Flux comparisons among FBA, FVA-sampling, and pFBA

To evaluate altered reactions beyond those directly constrained in central carbon metabolism, we systematically compared predicted flux profiles from FBA, FVA-sampling, and pFBA analyses (see **Methods**). Each method offers distinct advantages and limitations: FVA-sampling explores the entire feasible solution space, capturing metabolic flexibility but potentially introducing unrealistically high fluxes through internal cycling reactions. In contrast, pFBA provides a single parsimonious solution that minimizes total flux and suppresses internal cycling to better reflect enzyme economy, but it may overlook alternative flux distributions. Standard FBA falls between FVA-sampling and pFBA. Thus, we reasoned comparing differential fluxes from these methods provided a more robust flux analysis framework, especially for identifying perturbed reaction sets.

3a. Total flux evaluation:

To validate the robustness of pFBA, we compared the total flux and internal cycling reactions after performing the FBA, pFBA, and FVA-sampling flux simulations. Comparison of total flux revealed a substantial decrease with pFBA relative to FBA and FVA-sampling (**Supplementary Figure 3d**). Specifically, total flux decreased by approximately 76 % and 85 % relative to FVA-sampling under NSD and HSD conditions, respectively. Moreover, only about 20 % of reactions carried non-zero fluxes in pFBA, whereas about 80 % of reactions carried non-zero fluxes in FVA-sampling (**Supplementary Figure 3e**). The higher total flux and greater number of active reactions observed in FVA-sampling likely result from the inclusion of fluxes through parallel pathways and internal cycles.

3b. NAD(P)-dependent internal cycling reactions evaluation:

Internal cycling reactions can occur in under-constrained metabolic networks when fluxes circulate, often leading to inflated total flux or unrealistic pathway activity. To evaluate such internal cycles, we focused on NAD(P)-dependent reactions as these reactions frequently participate in reversible loops involving oxidoreductases and dehydrogenases.

We first profiled NAD(P)-dependent reactions in the muscle-GEM. To detect potential cycling reactions, we selected reactions whose fluxes (i) exceeded 10% of the maximum flux bounds and (ii) were at least twofold higher than those obtained from pFBA analysis. Applying these criteria revealed several reactions with elevated fluxes in both FBA and FVA-sampling but with markedly reduced or suppressed fluxes in pFBA (**Supplementary Figure 3f**). These included reactions associated with *P5CDh1* in arginine and proline metabolism, *Aldh-III* in the Miscellaneous subsystem, *CG8888* in retinol metabolism, and *CG2767* in pyruvate metabolism.

3c. Flux boundary effects in FVA-sampling:

In FVA-sampling analysis, flux solutions of some of some unbounded reactions may approach to boundary limits, raising the possibility that the default bounds may be too restrictive relative to the actual feasible solution spaces. Especially, in our muscle-GEM, default reaction flux bounds were set at ±1,000 (arbitrary units, given unavailable precise physiological units for *Drosophila* muscle *in vivo*). While constraining reaction bounds to physiologically relevant values is critical for accurate flux predictions, comprehensive experimental data required to fully constrain all reaction bounds in *Drosophila* GEM was lacking, generating the potential boundary effects from the simulation.

To assess this possibility, we tested three boundary conditions: ±1000 (default), ±10000, and ±50000. For each boundary condition, all default reaction bounds were scaled to the new boundary values while maintaining model-specific constraints (e.g., HSD and NSD). After varying the boundary limits, we performed FVA followed by sampling analysis. To determine reactions approaching boundary saturation, we used two complementary criteria: (i) reactions approaching boundaries (max/min saturation), where maximum or minimum sampled flux values approached within 1% of the imposed boundary (e.g., max flux ≥990 for a +1000 boundary), and (ii) reactions with consistently high flux (median saturation), where median flux values approached within 1% of the boundary magnitude. Although this percentage depends on the precise threshold used to define boundary proximity, we applied a stringent 1% cutoff to conservatively identify reactions potentially affected by numerical limits.

This analysis revealed minimal effects of boundary magnitude on saturation patterns. In both NSD and HSD models, reactions approaching upper bound saturation were only about 2 % of all

reactions across boundary conditions, whereas reactions showing lower bound saturation were about 1 % (**Supplementary Figure 3g**). Similarly, across different boundary conditions, median flux criteria also showed that less than 1 % of reactions were within 99 % boundary limits. These results suggested that the default ±1000 bounds, including some unbounded nutrient uptake constraints, were not overly restrictive for the majority of reactions in our metabolic model.